A Progress Report

January 1, 1989 to June 30, 1989

NASA-UVA LIGHT AEROSPACE ALLOY AND STRUCTURES TECHNOLOGY PROGRAM

NASA-LaRC Grant NAG-1-745

Submitted to:

National Aeronautics and Space Administration
Langley Research Center
Hampton, Virginia 23665

Attention: Mr. J.F. Royall, Jr.
Grants Officer MS 126

For Review by: Mr. D.L. Dicus
Grant Monitor
Metallic Materials Branch MS 188A

Submitted by:

Richard P. Gangloff
Associate Professor

Department of Materials Science
School of Engineering and Applied Science
University of Virginia
Charlottesville, VA 22901

Report No. UVA/528266/MS90/104
August 1989

Copy No.___

NASA-UVA LIGHT AEROSPACE ALLOY
AND STRUCTURES TECHNOLOGY PROGRAM

Program Director:

Richard P. Gangloff

Co-principal Investigators:

Richard P. Gangloff
John K. Haviland
Carl T. Herakovich
Walter D. Pilkey
Marek-Jerzy Pindera
Earl A. Thornton
Glenn E. Stoner
Robert E. Swanson (VPI)
Franklin E. Wawner, Jr.
John A. Wert

NASA-LaRC Grant Monitor:

Dennis L. Dicus

TABLE OF CONTENTS

NASA-UVA LIGHT AEROSPACE ALLOY AND STRUCTURES TECHNOLOGY PROGRAM

SUMMARY

The NASA-UVa Light Aerospace Alloy and Structures Technology Program (LA^2ST) has been founded by substantially broadening the scope of a predecessor NASA-Langley Grant. Here, we report on progress achieved between January 1 and June 31, 1989.

The objective of the LA^2ST Program is to conduct interdisciplinary graduate student research on the performance of next generation, light weight aerospace alloys and associated thermal gradient structures in close collaboration with Langley researchers. Individual technical objectives are established for each research project. Our efforts will produce basic understanding of material behavior, new monolithic and composite alloys, processing methods, solid and fluid mechanics analyses, measurement advances and a pool of educated graduate students.

The accomplishments presented in this report are highlighted as follows:

- 6 PhD and 3 MS graduate students, and 7 faculty members from three Departments at UVa and VPI are participating in 9 research projects, each in conjunction with a Branch at LaRC.

- 5 new projects, each with a graduate student, and 3 additional faculty advisors will begin within the next two months. 2 students were recruited for this work.

- 6 publications and 6 presentations at technical meetings were recorded during this reporting period.

- Research on corrosion fatigue of Al-Li-Cu alloy 2090 broadly characterized fracture mechanics and fractographic behavior, and established the central role of hydrogen embrittlement to guide alloy development and life prediction.

- Research on Al-Li-Cu alloys reproduced the beneficial strengthening effect of small In additions for large heats, and demonstrated a complex notch fracture toughness behavior which is degraded by overaging, low test temperature and perhaps indium.

- Research on localized corrosion of Al-Li alloys has shown that T_1 phase is active and does not passivate for a broad pH range, while iron-bearing constituent particles are aggressively cathodic compared to Al. Resulting subboundary attack and near particle ditching are significant in pitting and stress corrosion crack initiation.

- Research on SCC of Al-Li-Cu alloys demonstrated the dramatic effects of certain electrolytes, particularly lithium carbonate, which decrease time-to-failure for slow strain rate and "Breaking Load" type experiments.

- Research on fiber-matrix reaction studies (Ti-1100 and Ti-15-3 matrices containing SCS-6, SCS-9 and SCS-10 fibers) has been initiated. The kinetic parameters, reaction zone thickness versus time, reaction constants and activation energies have been determined and compared with other systems.

- Research on methods for quantifying non-random particle distributions in materials has led to generation of a set of computer programs that can detect and characterize clusters of particles.

This work was largely supported by the previous grant to the Materials Science Department; new funding was received in June of this year and work in solid mechanics is now commencing in conjunction with the projects described in this report.

INTRODUCTION

Background

For the past three years, the NASA-Langley Research Center has sponsored graduate student research at the University of Virginia and at Virginia Polytechnic Institute and State University on the performance of light aerospace alloys in aggressive environments [1]. Results are documented in a series of progress reports [2-4]; a grant review meeting was held in July of 1988 at NASA-LaRC. In the Fall of 1988 this program was increased to incorporate research at UVa on the processing of advanced aerospace materials [5], and in early 1989 the program was further increased in scope to include broadly interdisciplinary work on solid mechanics and thermal structures [6]. The NASA-UVA LIGHT AEROSPACE ALLOY AND STRUCTURES TECHNOLOGY PROGRAM (LA^2ST) was thusly founded. This progress report summarizes the results obtained under this interdisciplinary program and for the period from January 1, 1989 to June 30, 1989.

Problem and Needs

Future aerospace missions require advanced light alloys and composites with associated processing and fabrication methods; new structural design methods and concepts with experimental evaluations; component reliability/durability/damage tolerance prediction procedures; and a pool of doctoral level engineers and scientists. Work on advanced materials and structures must be fully integrated. The NASA-UVa Technology Program addresses these needs.

LA^2ST Program

As detailed in the original proposal [6], faculty from the Departments of Materials Science, Mechanical and Aerospace Engineering and Civil Engineering at UVa are participating in the LA^2ST research and education program centered on high performance, light weight, aerospace alloys and structures. The objective of this effort is to develop long term and interdisciplinary collaborations between graduate students, UVa faculty, and NASA-Langley researchers. Our efforts will produce basic understanding of materials behavior, new monolithic and composite alloys, processing methods, solid and fluid mechanics analyses, and measurement advances. A major product of the program is graduate students with education and research experience in materials science, mechanics and mathematics.

The scope of the LA^2ST Program is broad. Four research project areas are being investigated, including: (1) ENVIRONMENT ASSISTED DEGRADATION MECHANISMS IN ADVANCED LIGHT METALS, (2) AEROSPACE MATERIALS SCIENCE, (3) MECHANICS OF MATERIALS FOR AEROSPACE STRUCTURES, and (4) THERMAL GRADIENT STRUCTURES. Fourteen specific research projects are ongoing within these areas. These projects, which form the basis for the dissertation

requirement of graduate studies, involve nine faculty and fourteen graduate students. The majority of the graduate students are doctoral level and citizens of the United States. Research is conducted at either UVa or LaRC, and under the guidance of UVa faculty and NASA professionals. Each project is developed in conjunction with a specific LaRC researcher. Participating students and faculty are closely identified with a NASA-LaRC sponsored program.

A primary goal of the LA^2ST Program is to foster interdisciplinary research. To this end, many of the research projects share a common focus on light and reusable space structures which will be subjected to aggressive terrestrial and space environments; with emphasis on both cryogenic and elevated temperature conditions with severe thermal gradients typical of tankage structures.

Organization of Progress Report

This progress report provides organizational and administrative information (viz. statistics on the productivity of faculty and student participants, a history of current and graduated students, and ongoing projects with NASA and UVa advisors). The next sections provide summaries of technical accomplishments and problems for each research project and over the period from January to June of 1989. Appendices document conference participation and provide reprints of technical papers which were developed under Grant sponsorship.

References

1. R.P. Gangloff, G.E. Stoner and M.R. Louthan, Jr., "Environment Assisted Degradation Mechanisms in Al-Li Alloys", University of Virginia, Proposal No. MS-NASA/LaRC-3545-87, October, 1986.

2. R.P. Gangloff, G.E. Stoner and R.E. Swanson, "Environment Assisted Degradation Mechanisms in Al-Li Alloys", University of Virginia, Report No. UVA/528266/MS88/101, January, 1988.

3. R.P. Gangloff, G.E. Stoner and R.E. Swanson, "Environment Assisted Degradation Mechanisms in Advanced Light Metals", University of Virginia, Report No. UVA/528266/MS88/102, June, 1988.

4. R.P. Gangloff, G.E. Stoner and R.E. Swanson, "Environment Assisted Degradation Mechanisms in Advanced Light Metals", University of Virginia, Report No. UVA/528266/MS89/103, January, 1989.

5. T.H. Courtney, R.P. Gangloff, G.E. Stoner and H.G.F. Wilsdorf, "The NASA-UVA Light Alloy Technology Program", University of Virginia, Proposal No. MS NASA/LaRC-3937-88, March, 1988.

6. R.P. Gangloff, "NASA-UVa Light Aerospace Alloys and Structures Technology Program", University of Virginia, Proposal No. MS NASA/LaRC-4278-89, January, 1989.

SUMMARY STATISTICS

The following table documents numbers of students and faculty who have or are participating in the LA^{2}ST Program. Education and research accomplishments are indicated by the numbers of degrees awarded, and by publications and presentations, respectively. The youth of the program explains the lack of degrees granted to date; the first two PhD students should graduate in 1989. The senior PhD student on the program, Mr. Robert Piascik, should graduate in September and has accepted a position with the Fatigue and Fracture Branch at the Langley Research Center. Mr. James Moran plans to graduate in late 1989, and has accepted a National Research Council Postdoctoral Fellowship at the Naval Research Laboratories in Washington, D.C. The aggressive character and quality of the ongoing research projects are indicated by the publication and presentation activity. As an example, Grant research was well represented at the recent International Conference on Aluminum-Lithium alloys.

	1/1 to 6/30/89	1986 TO 1/89
PhD Students: UVa	5	3
: NASA-LaRC	1	1
MS Students: UVa	2	0
: NASA-LaRC	0	0
: VPI	1	1
Faculty: UVa	6	2
: VPI	1	1
Research Associates: UVa	1	0
PhD Awarded:	0	0
MS Awarded:	0	0
Employers: NASA	0	0
: Other	0	0
Publications:	6	3
Presentations:	6	7
Dissertations/Theses:	0	0
NASA Reports:	1	4

GRADUATE STUDENT PARTICIPATION IN THE NASA-UVa LA^{2}ST PROGRAM

POS #	GRADUATE STUDENT EMPLOYER	ENTERED PROGRAM	DEGREE COMPLETED	LANGLEY RESIDENCY	RESEARCH TOPIC	UVa/NASA-LaRC ADVISORS
1.	R. S. Piascik NASA-Langley	6/86	Ph.D. 8/89		Damage Localization Mechanisms in Corrosion Fatigue of Aluminum-Lithium Alloys	R. P. Gangloff D. L. Dicus
2.	J. A. Wagner NASA-Langley	6/87	Ph.D. 6/91	PhD Research @ LaRC	Deformation and Fracture of Thin Sheet Aluminum-Lithium Alloys: The Effect of Cryogenic Temperatures	R. P. Gangloff W. B. Lisagor J. C. Newman
3.	R. G. Buchheit	6/87	Ph.D. 1/91		Measurements and Mechanisms of Localized Aqueous Corrosion in Aluminum-Lithium Alloys	G. E. Stoner D. L. Dicus
4.	W. C. Porr, Jr.	1/88	Ph.D. 6/91		Elevated Temperature Crack Growth in Advanced Aluminum Alloys	R. P. Gangloff C. E. Harris
5.	D. Gundel	9/88	M.S. 5/90		Investigation of the Reaction Kinetics Between SiC Fibers and Titanium Matrix Composites	F. E. Wawner W. Brewer
6.	F. Rivet (VPI)	9/88	M.S. 3/90		Deformation and Fracture of Aluminum-Lithium Alloys: The Effect of Dissolved Hydrogen	R. E. Swanson (VPI) D. L. Dicus
7.	J. Parse	9/88	Ph.D. 5/91		Quantitative Characterization of Spatial Distribution of Particles in Materials	J. A. Wert D. R. Tenney
8.	J. P. Moran	9/88	Ph.D. 12/89		An Investigation of the Localized Corrosion and Stress Corrosion Cracking Behavior of Alloy 2090	G. E. Stoner W. B. Lisagor

GRADUATE STUDENT PARTICIPATION IN THE NASA-UVa LA^{2}ST PROGRAM
(continued)

POS #	GRADUATE STUDENT EMPLOYER	ENTERED PROGRAM	DEGREE COMPLETED	LANGLEY RESIDENCY	RESEARCH TOPIC	UVa/NASA-LaRC ADVISORS
9.	C. Copper	4/89	M.S. 1/91		Design of Cryogenic Tanks for Launch Vehicles	W. D. Pilkey J. K. Haviland
10.	D. C. Slavik	9/89	Ph.D. 6/92		Near Threshold Corrosion Fatigue of Advanced Aluminum Alloys and Composites	R. P. Gangloff D. L. Dicus

Post-Doctoral Research Associate Participation
in NASA-UVa LA^2ST Program

Pos #	Res. Assoc. Employer	Tenure	Research	Supervisor
1	Yang Leng	3/88 to 3/90	Eleveated Temp- ature Fracture of PM Al Alloys. Fatigue of Composites	R. P. Gangloff

CURRENT PROJECTS

ENVIRONMENT ASSISTED DEGRADATION MECHANISMS IN ADVANCED LIGHT METALS

1. DAMAGE LOCALIZATION MECHANISMS IN CORROSION FATIGUE OF ALUMINUM-LITHIUM ALLOYS
   Faculty Investigator: R.P. Gangloff
   Graduate Student: Robert S. Piascik; PhD candidate
   UVa Department: Materials Science
   NASA-LaRC Contact: D. L. Dicus (Metallic Materials)
   Start Date: June, 1986
   Anticipated Completion Date: August, 1989

2. ELEVATED TEMPERATURE CRACK GROWTH IN ADVANCED RAPIDLY SOLIDIFIED POWDER METALLURGY ALUMINUM ALLOYS
   Faculty Investigator: R.P. Gangloff
   Graduate Student: William C. Porr, Jr.; PhD candidate
   UVa Department: Materials Science
   NASA-LaRC Contact: C.E. Harris (Fatigue and Fracture)
   Start Date: January, 1988
   Anticipated Completion Date: June, 1991

3. DEFORMATION AND FRACTURE OF THIN SHEET ALUMINUM-LITHIUM ALLOYS: THE EFFECT OF CRYOGENIC TEMPERATURES
   Faculty Investigator: R.P. Gangloff
   Graduate Student: John A. Wagner; PhD candidate
   UVa Department: Materials Science
   NASA-LaRC Contacts: W.B. Lisagor (Metallic Materials) and J.C. Newman (Fatigue and Fracture)
   Start Date: June, 1987
   Anticipated Completion Date: June, 1991

4. NEAR THRESHOLD CORROSION FATIGUE OF ADVANCED ALUMINUM ALLOYS AND COMPOSITES
   Faculty Investigator: R.P. Gangloff
   Graduate Student: Donald Slavik; PhD Candidate
   UVa Department: Materials Science
   NASA-LaRC Contact: D.L. Dicus (Metallic Materials)
   Start Date: September, 1989
   Anticipated Completion Date: June, 1992

5. MEASUREMENTS AND MECHANISMS OF LOCALIZED AQUEOUS CORROSION IN ALUMINUM-LITHIUM ALLOYS
   Faculty Investigator: Glenn E. Stoner
   Graduate Student: Rudolph G. Buchheit, Jr.; PhD candidate
   UVa Department: Materials Science
   NASA-LaRC Contact: D. L. Dicus (Metallic Materials)
   Start Date: June, 1987
   Anticipated Completion Date: January, 1991

6. AN INVESTIGATION OF THE LOCALIZED CORROSION AND STRESS CORROSION CRACKING BEHAVIOR OF ALLOY 2090 (Al-Li-Cu)
Faculty Investigator: Glenn E. Stoner
Graduate Student: James P. Moran; PhD candidate
UVa Department: Materials Science
NASA-LaRC Contact: W.B. Lisagor (Metallic Materials)
Start Date: September, 1988
Anticipated Completion Date: December, 1989

7. THE EFFECTS OF ZINC ADDITION ON THE ENVIRONMENTAL STABILITY OF ALUMINUM-LITHIUM ALLOY
Faculty Investigator: Glenn E. Stoner
Graduate Student: MS or PhD candidate to be recruited
Department: Materials Science
NASA-LaRC Contact: W.B. Lisagor (Metallic Materials)
Start Date:
Anticipated Completion Date:

8. DEFORMATION AND FRACTURE OF ALUMINUM-LITHIUM ALLOYS: THE EFFECT OF DISSOLVED HYDROGEN
Faculty Investigator: R.E. Swanson (VPI)
Graduate Student: Frederick C. Rivet; MS candidate
VPI Department: Materials Engineering at VPI
NASA-LaRC Contact: D.L. Dicus (Metallic Materials)
Start Date: September, 1988
Anticipated Completion Date: March, 1990

AEROSPACE MATERIALS SCIENCE

1. INVESTIGATION OF THE REACTION KINETICS BETWEEN SIC FIBERS AND SELECTIVELY ALLOYED TITANIUM MATRIX COMPOSITES AND DETERMINATION OF THEIR MECHANICAL PROPERTIES
Faculty Investigator: F.E. Wawner
Graduate Student: D. Gundel; MS candidate
UVa Department: Materials Science
NASA-LaRC Contact: William Brewer (Metallic Materials)
Start Date: September, 1988
Anticipated Completion Date: May, 1990

2. THE EFFECT OF NON-RANDOM PARTICLE DISTRIBUTION ON THE MECHANICAL BEHAVIOR OF STRUCTURAL MATERIALS
Faculty Investigator: John A. Wert
Graduate Student: Joseph Parse; PhD candidate
UVa Department: Materials Science
NASA-LaRC Contact: D.R. Tenney (Materials Division)
Start Date: September, 1988
Anticipated Completion Date: May, 1991

MECHANICS OF MATERIALS FOR AEROSPACE STRUCTURES

1. INELASTIC RESPONSE OF METAL MATRIX COMPOSITES UNDER BIAXIAL LOADING
   Faculty Investigators: Carl T. Herakovich and Marek-Jerzy Pindera
   Graduate Student: To be recruited
   UVa Department: Civil Engineering
   NASA-LaRC Contact: Charles Harris (Fatigue and Fracture)
   Start Date: April, 1989
   Anticipated Completion Date: January, 1991

THERMAL GRADIENT STRUCTURES

1. DESIGN OF CRYOGENIC TANKS FOR LAUNCH VEHICLES
   Faculty Investigators: W. D. Pilkey and J. K. Haviland
   Graduate Student: Charles Copper
   UVa Department: Mechanical and Aerospace Engineering
   NASA-LaRC Contact: Donald Rummler (Thermal Structures)
   Start Date: April, 1989
   Anticipated Completion Date: January, 1991

2. FINITE ELEMENT THERMAL-STRUCTURAL ANALYSIS OF HIGH TEMPERATURE VISCOPLASTIC STRUCTURES
   Faculty Investigator: Earl A. Thornton
   Graduate Student: To be recruited
   UVa Department: Mechanical and Aerospace Engineering
   NASA-LaRC Contact: Donald Rummler (Thermal Structures)
   Start Date: August, 1989
   Anticipated Completion Date: To be determined

3. EXPERIMENTAL STUDY OF THE VISCOPLASTIC RESPONSE OF HIGH TEMPERATURE STRUCTURES
   Faculty Investigators: Earl A. Thornton and Richard P. Gangloff
   Graduate Student: To be recruited
   UVa Department: Mechanical and Aerospace Engineering
   NASA-LaRC Contact: Donald Rummler (Thermal Structures)
   Start Date: August, 1989
   Anticipated Completion Date: To be determined

ADMINISTRATIVE PROGRESS AND PLANS

Student Recruitment

Several new students have been recruited into the LA^2ST Program, including:

- Mr. Donald Slavik; PhD candidate from General Electric Aircraft Engine Group; working with Prof. Gangloff in Materials Science, beginning in August of 1989.

- Mr. Charles Copper; MS candidate from Washington and Lee University; working with Profs. Haviland and Pilkey in Mechanical and Aerospace Engineering, beginning in May of 1989.

- Ms. Cynthia Lach; MS candidate currently employed by NASA-LaRC; working with Prof. Gangloff in Materials Science, beginning in January of 1990.

Brochure

A brochure will be developed during the second half of 1989. The purpose of this will be to facilitate graduate student recruitment by describing the educational and technical opportunities provided by the LA^2ST Program. A secondary objective will be to advertise our research programs to the technical community worldwide.

Yearly Meeting

Because of the delayed startup of several of the research projects, we plan to postpone the proposed annual NASA-UVa technical meeting until the Spring of 1990. During the next quarter, the Technical Program Director and the NASA Grant Monitor will decide upon the format and scheduling of this technical session. The objective here is to provide graduate students and other participants with a presentation opportunity, to review and improve research directions, to promote interdisciplinary research and to spawn new technical ideas.

RESEARCH PROGRESS AND PLANS (January 1, 1989 to June 30, 1989)

Research progress recorded during the period of this report and future plans are described here for individual projects. Since the funding for the 1989 Technology Program did not arrive at UVa until June 1989, only those projects which were ongoing under the predecessor grant are described. All individual projects will be initiated by the end of August, 1989, and will be discussed in the next progress report.

Program 1 DAMAGE LOCALIZATION MECHANISMS IN CORROSION FATIGUE OF ALUMINUM-LITHIUM ALLOYS

Robert S. Piascik and Richard P.Gangloff

This research project is essentially completed. Mr. Piascik is in the final stages of writing his PhD dissertation and plans to defend this work near the end of August. Three papers have been published and two additional papers are planned.

The essence of our results on environmental fatigue crack propagation in Aluminum-Lithium alloys is given by the following conclusions which were taken from each chapter of the dissertation.

A. DEVELOPMENT OF ELECTRICAL POTENTIAL MEASUREMENTS OF CRACK GROWTH FOR GASEOUS AND AQUEOUS ENVIRONMENTS

Conclusions

1. The direct current electrical potential method accurately and reproducibly monitors fatigue crack propagation in aluminum alloys exposed to a variety of benign and corrosive gaseous and aqueous environments.

2. Experimental results for steels compare with literature data demonstrating that experimental equipment and methods can be applied to the study of environmental effects on intrinsic fatigue crack propagation in aluminum alloys.

3. Aqueous corrosion fatigue crack growth rates in aluminum are not altered by an applied electrical current.

4. Corrosion fatigue crack propagation in alloy 2090 is not influenced by the EDM micronotch; neither contaminants nor a remelt zone were introduced.

B. INTRINSIC FATIGUE CRACK GROWTH

Conclusions

1. Using high resolution potential difference monitoring, a short crack geometry and the current constant $\Delta K/K_{max}$ step

changed R test scheme, an excellent method has been developed for the continuous insitu monitoring of intrinsic fatigue crack growth in aluminum alloys.

2. The intrinsic fatigue crack growth characteristics for alloy 2090 in moist air exhibit an intermediate stress intensity range "plateau" behavior, suggesting a microstructural/environmental change in fracture behavior for near threshold fatigue crack growth compared to the Paris regime.

3. The intrinsic transgranular fatigue crack growth characteristics of Al-Li-Cu alloy 2090 rolled plate are independent of crack path direction.

4. Single grain (microstructurally small) cracks, monitored by the potential difference method, do not exhibit accelerated fatigue crack growth rates; fatigue crack growth rate threshold stress intensity range is similar to that for long cracks.

5. Grain boundary microstructure inhibits the growth of elliptical surface flaws contained in single grains. The fatigue crack growth of through thickness cracks contained in single grains is not influenced by high angle grain boundaries.

6. In moist air 2000 series alloys (including alloy 2090) exhibit identical intrinsic fatigue crack growth characteristics. 7000 series alloys exhibit similar but higher intrinsic fatigue crack growth rates.

C. INTRINSIC FATIGUE CRACK GROWTH IN GASEOUS ENVIRONMENTS

Conclusions

1. Gaseous environments capable of producing hydrogen, viz. moist air and water vapor, accelerate da/dN for alloy 2090. Water vapor effects are pronounced near threshold with crack growth rates accelerated at extremely low water vapor pressures. At high ΔK, little environmental effect is observed.

2. Near threshold, high R results for alloy 2090 in water vapor support a molecular transport model. Increased crack opening at high mean stress enhances Knudsen flow, resulting in increased crack tip environmental interaction. Other factors, such as highly localized crack tip reaction area may also explain a reduced saturation value.

3. In embrittling environments alloy 2090 exhibits better intrinsic transgranular fatigue crack growth compared to alloy 7075.

4. Surface films formed in oxidizing environments do not alter fatigue crack growth rates by either impeding slip reversibility or homogenizing localized deformation.

5. Fatigue crack growth in moist air is governed by a complex embrittlement damage mechanism. Oxygen inhibits embrittlement by water vapor in alloy 2090; possibly by competitive adsorption or protective surface film formation.

D. INTRINSIC FATIGUE CRACK GROWTH IN AQUEOUS ENVIRONMENTS

Conclusions

1. Al-Li-Cu alloy 2090, peak aged, is susceptible to transgranular corrosion fatigue crack propagation in aqueous 1% NaCl under anodic polarization.

2. The effect of aqueous NaCl on fatigue crack growth rate depends on stress intensity range. Near threshold, anodic potential aqueous crack growth rates are greatly increased compared to inert environment. At high ΔK environmental effects are reduced.

3. Environmental effects on alloy 2090 are less severe than those observed for high strength alloy 7075; the new aluminum lithium alloy behaves similarly to conventional 2000 series alloys.

4. Corrosion fatigue crack growth rates are relatively insensitive to loading frequency, but are greatly reduced by cathodic polarization.

5. The effect of load frequency, cathodic polarization and Li2C03 addition suggest that crack tip films play as important role in corrosion fatigue damage. Film formation hinders the hydrogen embrittlement process which is presumed to control environmental crack propagation.

6. High angle boundaries do not play an important role in aqueous corrosion fatigue growth in alloy 2090.

7. Limited data suggest that short crack-chemical effects which could enhance corrosion fatigue crack growth are not operative in alloys 2090 or 7075.

E. FRACTOGRAPHIC ANALYSES

Conclusions

1. For inert and oxidizing environments (viz:0_2, He, vacuum), fatigue crack growth proceeds by 111 slip band cracking. This growth mechanism is independent of ΔK.

2. For hydrogenous environments, changes in da/dN are associated with changes in crack tip damage mechanism. The fatigue crack growth mechanisms depend on ΔK. At moderate to high ΔK, fatigue crack growth is dominated by sub-grain boundary cracking; lesser amounts of slip band cracking observed. For near threshold, cracking is by a cleavage mechanism which produces {100} or {110} facets.

3. The changes in slope of the fatigue crack growth response are associated with the presence of hydrogen.

4. Similar fatigue fracture morphologies for water vapor and aqueous NaCl suggest hydrogen embrittlement; a dissolution mechanism is unlikely.

5. Increased surface oxide thickness on fatigue fracture surfaces in oxygen, relative to vacuum, and no increase in fatigue crack growth rate suggest that films are not damaging.

F. CORROSION FATIGUE DAMAGE MECHANISMS

Conclusions

1. Environmental fatigue crack propagation in moist air, pure water vapor and aqueous NaCl proceeds by a hydrogen embrittlement mechanism. While anodic dissolution may contribute to this mechanism, there is no evidence that this process is uniquely causal of corrosion fatigue.

2. A hydrogen embrittlement process zone model, based on dislocation transport and volume diffusion of hydrogen in a portion of the crack tip plastic zone rationalizes the observed corrosion fatigue crack propagation responses for a variety of environmental conditions.

3. The size of the process zone relative to microstructure, particularly subgrain size for the Al-Li alloy, determines rates and microscopic paths for hydrogen enhanced corrosion fatigue.

4. While surface films have no influence on fatigue crack growth in alloy 2090, they may reduce hydrogen production and associated crack growth rates by preferential formation and blockage processes.

5. The effects of key variables (frequency and cathodic potential) are not simply explained by the process zone model. Such variables are likely, however, to affect crack chemistry and hydrogen uptake; hydrogen embrittlement is probable, but crack chemistry modeling is required to complement the process zone ideas.

Future Plans

Research on environmental fatigue crack propagation in advanced aluminum alloys will be continued by Mr. Donald Slavik and according to the plans outlined in the January, 1989 proposal for the LA^2ST Program. Further studies of crack tip damage mechanisms, additional aluminum alloys and microstructures, and metal matrix-ceramic short fiber composites will be emphasized.

Program 2 ELEVATED TEMPERATURE CRACK GROWTH IN ADVANCED POWDER METALLURGY ALUMINUM ALLOYS

William C. Porr, Jr. and Richard P. Gangloff

Objective

The goal of this research program is to evaluate subcritical crack growth and fracture toughness at elevated temperatures in advanced aluminum alloys. As an extension of this goal, the effect of microstructure or environment on crack growth and mechanisms will also be examined.

Approach

Program approach was outlined in a previous report [1]. Research efforts over the past six month period included materials acquisition and microstructural characterization, test technique refinement, initial testing and analysis of the room temperature fracture/fatigue behavior of aluminum alloy 2618.

Research Progress and Results

Materials. As reported previously, a 0.57" thick plate of aluminum alloy 2618 with a T651 temper was acquired from Cegedur Pechiney with chemical analysis and complete mechanical properties documentation [1].

Additionally, two Al-Fe-V-Si powder metallurgy alloys manufactured by Allied-Signal, Inc. acquired with nominal compositions (wt.%) [2]:

Al, 8.5 Fe, 1.3 V, 1.7 Si

and

Al, 12.4 Fe, 1.2 V, 2.3 Si

These alloys are designated FVS0812 and FVS1212, respectively, and were provided by Dr. P. S. Gilman of Allied-Signal. Both alloys are designed with thermally stable silicide dispersoids for elevated temperature property stability. The FVS1212 has a high volume fraction (36%) of the silicide for high strength and stiffness, where the FVS0812 has a lower silicide volume fraction (27%) for improved fracture toughness over the FVS1212 [2]. The room temperature yield and tensile strengths for the FVS1212 were found to be 73.8 ksi and 78.2 ksi, respectively.

Figures 1a throught 1c are micrographs showing the microstructures of the three aluminum alloys. Figure 1a shows the equiaxed grain structure of the as received 2618. The grains are approximately 30-40 microns in size. Small precipitates of $CuMgAl_2$ are barely visible along the boundaries while larger (10-20 microns) $FeNiAl_9$ constituents are aligned parallel to the

rolling direction. The insoluble and thermally stable $FeNiAl_9$ particles are present for mechanical properties retention with increasing temperature.

Little microstructural detail can be seen in the optical micrographs of FVS0812 and FVS1212 shown in figures 1b and 1c, respectively. This is expected considering the ultra fine structure reported for the rapidly solidified powders used in these alloys. However, the micrographs do show alignment of the prior particle boundaries with the extrusion direction. The dimensions of the aligned microstructure appear to be consistent with a prior particle size expected from the 40 mesh filtering [3] conducted in the processing of these powders.

Test Technique Refinement. The electric potential difference (EPD) technique will be used to measure crack growth in compact tension (CT) test specimens during the fracture resistance experiments conducted in this program. This laboratory, however, has had no prior experience with the EPD method in CT specimens. As there is no ASTM standard for EPD testing, initial evaluation of the accuracy and range of applicability of a calibration polynomial was necessary. EPD calibration polynomials are generally of the form [4]:

$$a/a_o = f(V/V_o)$$

where:

a = crack length,
a_o = reference crack length,
V = measured potential,
V_o = reference potential for crack length a_o.

The calibration polynomial evaluated was originally developed by Hicks and Pickard [5] and is being incorporated into ASTM standard E647, Measurement of Fatigue Crack Growth Rates, by ASTM committee E24.04.01 [4]. It has two forms, normalized for specimen dimensions:

$$V/V_o = 0.5766 + 1.9169(a/W) + -1.0712(a/W)^2 + 1.6898(a/W)^3$$

and

$$a/W = -0.5051 + 0.8857(V/V_o) + -0.1398(V/V_o)^2 + 0.0002398(V/V_o)^3$$

where:

V_o = reference potential for $a/W = 0.241$,
W = CT specimen width,

and all other variables are as previously defined. The first of these two equations can be used to calculate V_o from a known crack length and measured potential. This V_o can then be used in the second equation to calculate crack length for any measured V.

Three tests were conducted using alloy 2618 to evaluate these polynomials. Fatigue tests were run using the compliance

technique to measure crack growth. Simultaneously, specimen potential was periodically measured using DC potential drop techniques. After correcting the compliance values of crack length with several visual measurements, the crack lengths were paired with potential measurements according to cycle count. The potential data were normalized based on measured notch length and notch Vo and were plotted with the polynomial. The results of these tests are shown in Figure 2. There is good agreement between the measured values and the polynomial over a wide range of a/W.

Two subtle questions were addressed with the testing. The first was the validity of the polynomial at high values of a/W. As can be seen in Figure 2, even at a/W values greater than 0.8 there was good agreement between the measured values and the polynomial prediction. Secondly, it was uncertain whether the notch potential could be used, along with the notch length, to calculate the normalizing potential, V_o. The initial finite element analysis used by Hicks and Pickard to develop the polynomial considered a crack in the specimen, and not a notch. Therefore, theoretically, the polynomial should not be valid for a notch. Experimentally, normalizing the data with consideration of the notch potential causes less than a 5 percent difference in overall crack lengths between measured and polynomial values, as shown in figure 2. This is a convenient result as it allows fatigue testing and precracking from the specimen notch using EPD machine control.

Fracture/Fatigue Behavior of 2618. In all fracture mechanics experiments for this project a standard CT type specimen with W = 1.5 inches will be used. The thickness of the specimen is 0.3 inches with 16.7% sidegrooves (net thickness = 0.25 inches). The sidegrooves will be necessary to prevent crack deflection during the elevated temperature testing to be conducted in the future.

While evaluating the EPD polynomial and precracking fracture toughness specimens, a series of fatigue tests were conducted with the 2618. They were run as decreasing ΔK tests with a constant K_{max} of approximately 12 MPa$\sqrt{m}$ so as to avoid closure problems near threshold. Results of these tests are shown in Figure 3 which was published by Piascik [6]. Crack growth rates for the 2618 are slightly higher than those for other 2000 series aluminum alloys, but still lower than those for the high strength 7000 series alloys. The fatigue threshold, though not well defined, appears to fall in the same ΔK range as with the other aluminum alloys.

Three room temperature fracture toughness tests were performed yielding valid K_{IC} values for the as received 2618 in the LT orientation. A load-load line displacement profile for one of these tests is shown in Figure 4. The K_{IC} values averaged 18.4 MPa$\sqrt{m}$, ranging from 17.2 MPa$\sqrt{m}$ to 20.2 MPa$\sqrt{m}$. This is significantly lower than the expected toughness of 25.2 MPa$\sqrt{m}$

[7]. The load-load line displacement profile confirms visual observations that there was little macroscopic plasticity or stable crack growth prior to unstable crack growth and final fracture. The overload fracture surface was flat with practically no shear lips.

Figure 5 is an SEM image of the overload fracture surface. The high volume percent of constituents that was seen in Figure 1a can be seen here as well. The constituents served as void initiation sites, as evidenced by the fact that there is at least one at the bottom of most dimples in the fractograph. The high volume fraction of large constituents providing many void initiation sites is the reason for the poor fracture toughness of the material. This high volume percent of constituents is not unusual for 2618-T651, so the reason for the difference between the toughness reported here and that expected is uncertain.

Plans for the Coming Report Period

The elevated temperature testing apparatus described previously [8] is now fully instrumented and operational. Research during the next reporting period will center on studying the effect of temperature and displacement rate on the R-curve behavior of aluminum alloys 2618, FVS0812, and FVS1212 in a moist air environment. Figure 6 is a preliminary test matrix for this work showing the seven temperatures and four displacement rates that will be used in conducting ten tests. The test matrix may change due to limited material availability and initial results. The fracture mechanics testing will be coupled with SEM fractography to correlate toughness results with microstructural observations.

Additionally, the degree requirements of writing and defending a research proposal, and taking the PhD comprehensive exam are planned for this fall.

References

1. R. P. Gangloff, G. E. Stoner, and R. E. Swanson, "Environment Assisted Degradation Mechanisms in Advanced Light Metals", University of Virginia, Report No. UVA/528266/MS89/103, January, 1989.

2. P. S. Gilman, M. S. Zendalis, J. M. Peltier, and S. K. Das, "Rapidly Solidified Aluminum-Transition Metal Alloys for Aerospace Applications", AIAA/AHS/ASEE Aircraft Design, Systems and Operations Conference, September, 1988.

3. P. S. Gilman, private communication to R. E. Franck.

4. J. J. Ruschau, "Guidelines for Use of Electric Potential Drop for Crack Length Determination", Draft of Annex to ASTM Standard E647 by ASTM Committee E24.04.01, March, 1989.

5. M. A. Hicks and A. C. Pickard, "A Comparison of Theoretical and Experimental Methods of Calibrating the Electric Potential Drop Technique for Crack Length Determination", Int. Journal of Fracture, No. 20, 1982, pp. 91-101.

6. R. S. Piascik, PhD Dissertation, to be published in August, 1989.

7. D. Ferton and P. Coppin, private communication.

8. R. P. Gangloff, G. E. Stoner, and R. E. Swanson, "Environment Assisted Degradation Mechanisms in Advanced Light Alloys", University of Virginia, Report No. UVA/528266/MS88/102, June, 1988.

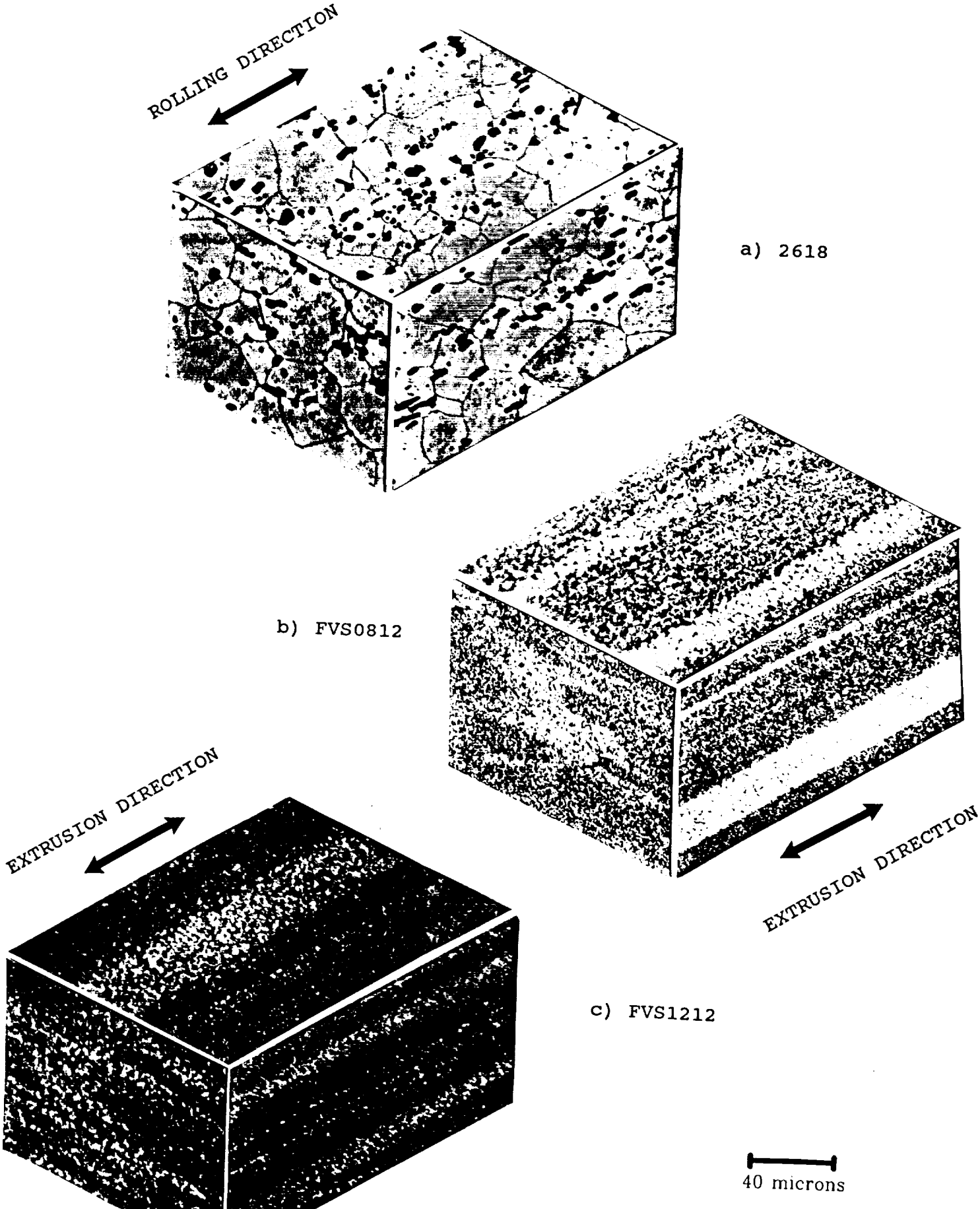

Figure 1. As received microstructures.

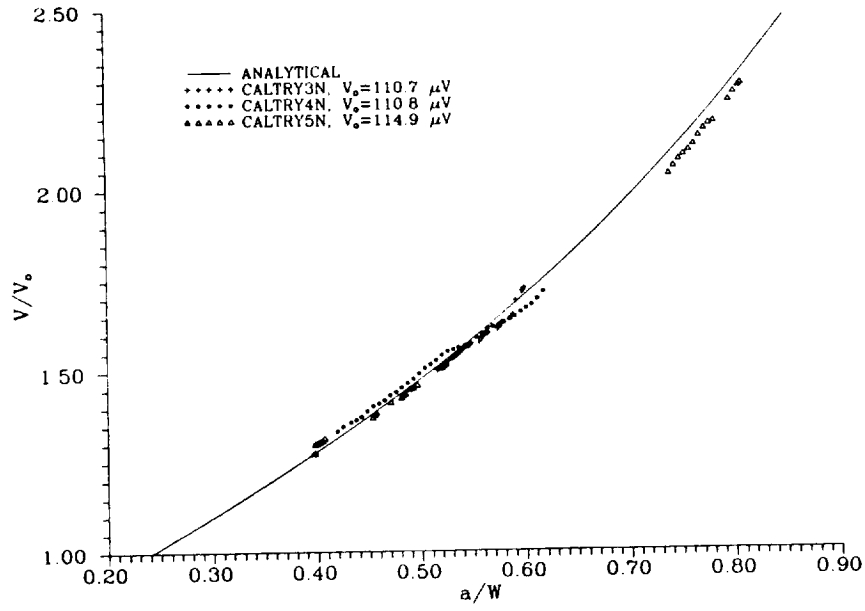

Figure 2. Experimental results of electric potential drop calibration for crack length in a compact tension test specimen.

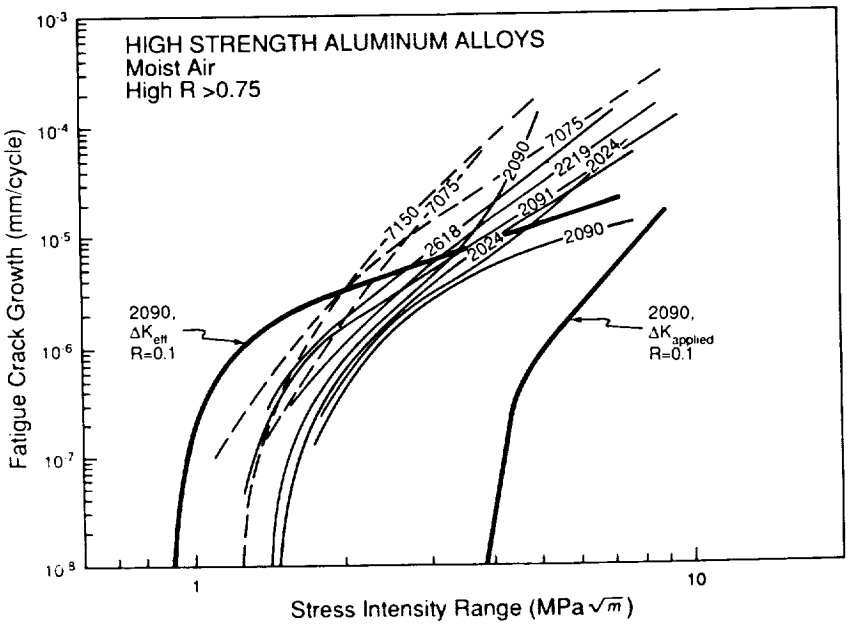

Figure 3. Fatigue crack growth curve for 2618 and other high strength aluminum alloys.

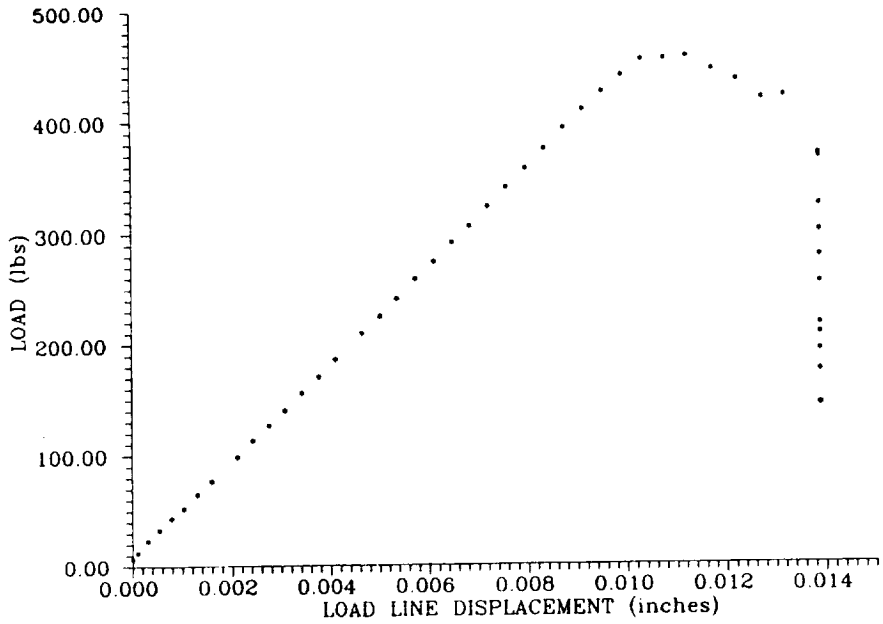

Figure 4. Load -- load line displacement profile for 2618 fracture toughness test 26R3. Initial a/W = 0.598. K_{IC} = 20.2 MPa$\sqrt{m}$.

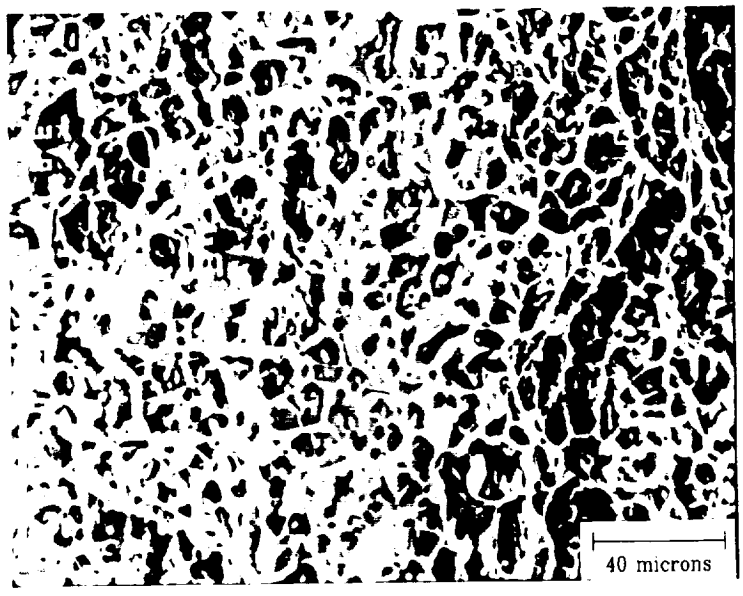

Figure 5. SEM micrograph showing the overload region of a 2618 fracture toughness specimen. K_{IC} = 17.7 MPa$\sqrt{m}$.

Load Line Displacement Rate, in/sec	Temperature, C						
	25	100	150	200	250	300	350
1.00E-04	X	X	X	X	X	X	X
1.00E-05				X			
1.00E-06				X			
1.00E-07				X			

Figure 6. Matrix of temperatures and displacement rates for proposed fracture toughness testing.

Program 3 **DEFORMATION AND FRACTURE OF THIN SHEET ALUMINUM-LITHIUM ALLOYS: THE EFFECT OF CRYOGENIC TEMPERATURES**

John A. Wagner and Richard P. Gangloff

Introduction

Cryogenic tanks are responsible for a large portion of the structural weight of current and proposed launch vehicles. As stated in the most recent progress report of this grant [1], it is envisioned that significant weight and overall cost savings could be realized in future launch vehicles by using advanced forming and joining techniques and novel alloy systems in the fabrication of cryogenic propellent tanks. An ongoing program at NASA-LaRC is evaluating the potential of superplastic forming (SPF) a 2090 based alloy with a minor alloy addition of indium in an effort to reduce the cost of cryogenic tanks. The objective of Program 3 is to understand and optimize the fracture resistance of Al-Cu-Li and Al-Cu-Li-In alloys processed for thin sheet cryogenic tank applications.

Results

Plate, 1/2x47x34", and sheet, 1/8x17x34", have been processed under various schedules at Reynolds Metals and delivered to NASA-LaRC. Compositions of these alloys are:

Al-2.65Cu-2.17Li-0.13Zr-0.05Si-0.05Fe
Al-2.60Cu-2.34Li-0.16Zr-0.04Si-0.05Fe-0.17In (wt %)

The material received was given a thermomechanical treatment (TMT C) or was solution heat treated and stretched approximately 3%. TMT C is a practice used to enhance the SPF behavior of sheet material and leaves the alloy in the overaged condition. Mechanical properties were evaluated using uniaxial tensile and notched Kahn Tear tests at room temperature and -185 C. Specimens were processed according to TMT C and then solution heat treated at 555 C and aged at 160 C for 20, 75 and 120 hours. Results are given in a paper contained in Appendix I.

At room temperature, alloying with indium had no measurable effect on yield strength, but increased the ultimate strength of 2090 based alloys at longer aging times. The addition of indium, however, was not as effective as using a post-solution heat treatment stretch to increase strength. Another observation that can be made from room temperature uniaxial tensile tests is that there was a continuous increase in yield strength and ultimate strength with increasing aging times for both alloys. This suggests that substantial overaging did not occur even at an aging time of 120 hours.

The observation that indium enhances the room temperature ultimate tensile strength, but had no effect on yield strength suggests that indium promotes work hardening in these alloys. This hypothesis, however, is complicated by the fact that the microstructure of the 2090+In was partially recrystallized. The lower yield strength typically associated with a partially recrystallized structure could offsett a beneficial effect indium on room temperature yield strength. The extent to which room temperature tensile behavior is unique to TMTC processed material remains to be defined.

At cryogenic temperatures, there is an improvement in yield and ultimate tensile strength of 2090 baseline and 2090+In alloys. Increased strength at cryogenic temperatures is characteristic of most Al-Li alloys. Moreover, the addition of indium significantly increased the ultimate and also notably the yield strength at cryogenic temperatures compared to the baseline alloy. The mechanism by which In improves yield strength at cryogenic temperatures remains to be determined.

The Kahn Tear test was used to rank alloys and tempers in terms of relative toughness because of its advantage in terms of simplicity and specimen size. Fig. 1 shows the variation in the tear strength to yield strength ratio with temperature for 2090+In in three aging conditions. The tear strength to yield strength ratio (TS/YS) measures the resistance of a material to fracture in the presence a stress raiser [2]. 2090+In exhibited a significant decrease in the TS/YS ratio with increasing aging times at room and cryogenic temperatures. Similar results were obtained for baseline 2090. The decrease in toughness with increasing aging time is typically attributed to an increased yield strength and to an increase in grain and subgrain boundary precipitates which promote intergranular fracture [3]. Both alloys also exhibited a decrease in relative toughness at cryogenic temperatures as indicated by the decrease in the TS/YS ratio, unit initiation energy and unit propagation energy.

Previous investigations on Al-Li plate alloys have shown an increase in toughness with decreasing temperature and have attributed the increase to enhanced intergranular splitting [4] and higher strain hardening rates [5] with no associated change in fracture mode. Fractographic analyses were conducted in the current study to determine the dominate fracture mode and the degree of intergranular splitting.

At room temperature, the macroscopic crack path of Kahn Tear specimens exhibited significant out of plane crack deviation, Fig. 2A. In general the crack path tended to become more planar as the aging time was increased. Microscopically, fracture in the baseline alloys was dominated by transgranular shear (Figs. 2B and 2C) and appeared to be crystallographic in nature. The amount of intersubboundary (ISB) cracking increased with increasing aging time, correlating with the move planar crack paths. In comparison at cryogenic temperatures the relative

toughness decreased and the macroscopic crack path was almost always planar, Fig. 3A. Furthermore, there was a change in the fracture mode of 2090 baseline from transgranular shear at room temperature to predominately intersubboundary failure at cryogenic temperatures, Figs. 3B and 3C, which suggests that ISB is a lower energy event. Similar observations have been made in a previous study on 2090 sheet thermomechanically processed for SPF applications [6]. The significant increase in yield strength at cryogenic temperatures increases plane strain constraint and slip localization and, therefore, leads to a fracture surface which is more planar/brittle. The degree of intergranular splitting was minimal for both alloys.

Specimens of 2090+In, aged for 75 hours at 160 C and tested at room temperature, had a mixed fracture mode of ductile shear and ISB fracture, Fig. 4. The tendency for ISB fracture at room temperature was reflected in the decrease in the relative toughness of the indium bearing material. Low energy ISB fracture may be promoted in these alloys by the reported increase in the T1 number density [7] causing a T1 PFZ in which slip would become localized. A mechanism to account for the decrease in toughness at cryogenic temperatures and with minor addition of indium being investigated.

Conclusions

Results for this period are summarized as follows:

- A mechanism for the increased hardness and strength of 2090+In could be related to increased work hardening.

- For alloys processed according to TMT C, solution heat treated and aged, indium additions to base chemistries promote recrystallization.

- 2090 baseline and 2090+In exhibit a decrease in toughness at cryogenic temperatures, as measured by a decrease in the Kahn tear strength to yield strength ratio.

- Low relative toughnesses are associated with low energy intersubboundary failure. Beneficial splitting does not contribute to sheet toughness for the conditions examined.

Future Plans

Future plans will specifically focus on the following areas:

- Conduct preliminary J-integral testing on select 2090 baseline and 2090+In alloys at Fracture Technology Associates.

- Initiate cryogenic J-integral testing at NASA-LaRC.

- Conduct detailed microstructural analyses of 2090 and 2090+In using transmission electron microscopy.

- Conduct texture analyses of selected sheet and plate alloys.

- Identify the mechanism to account for the decrease in toughness for thin sheet Al-Li alloys at cryogenic temperatures.

References

1. Progress Report, "Environment Assisted Degradation Mechanisms in Advanced Light Metals," Grant No. NAG-1-745-2, Report No. UVA/528266/MS89/103, January, 1989.

2. J.G. Kaufman and M. Holt, "Fracture Characteristics of Aluminum Alloys," Technical Paper No. 18, Alcoa Laboratories, Alcoa Center, PA, 1965.

3. S. Suresh, A.K. Vasudevan, M. Tosten and P.R. Howell, "Microscopic and Macroscopic Aspects of Fracture in Lithium-Containing Aluminum Alloys," Acta.Met., vol.35, 1987, pp. 26-46.

4. K.T.V. Rao, W. Yu and R.O. Ritchie, "Cryogenic Toughness of Commercial Aluminum-Lithium Alloys: Role of Delamination Toughening," Met. Trans., vol. 20A, 1989, pp. 485-497.

5. J. Glazer and J.W. Morris, Jr., "Tensile Properties of Commercial Aluminum-Lithium Alloys at Cryogenic Temperatures," presented at the 1988 ASM Aluminum-Lithium Symposium, Los Angeles.

6. J. Glazer, J.W. Morris, Jr., and T.G. Nieh, "Tensile Behavior of Superplastic Al-Cu-Li-Zr Alloy 2090 at Cryogenic Temperatures," Adv. Cryo. Eng., vol. 34, 1988, pp. 291-298.

7. L.B. Blackburn and E.A Starke, Jr., "Microstructure-Mechanical Property Relationships for Al-Cu-Li-Zr Alloys with Minor Additions of Cadmium, Indium or Tin," to be published in the Proceedings of the Symposium on Light-Weight Alloys for Aerospace Applications, TMS Annual Meeting, Las Vegas, NV, 1989.

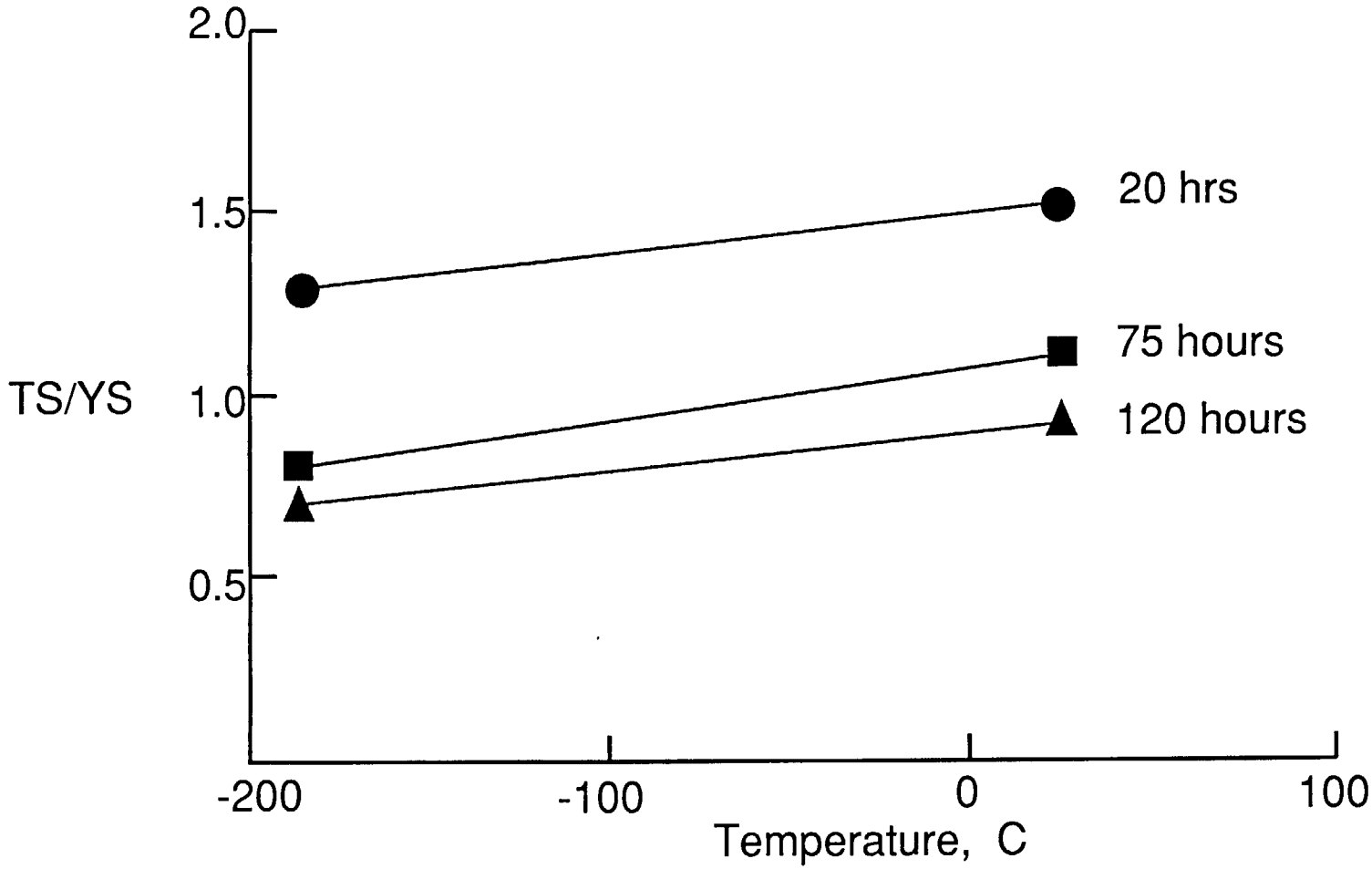

Figure 1 - Tear strength to yield strength ratio of 2090 + In at -185° C and 23° C for various aging times at 160 C.

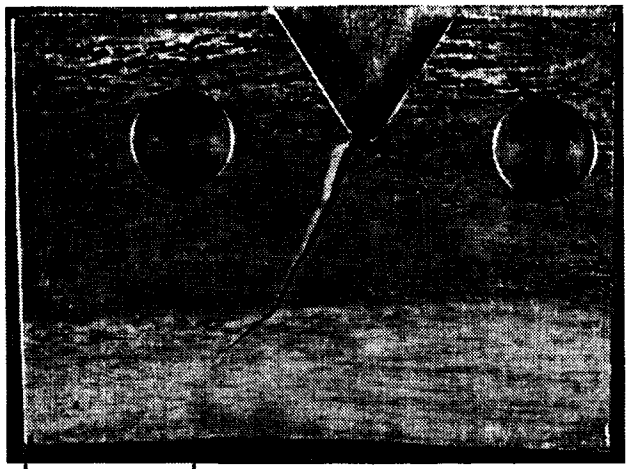

A

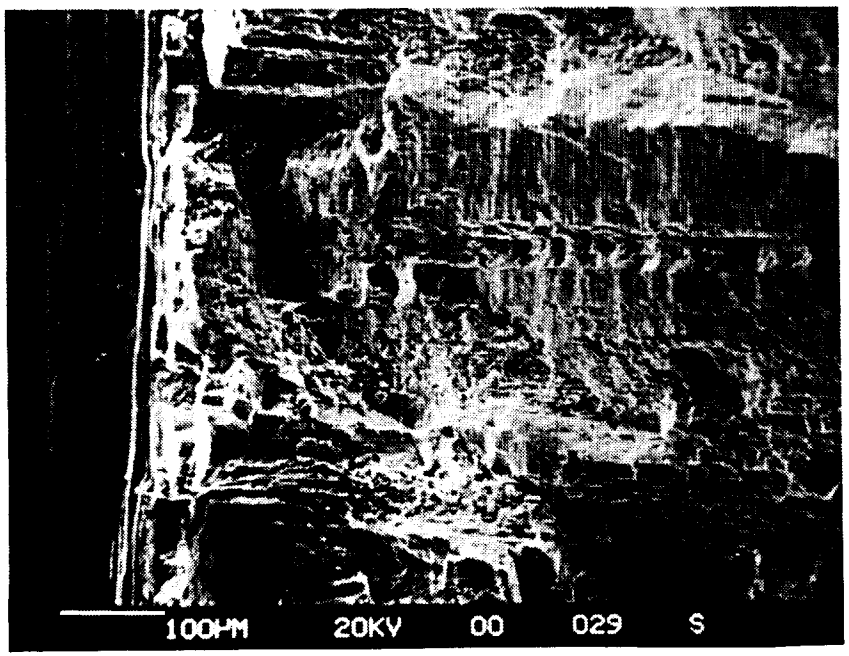

B

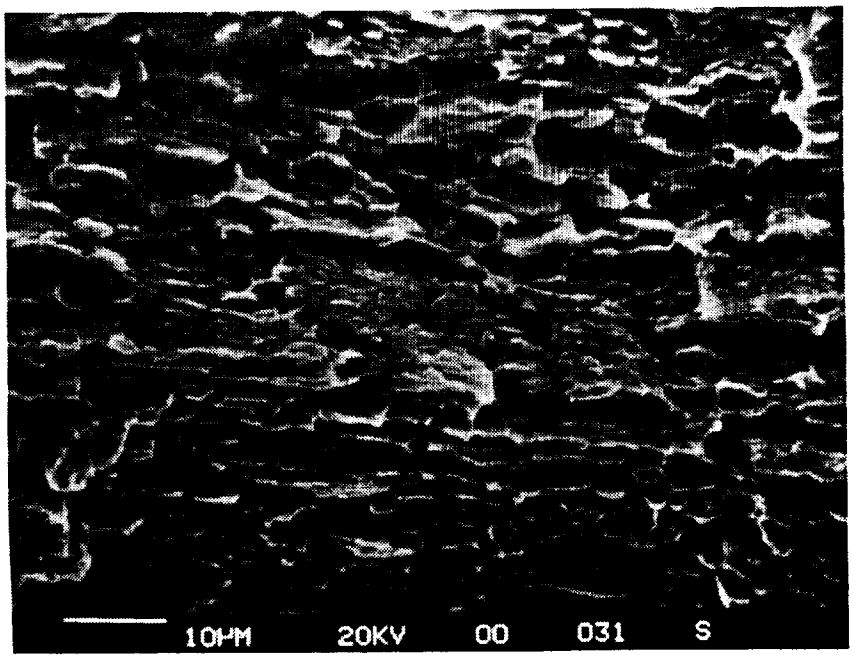

C

Figure 2 - Fracture path and fracture surface morphology of 2090 baseline aged at 160°C for 75 hrs and tested at room temperature.

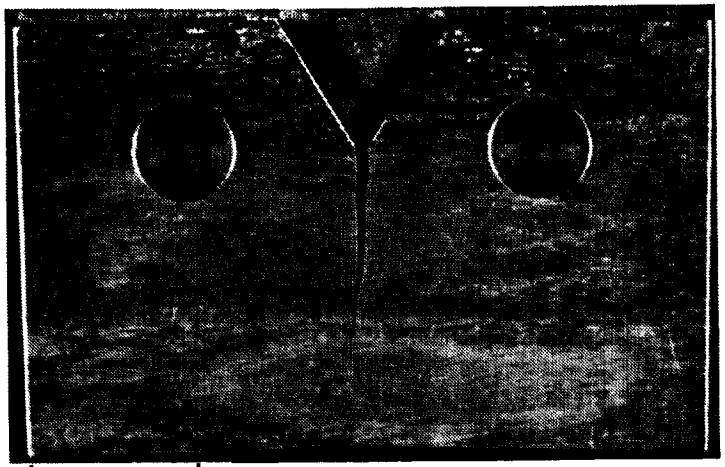

A

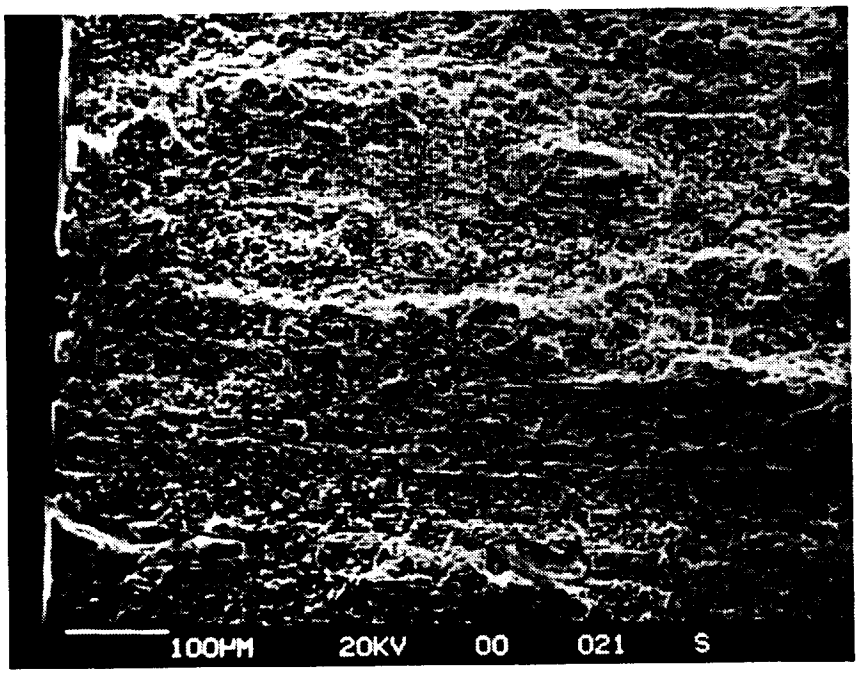

B

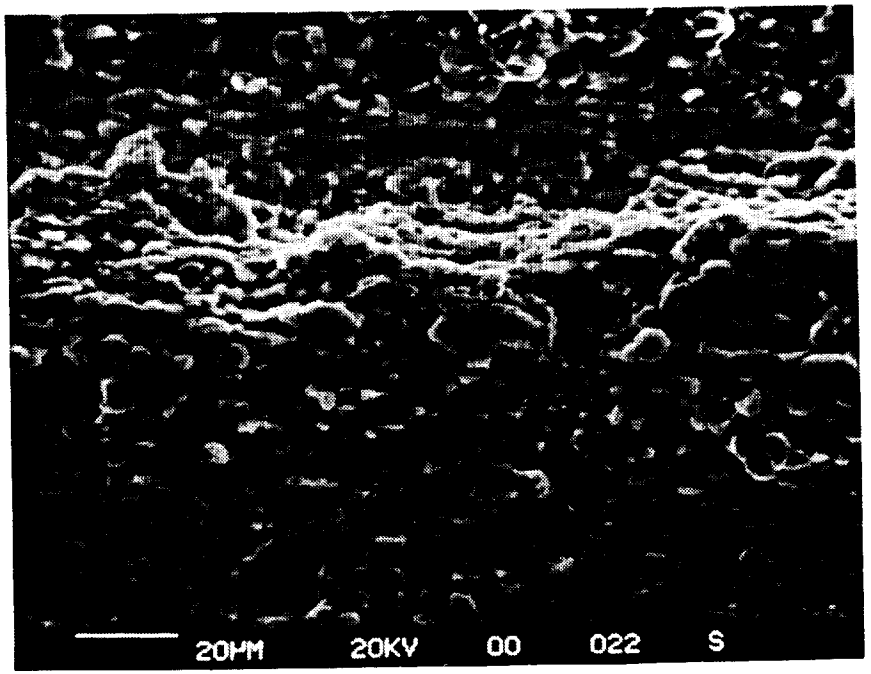

C

Figure 3 - Fracture path and fracture surface morphology of 2090 baseline aged at 160°C for 75 hrs and tested at cryogenic temperatures.

Figure 4 - Fracture surface morphology of 2090 + In aged at 160°C for 75 hrs and tested at room temperature.

Program 4 MEASUREMENTS AND MECHANISMS OF LOCALIZED AQUEOUS CORROSION IN ALUMINUM-LITHIUM ALLOYS

Rudolph G. Buchheit, Jr. and Glenn E. Stoner

Objectives

As cited in previous reports [1,2,3], the objectives of this study have been:

1) to develop new or adapt existing techniques to surmount the difficulties associated with measuring and monitoring localized corrosion processes;

2) to utilize these techniques to understand the processes and mechanisms of localized corrosion and embrittlement of aluminum-lithium alloys.

As a result of discussions with the examination committee at the student's dissertation outline defense held June 23, the primary task of this program will be focused on studies of localized environment chemistry and electrochemistry. The primary aim of the study will be to gain an understanding of how localized environments develop and how they contribute to embrittlement of these alloys. Topics of special interest are:

1) effect of cation hydrolysis on crevice pH

2) effects of solids precipitation on crevice solution chemistry

3) short crack versus long crack chemistry

4) embrittlement in carbonate environments.

Approach

A detailed research proposal is being formulated for submission to the student's advisory committee. The experiments will concentrate in two major areas. These are polarization in simulated crevice environments and simulated crevice experiments.

Polarization of bulk phases in simulated environments will be used to:

* assess the corrosion behavior of phases thought to be important to the localized corrosion process

* form anodic surface films in selected environments which will be characterized *in situ* using electrochemi-

cal impedance spectroscopy and ex situ using auger electron surface analysis and X-ray photoelectron spectroscopy (to be performed at Johns Hopkins University).

A new scanning electron microscope facility is planned to be in operation at U. Va. in the early fall. It will be equipped with a windowless solid state EDS detector which will be able to routinely detect oxygen and carbon. It is anticipated that this facility will also be utilized for ex situ surface analysis.

Goal. Use corrosion rate data from polarization experiments to develop mechanisms for crevice corrosion processes.

Goal. Investigate the cause of the active-passive transition observed in polarization experiments performed with aluminum alloys exposed to lithium carbonate (Li_2CO_3).

Simulated crevice experiments will be performed to measure:

* crevice corrosion current vs. time

* crevice potential vs. time

* crevice pH versus time

in long and short simulated crevices in selected bulk environments. Measured responses obtained from simulated crevice experiments will be compared to responses calculated from chemical and electrochemical equilibrium (initially) or kinetics (ideally).

Goal. Identify chemical and electrochemical processes which dominate the crevice environment in aluminum-lithium alloys.

Results

Corrosion Behavior of T_1 (Al_2CuLi). Two mechanisms have been proposed for the preferential subgrain boundary corrosion of Al-Li-Cu alloys. The first mechanism proposes that T_1 (Al_2CuLi) precipitates on the subgrain boundaries selectively dissolve resulting in preferential subgrain boundary corrosion. The second mechanism proposes that a copper depleted zone forms along subgrain boundaries which is susceptible to corrosion because of the lack of copper.

The objective of this study was to synthesize T_1 in bulk form so that its corrosion behavior could be assessed by conventional electrochemical techniques. The corrosion behavior of the synthesized T_1 was then compared to that of the matrix phase and a copper depleted phase. The proposed mechanisms for subgrain boundary corrosion were evaluated in terms of the measured corrosion behavior of these phases.

Open circuit measurements, cyclic potentiodynamic polarization and corrosion rate determinations were used in this study. Solution heat treated (SHT) 2090 was to simulate the matrix phase, pure aluminum was used to simulate the copper depleted phase (a worst case scenario considering the ennobling effects of copper in aluminum) and the synthesized T_1 was used to simulate the precipitate phase.

The details of the experimental procedures used, results obtained and discussion of the results are presented in the paper appended to this report. A brief summary of the results and conclusions of the study are presented below.

Based on open circuit potential, potentiodynamic polarization and corrosion rate determinations, T_1 is an extremely active phase with a corrosion potential of -1100 mV_{SCE} and a corrosion current of 0.1 mA/cm^2 in 3.5 w/o NaCl solution. The corrosion current of T_1 is roughly two orders of magnitude greater than that for a copper depleted zone of the α-matrix phase in 2090. These data support a mechanism for subgrain boundary corrosion based on selective T_1 dissolution.

Measurements of corrosion rate versus pH for T_1 show that corrosion rate is independent of pH over the range of pH3 to 11.

Visual examination and polarization behavior of bulk T_1 specimens suggest that copper dissolves and then deposits back on the electrode surface during polarization experiments.

Polarization in Carbonate Environments. Moran has shown that constant immersion SCC Time To Failure (TTF) for peak aged 2090 in 0.1 M Li_2CO_3 + 3.5 w/o NaCl is greatly accelerated, but surface attack by pitting is absent [4]. Constant immersion TTF specimens exposed to straight 3.5 w/o NaCl solution gave aggressive surface attack but long times to failure. Several environments were utilized in Moran's study in an attempt to isolate the effects of CO_3^{2-} and Li^+. The compositions and pH values of these environments are listed in Table 1.

In the present investigation, specimens of 1100 aluminum (intended to simulate the α-matrix phase of the alloy) and bulk T_1 (simulating the subgrain boundary phase) were subjected to potentiodynamic polarization in each of the environments listed. Pertinent corrosion data are presented in Table 1.

In general electrochemical polarization results do not provide a reasonable assessment of SCC performance. However, the results from polarization experiments performed on isolated bulk phases present some interesting correlations to constant immersion TTF experiments with peak aged 2090. Polarization data are presented in Table 1. Only the carbonate results are discussed below.

Exposure of peak aged 2090 to a Li_2CO_3/NaCl aqueous environment under constant immersion conditions caused rapid failures (3

of 4 specimens failed in less than 24 hours). Furthermore, the specimens showed almost no surface damage; even after prolonged exposure to the environment. A comparison of passive current densities listed in Table 1 shows that bulk T_1 has a much higher value than 1100 Al. The low corrosion rate of the 1100 Al is consistent with the occurrence of little surface damage in TTF experiments. The rapid corrosion of T_1 is consistent with a subgrain boundary dissolution SCC initiation process which has been proposed to operate in Al-Li-Cu alloys.

A second interesting feature of the polarization data is the existence of an active-passive transition for 1100 Al in the Li_2CO_3/NaCl environment (Figure 1). This type of polarization curve, uncommon in naturally occurring aqueous environments, has also been reported by other workers (5,6).

Polarization experiments for 1100 Al and T_1 in Na_2CO_3/NaCl, pH 10 environments shows that the passive currents are large and nearly equal. In TTF experiments, specimens are severely corroded but withstand breaking for periods greater than 60 days.

These polarization results, taken with TTF experiments, strongly suggest that:

1) localized dissolution plays an important role in accelerating failure by SCC

2) Li_2CO_3 is the primary candidate as the passivating species for α-aluminum in 2090. Passivation of the α-Al phase exacerbates SCC by helping to maintain sharp cracks along subgrain boundaries.

Future work

Bulk Phase Corrosion Experiments. Bulk phase corrosion experiments will be continued with an investigation of the corrosion behavior of the T_2 precipitate phase. While it is known that this phase is less prevalent in 2090 than T_1 in peak aged tempers, it is an important high angle grain boundary phase. Due to its stoichiometry, it is likely that this phase will be as (or more) reactive with aqueous environments as T_1.

The proposed plan is similar to that used in the T_1 study and includes:

1) synthesis and verification of the phase

2) refinement of specimen preparation techniques

3) documentation of corrosion behavior via polarization in standard environments

4) documentation of the variation of corrosion rate versus pH.

Localized Environment Studies. As described above, a detailed research proposal regarding the chemistry and electrochemistry of crevice corrosion in Al-Li-Cu alloys is being formulated for submission to the advisory committee. This proposal will be forwarded to the contract monitors at NASA Langley upon completion and approval by the committee.

References.

1. R.P. Gangloff, G.E. Stoner and R.E. Swanson, "Environment Assisted Degradation Mechanisms in Al-Li Alloys", University of Virginia, Report No. UVA/528266/MS88/101, January, 1988.

2. R.P. Gangloff, G.E. Stoner and R.E. Swanson, "Environment Assisted Degradation Mechanisms in Aluminum-Lithium Alloys", University of Virginia, Report No. UVA/528266/MS88/102, June, 1988.

3. R.P. Gangloff, G.E. Stoner and R.E. Swanson, "Environment Assisted Degradation Mechanisms in Advanced Light Metals", University of Virginia, Report No. UVA/528266/MS89/103, January, 1989.

4. J.P. Moran, "An Investigation of the Mechanisms of Localized Corrosion and Stress Corrosion Cracking of Al-Li-Cu Alloy 2090", Research Summary, University of Virginia, August, 1988.

5. J. Gui, T.M. Devine, Scripta Met., 21, 1987, p. 853.

6. J.G. Craig, R.C. Newman, M.R. Jarrett, N.J.H. Holroyd, "Stress Corrosion Cracking and Pre-Exposure Effects in Al-Li-Cu-Mg Alloy 8090", Third Int. Conf. on Environmental Degradation of Engineering Materials, PSU, University Park, PA, 1987.

Polarization in Carbonate Environments

Environment	pH	E_{CORR} (mV_{SCE})		i_{PASS} ($\mu A/cm^2$)		E_{BR} (mV_{SCE})	
		Al	T_1	Al	T_1	Al	T_1
Li_2CO_3 A	10	-1600	-1180	0.1	40	-600	-720
Li_2CO_3 D	10	-1702	-1100	< 1	40	-	-720
Na_2CO_3 A	7-9	-967	-1001	20	70	-680	-650
Na_2CO_3 A	10	-1611	-1129	500	500	>-500	-750

Table 1. Polarization data for pure aluminum and synthesized bulk T_1 in various chloride, carbonate and sulfate environments.

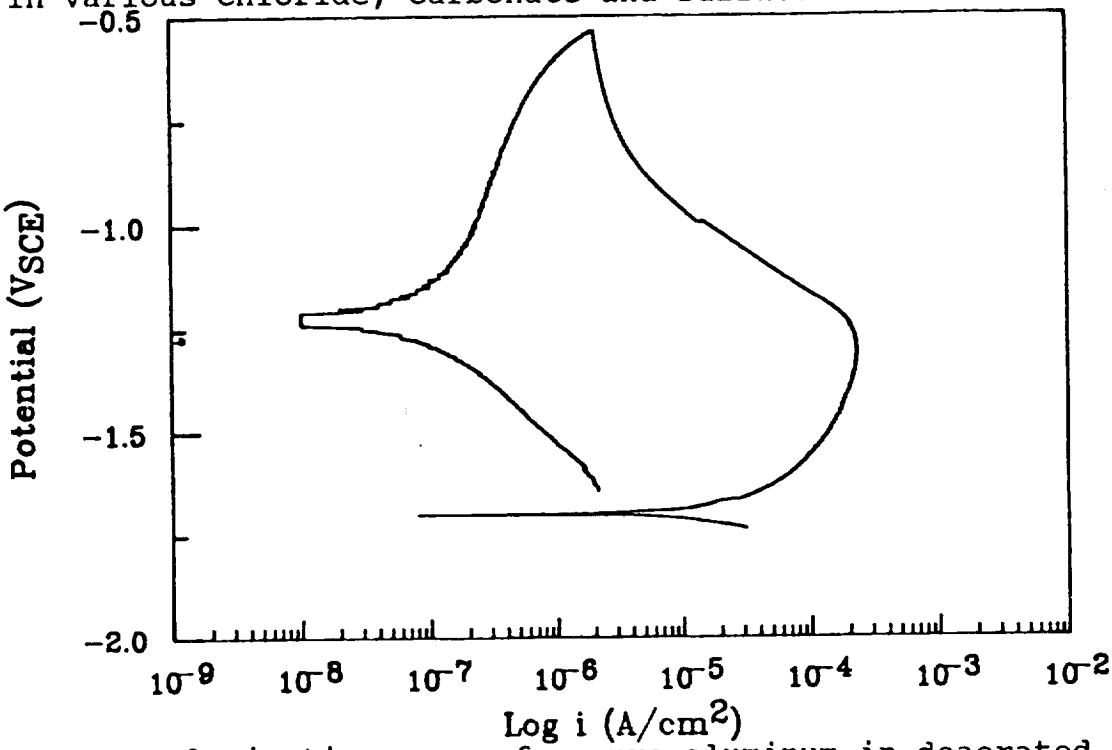

Figure 1. Polarization curve for pure aluminum in deaerated 0.1M Li_2CO_3 + 3.5 w/o NaCl solution.

Program 5

AN INVESTIGATION OF THE LOCALIZED CORROSION AND STRESS CORROSION CRACKING BEHAVIOR OF ALLOY 2090 (Al-Li-Cu)

James P. Moran and Glenn E. Stoner

Introduction

This report represents the second contribution from this project to NASA Grant NAG-1-745. This project is an ongoing dissertation research effort, with an expected completion date of Sept./Oct., 1989. On March 20, the student presented his dissertation outline to his examining committee. The discussions at that time focused on how well the work done to date has addressed the primary objectives of the project, as well as what further work was required to successfully complete the dissertation. A summary of those discussions is being compiled by the student, and will be submitted to the committee in early-July. The following summarizes the research progress made during this reporting period.

Objectives

The objectives of this project are as follows :

1) To characterize the localized corrosion and SCC initiation behavior of alloy 2090.

2) To gain an understanding of the role of localized corrosion phenomena and associated occluded cell environments in the mechanisms of initiation and early-stage propagation of stress corrosion cracks in 2090.

Approach

As outlined in more detail in previous reports [1,2], research efforts have focused in the following areas :

1) Anodic polarization of alloy 2090 and post-exposure microscopy to determine the pitting behavior and localized corrosion surface morphology in selected environments.

2) Constant immersion time-to-failure (TTF) stress corrosion cracking (SCC) experiments in selected $Cl^-/CO_3^=$ environments.

3) Pre-exposure TTF experiments : constant immersion in NaCl for 7 days, followed by exposure to lab air (with and without atmospheric CO_2).

4) Slow strain rate (SSRT) SCC tests in selected environments.

Progress during this reporting period has focused on three areas :

1) Accumulation of SSRT data in NaCl and NaCl/Li_2CO_3 environments. SSRT experiments have been performed on the underaged temper (UA) only, due to the inherent scatter in the peakaged data [1,2].

2) Interpretation of the TTF data reported earlier [1,2,3], with particular interest in the role of CO_2 in the SCC initiation process.

3) Preliminary fractography on SCC specimens.

Results

SLOW STRAIN RATE EXPERIMENTS

The effect of strain rate on the ductility of alloy 2090-UA is illustrated in Figures 1 and 2, for the following environments, respectively: NaCl, applied potential = -715 mV vs. SCE, and NaCl/Li_2CO_3 under free corrosion. Each plot includes the ductility data gathered in dry argon, at a strain rate of $5.4E^{-7}$ /sec. The presence of Li_2CO_3 significantly affects the SSRT behavior, particularly at slow strain rates, where ductility is reduced to zero. Together, these plots represent the two classic curve shapes expected from SSRT testing [4], with the NaCl curve representative of a film dissolution mechanism and the NaCl/Li_2CO_3 curve indicative of hydrogen embrittlement.

Consider first the NaCl curve. Although only roughly defined, the curve reveals a trough of minimum ductility, with increased ductility at both slower and faster strain rates. As the strain rate is decreased from its maximum, increased time is available for dissolution to occur, per film rupture event. This increases SC crack growth rates and decreases ductility [4]. Eventually (at strain rates lower then roughly $2E^{-6}$), the film rupture frequency (i.e., strain rate) becomes sufficiently slow such that selective dissolution is not maintained at the crack tip and competitive dissolution of crack tip walls ensues. This produces a blunted fissure, effectively reducing the stress concentration and SC crack growth rates, and increasing ductility.

For NaCl/Li_2CO_3, on the other hand, the continual decrease in ductility is similar to that observed for hydrogen embrittlement (4). Decreasing the strain rate increases the specimen exposure time, thereby allowing greater accumulation of hydrogen and its associated detrimental effects on ductility. There is, however, one problem with this hypothesis. The specimens exposed at the slower strain rates are fracturing very early along the

elastic portion of the stress-strain curve (as low as 10% of yield). Accordingly, the overall exposure times are only 2-3 times that of the faster strain rates, where some ductility is maintained. Therefore, the greatly increased exposure times required to increase cummulative hydrogen damage are not attained, suggesting that hydrogen is not the predominant mechanism.

As an alternative to hydrogen embrittlement, an argument can be made for a film dissolution mechanism. The passivating effects of Li_2CO_3 have been documented by this student [1-3, and see below] and other researchers [8]. At slower strain rates, the presence of Li_2CO_3 will improve crack wall passivity, thereby maintaining a sharp crack tip, contrary to the straight NaCl case, where blunted crack tips are produced.

Further experiments are required to clarify the roles of film rupture and hydrogen. For example, unstressed specimens could be exposed to $NaCl/Li_2CO_3$ for long time periods, then pulled under inert SSRT conditions. Ductility decreases under these conditions would suggest that hydrogen does dominate the fracture process.

ROLE OF CO_2 AND CARBONATES IN THE SCC CRACK INITIATION PROCESS

This investigation was initiated based on a study performed by Craig et al. [5,6]. The pertinent aspects of the work performed by Craig, et al. [5,6] are reviewed in the Fall '88 report (pg. 25) [1]. In summary they found that 8090, constantly immersed in NaCl solution, would not stress corrode. Removal from solution after several days and placement in lab air resulted in very quick fracture, while removal and placement in a CO_2-free environment did not produce fracture.

The experiments discussed above were repeated on 2090 by this author, and the results were perfectly duplicated. They are summarized in previous reports [1,2,3]. Constant immersion in NaCl containing 0.1M Li_2CO_3 yielded greatly accelerated failure times, relative to straight NaCl. Those immersed in straight NaCl suffered from severe pitting and surface discoloration, while those in Li_2CO_3 exhibited no evidence of macroscopic localized corrosion.

To isolate the role of $CO_3^=$, 0.1M Na_2CO_3 was substituted for the Li_2CO_3. The results were dramatically different. Severe surface attack and discoloration occurred almost immediately, and fracture times were significantly increased. Many samples did not fracture after 30 days (similar to straight NaCl). Clearly, there is a major difference between these two cations. To isolate the role of Li^-, LiCl was added to NaCl solution (pH=10). The NaCl concentration was altered to keep a consistent Cl^- concentration. SCC times to failure for this environment slight-

ly increased, relative to NaCl, but were still far greater than Li_2CO_3.

Perhaps the most significant result of this work is the effect of atmospheric CO_2 on the SCC behavior of pre-exposed specimens. With this in mind, the following discussion will propose a series of critical events occurring during the pre-exposure process, with emphasis on the role of CO_2 in the formation of an SC crack. A more detailed discussion is presented in reference 3.

Upon immersion in NaCl, intergranular fissures initiate at surface flaws and propagate inter-subgranularly. In the presence of a bulk solution, oxygen reduction on the external surfaces will be the primary cathodic reaction. Therefore, cathodic consumption of H^+ within the fissure will be minimal, and the occluded pH should be governed by Al(III) hydrolysis equilibria (see Fig. 3). These equilibria predict a steady-state pH=4, as measured (Fig. 2, ref. 3). The rate of metal dissolution should continue to increase as the pH decreases, thereby inhibiting the formation of a sharp crack tip.

Removal of the bulk solution forces the cathodic reaction (hydrogen evolution) to occur within the fissures. The consumption of H^+ gradually increases the fissure pH, as measured (Fig. 3, ref. 3). As pH increases, the solubility of Al (III) decreases (see Fig. 3), most likely promoting precipitation of $Al(OH)_3$. As the pH rises above 7 (in the presence of Li^+), Al(III) hydrolysis equilibria predict the precipitation of the insoluble $LiAlO_2$.

Although the above series of events predicts precipitation of at least two species, it is unlikely that these species play a major role in the passivation of fissures, since their precipitation will occur with or without the presence of atmospheric CO_2. On the other hand, atmospheric CO_2 <u>will</u> directly affect the concentrations of dissolved CO_2 and its ionic species (see Fig. 4). As the pH increases (due to hydrogen evolution), the percentage of CO_2 in its ionic forms will increase. This is where the presence of atmospheric CO_2 becomes critical. Figure 5 predicts the total concentrations of dissolved CO_2 species with and without exposure to atmospheric CO_2. From these calculations, it is evident that as the alkalinity of a fissure increases, the concentrations of bicarbonate and carbonate will be orders of magnitude greater in the presence of atmospheric CO_2.

Given the fact that atmospheric CO_2 will significantly increase the carbonate/bicarbonate concentration within fissures, the next issue to be addressed is the role of this increased concentration in the SC initiation process. The evidence suggests a mechanism of fissure passivation by precipitation of Li_2CO_3. Upon removal of the bulk solution, continued metal dissolution should increase the local Li^+ concentration ($[Li^+]$), and exposure to CO_2 will increase $[CO_3^=]$. Given the low solubility of

Li_2CO_3 (pK_p=2.74) [7], it is likely that precipitation of Li_2CO_3 could occur, and its passivating nature has been documented by this student [1-3] and other researchers [8].

As an example, consider a local pH of 10. Without CO_2, precipitation is predicted at $[Li^+]$ = 13 Molar; however, exposure to CO_2 would allow precipitation at $[Li^+]$ = 0.1 Molar. Unfortunately, this lithium concentration is roughly 50 times higher than measured values for 8090 crevices [9], and a high pH is not achieved (Fig. 3, ref. 3). Nevertheless, it is likely that the local pH and lithium concentration at the base of a fissure could be greater than the measured averages, thus exceeding the local solubility. In addition, the high total ionic concentration will tend to decrease the solubility [7].

The constant immersion data is consistent with this argument. Exposure to NaCl/LiCl did not promote failure. NaCl/Na_2CO_3 also did not promote failure, and the solubility for Na_2CO_3 is 2-3 orders of magnitude higher than Li_2CO_3 (7). Neither lithium alone nor carbonate (and its buffered pH) alone was a sufficient requisite for the passivity of fissures.

FRACTOGRAPHY OF SCC SPECIMENS

Preliminary fractography of TTF specimens has revealed several points of interest. Firstly, pre-exposure specimens (i.e., immersion in NaCl, followed by lab air exposure to failure) revealed the presence of a large pit at the smooth bar surface, with a smooth, corroded region (SCC) emanating from it. This morphology supports the arguments presented above, namely that SCC cracks initiate from blunted fissures/pits under proper environmental conditions. Secondly, the SC crack surface morphology for pre-exposure specimens is very similar in appearance to those specimens immersed in NaCl/Li_2CO_3. Finally, the values of approximated stress intensities for observed SC cracks were consistent with reported fracture toughness values for 2090, short transverse.

Although these results are encouraging, it must be stressed that they are preliminary. An extensive fractographic investigation will be performed during the upcoming reporting period.

Summary

Progress during this reporting period has focused on investigating the role of CO_2 and its associated ionic species in the SCC initiation processes. An argument for improved passivation of actively corroding fissures (via precipitation of Li_2CO_3), thereby producing a sharp crack tip, was presented. Both constant immersion TTF SCC and SSRT experiments offer experimental support for this argument.

Future Work

Although there is a great deal of evidence to support the mechanisms proposed in the report, several further experiments are planned to solidify the argument, and complete the dissertation. They are summarized as follows:

1. **Microscopic examination.** This will include optical cross-sections of tensile bars to observe blunted fissures and hopefully cracks emanating from them. Also, extensive fractography needs to be performed on both TTF and SSRT specimens.

2. **In-Situ experiments.** In a cooperative effort with R. Buchheit, we will attempt to optically view (using a long working distance microscope) the growth of cracks from predetermined blunt fissures, using the environments of interest discussed above.

3. **Complete SSRT work.** This will include the unstressed pre-exposure experiments discussed above, to aid in clarifying the role of hydrogen.

4. **Complete dissertation.** The Research Summary [1] compiled in 1988 will serve as the foundation of the dissertation. The literature review needs to be updated, and expanded; the results gathered over the last year need to be included; and the discussion section needs to be greatly enhanced.

References

1. J.P. Moran; "An Investigation of the Mechanisms of Localized Corrosion and Stress Corrosion Cracking of Alloy 2090 - A Literature Review and Research Summary"; A progress report submitted to the dissertation committee. The University of Virginia. September, 1988.

2. R.P. Gangloff, G.E. Stoner, R.E. Swanson, "Environment Assisted Degradation Mechanisms in Advanced Light Metals", Univ. of Virginia, Report No. UVA/528266/MS89/103, Jan., 1989.

3. J.P. Moran, G.E. Stoner, "Solution Chemistry Effects on the Stress Corrosion Cracking Behavior of Alloy 2090 and Alloy 2024", submitted to the 5th Int'l Conf. on Al-Li Alloys, Williamsburg, VA, March, 1989.

4. C.D. Kim, B.E. Wilde; Stress Corrosion Cracking - The Slow Strain Rate Technique, ASTM STP 665, 1979, G.M. Ugainsky, ed., pg. 97.

5. J.G. Craig, R.C. Newman, M.R. Jarret and N.J.H Holroyd; Conference Proceedings of the International Conference of

Environmental Degradation of Engineering Materials, Penn. State Univ., 1987.

6. J.G. Craig, R.C. Newman, M.R. Jarret and N.J.H. Holroyd; Pro-ceedings of the Fourth International Al-Li Conference, Paris, June, 1987.

7. **Lange's Handbook of Chemistry**, J.A. Dean, ed., McGraw-Hill.

8. J. Gui and T.M. Devine, **Scripta Met.**, 21, 1987, pp. 853-857.

9. N.J.H. Holroyd, G.M. Scamans and R. Herrman, **Corrosion Chemistry Within Pits, Crevices and Cracks**, A. Turnbull, ed., HMSO, London, 1987, pp. 495-511.

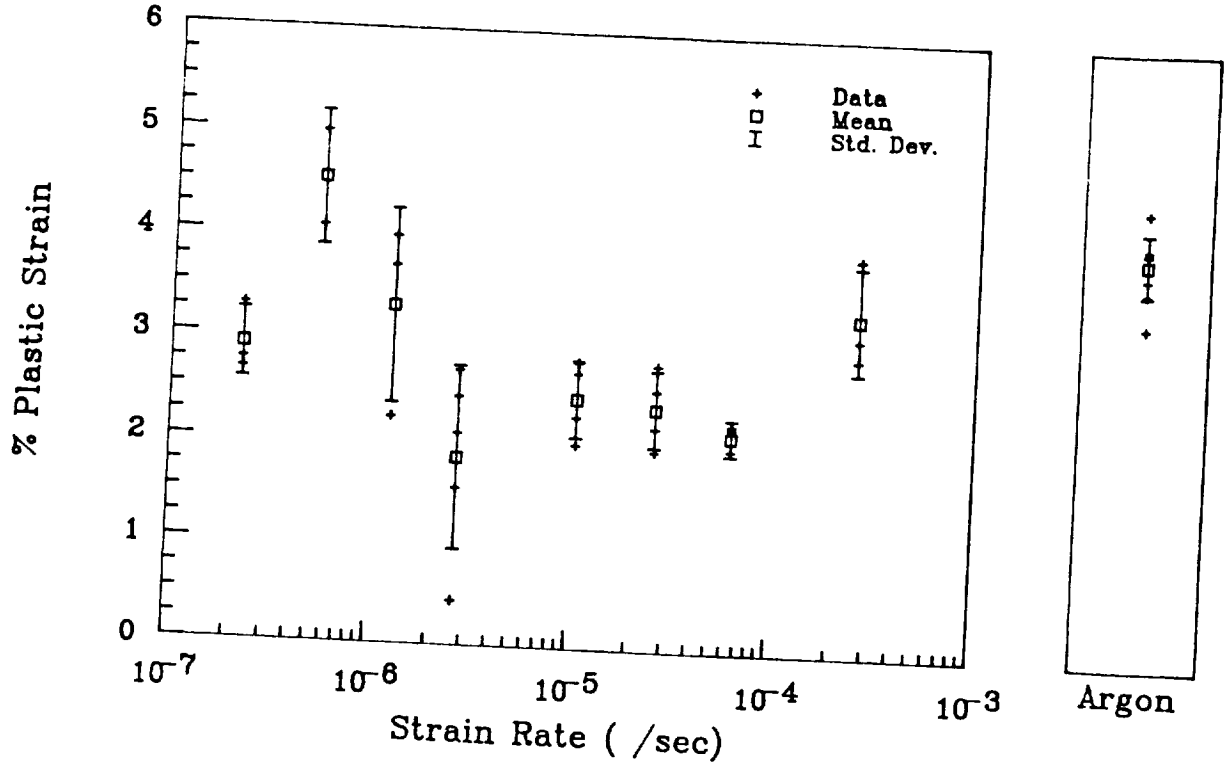

Figure 1 : Slow strain rate SCC data for alloy 2090, underaged. Environment = Deaerated 3.5w/o NaCl, applied potential = -715 mV vs. SCE. Solution pH=6-7.

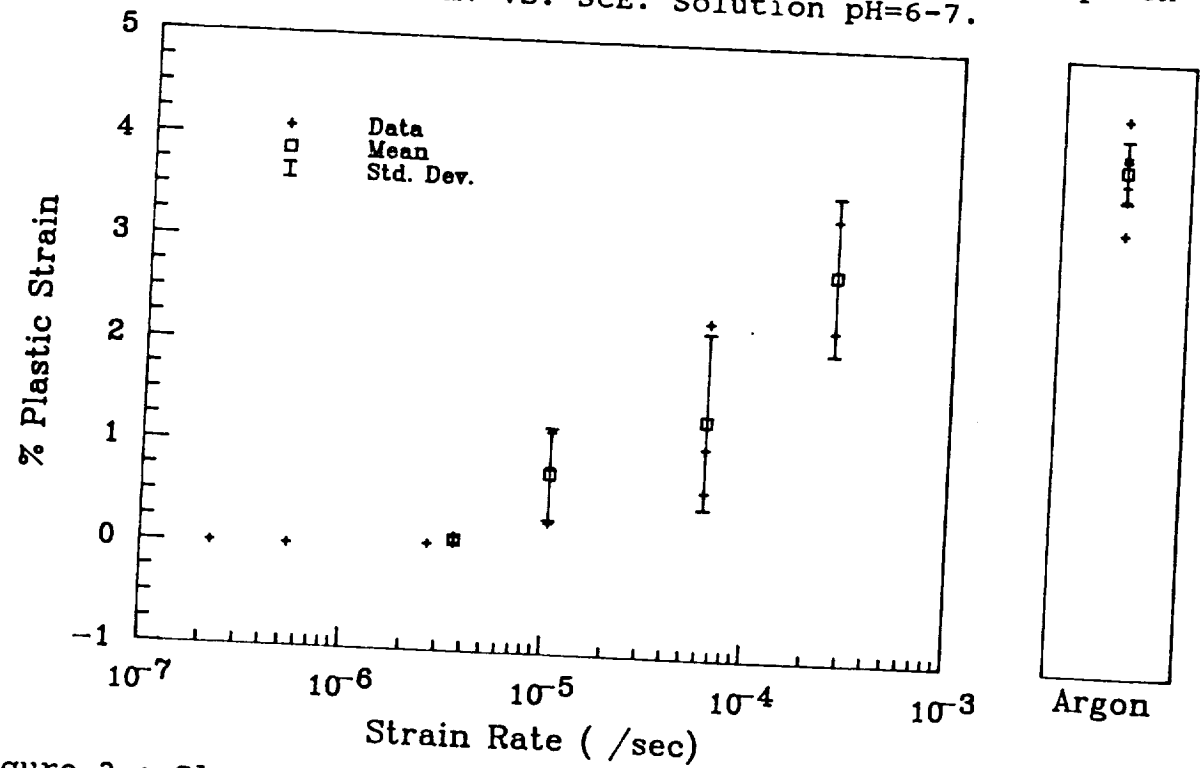

Figure 2 : Slow strain rate SCC data for alloy 2090, underaged. Environment = Aeaerated 3.5w/o NaCl/0.1M Li_2CO_3, at the free corrosion potential (typically -680 mV vs. SCE). Solution pH=10.

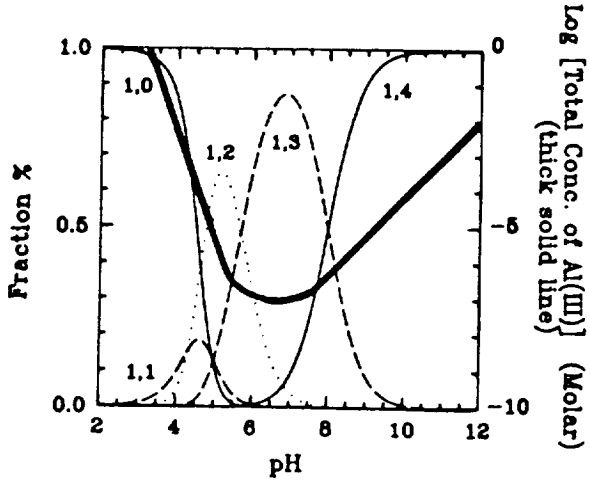

Figure 3. Stability diagram illustrating the distribution of mononuclear Al(III) hydrolysis products $Al_x(OH)_y^{(3x-y)+}$. The thick line is the total solubility of Al(III) (12).

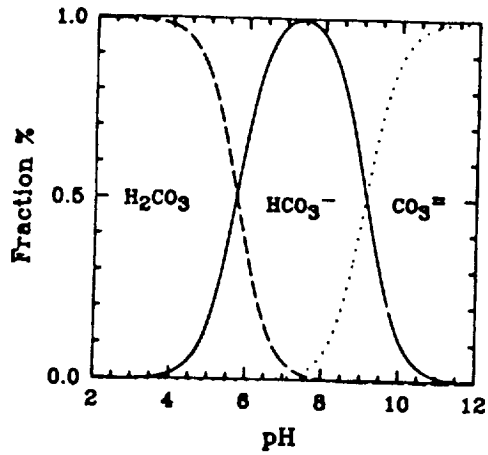

Figure 4. Stability diagram illustrating the distribution of species derived from dissolved CO_2 in seawater (15). (H_2CO_3 is equivalent to CO_2).

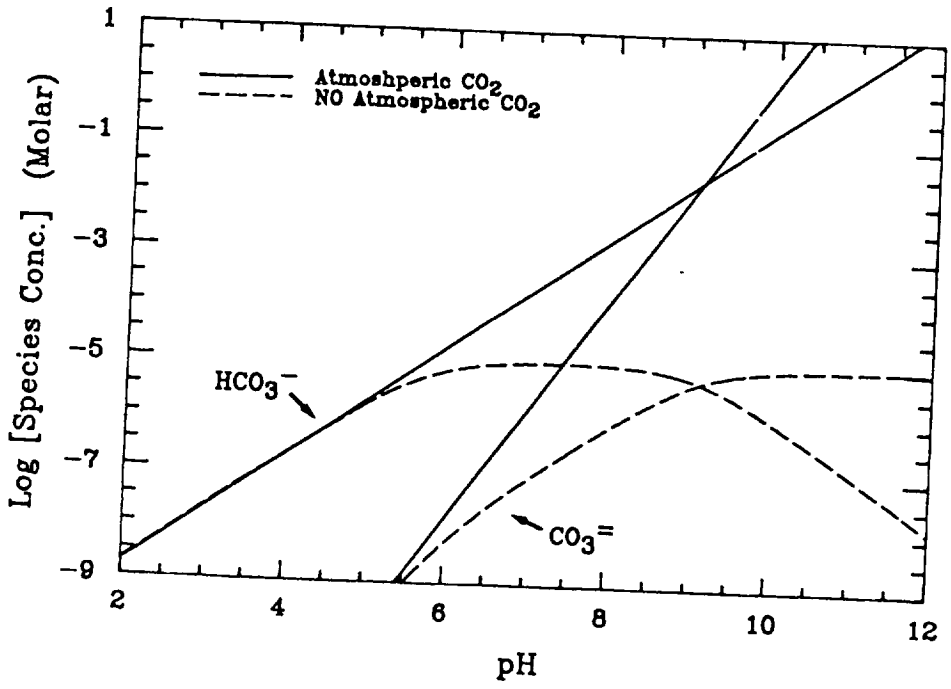

Figure 5. The calculated equilibrium concentrations of the dissociated ions of dissolved CO_2 in seawater, with and without exposure to atmospheric CO_2 (saturated and unsaturated respectively)

Program 6

DEFORMATION AND FRACTURE OF ALUMINUM-LITHIUM ALLOYS: THE EFFECT OF DISSOLVED HYDROGEN

Semiannual Progress Report

Submitted to the
NASA Langley Research Center

by

Department of Materials Engineering
Virginia Polytechnic Institute
and State University
Blacksburg, VA 24061

Proposal No. 88-0883-01
VPI Project No. 230-11-110F-108-402306-1

Principal Investigator:
R. E. Swanson

Graduate Student

F. Rivet

Report Period: 1/1/89-6/30/89

OBJECTIVE

The objective of this study is to characterize and understand the effects of hydrogen on the deformation and fracture behavior of 2090 and 2219, especially at low temperatures.

APPROACH

As outlined in our previous report [1], research efforts have focused on the following areas:

1. Evaluate various methods for cathodic charging;
2. Evaluate effect of temperature on fracture behavior in Charpy tests;
3. Investigate stress state effects in deformation and fracture processes.

HYDROGEN CHARGING STUDIES

Both 2219 and 2090 alloys have been sectioned and mounted in a red Bakelite powder. Holes were drilled to allow for electrical leads to be attached to the specimens. The samples were ground to 600 grit paper and polished using 1 mm diamond paste. Both potentiostatic and potentiodynamic tests were performed on an EG&G Model 342 test system.

Test specimens were cathodically charged using the guidelines proposed by Dull and Raymond [2], and several aqueous solution were tested. The tests have been performed using deionized water mixed with HCl, H_2SO_4, and also NaOH. The pH values were varied and tests were run with or without salt added. Prior to the potentiostatic experiments, we constructed potentiodynamic curves in order to determine the corrosion potentials.

Initially, a cathodic overpotential of -300 mV was applied to the samples. In each case, pitting corrosion damage formed at the surface of the sample after a very short time (from 5 to 15 minutes depending on the pH of the solution). Then, following a paper presented by Dr. S. S. Kim [3], a potential of -3 volts in a solution of 0.04N HCl was used. Testing the samples in that condition seems to give no macrodamage at the surface. New experiments are now being performed to analyze the microdamage and to determine the concentration of hydrogen for various charging times. In order to analyze the microdamage, we are using an optical roughness analyzer which provides results as shown in Figure 1. Figure 1a shows the two-dimensional view of the surface. A statistical analysis is also given with the values of roughness parameters, including RMS, RA, radius of curvature, radius of cylinder, wavelengths, and the maximum difference between valleys and peaks. Figure 1b shows the same analysis but for a three-dimensional view. Figure 1c shows an analysis of the

ten deeper valleys and the ten higher peaks. These figures show results for a sample ready to be charged. A comparison of these results with those after charging in the HCl solution (as well as others) will be useful in assessing the extent of surface damage. SEM will be used in order to confirm the results from this experiment. Two aqueous solutions have been chosen for the future tests: 0.04 N HCl, and also a 0.1N NaOH solution containing a small amount of As_2O_3 as hydrogen recombination poison [4].

In parallel to the roughness analysis, some other tests will be done to measure the amount of hydrogen as a function of charging time. SIMS or gas chromatography will be used for the measurements.

CHARPY IMPACT TESTS

Charpy samples from the 2090 alloy in the peak age condition were machined with dimensions of 55x10x10 mm. A notch of 2 mm depth was cut with a notch root radius of .25 mm for the four orientations L-T, T-L, L-S, and T-S. The samples were heated in an air furnace to various temperatures prior to testing with a GRC Model 730-I instrumented impact test machine, with a data acquisition and analysis system running on an IBM-PC. This system allows for the separation of the total impact energy into initiation and propagation components [5].

Two temperatures were tested to evaluate the effect of orientation: 25°C (70°F) and 200°C (392°F). The results are presented in Figure 2. The energy for crack initiation seems to be virtually the same for three orientations (Figure 2a), from 1 to 3 ft-lb for both temperatures. The initiation energy at 25°C for the LS orientation is somewhat higher than for the others. At 200°C, the initiation energy for the LS orientation is somewhat lower than for the other orientations. The propagation energy for the L-S orientation is much greater than for the others, with the T-S orientation having a somewhat greater resistance than T-L or L-T (Figure 2b). The propagation energy curves are very similar to the total energy curves (Figure 2c). Moreover, the L-S samples did not completely break as shown in Figure 3. The failure mode of the T-S orientation was similar to that of the L-S samples, but total separation occurred for T-S. Fracture in both of these orientations proceeded by ductile intergranular separation along the short transverse plane of the pancake-shaped grains.

Because of the pancake-shaped grains, all four orientations showed substantial tearing along grain boundaries. The T-L and L-T orientations have been used for further impact studies. Tests were carried out for the T-L and L-T orientations for additional temperatures; 25°C, 200°C, 300°C, 350°C, 400°C, and 500*C. Figure 4 shows a dramatic increase in total impact energy at about 350°C. We are evaluating these specimens for possible microstructural changes. We are currently conducting tests at low temperatures (from -200 to 0°C). Because of the loading

orientation in storage tank applications, these tests will focus on L-S and T-S orientations.

HEAT TREATMENT EXPERIMENTS

Heat treatment tests have been performed on the 2219 alloy in order to choose the best conditions of time and temperature for the UA, PA, and OA conditions. We solution heat treated the 8x8x8 mm samples at a temperature of 435°C for one hour before quenching into room temperature water, followed by room temperature aging for one week. Microhardness tests (VHN) were used to follow the change in mechanical properties of the alloy after heat treatment. Figure 5 shows the microhardness results plotted as a function of aging time and temperature. It appears that two hardening peaks exist for this alloy, the first at a temperature of 205°C for a time of 31 minutes and the second at the same temperature and for a time of 16 hours and 40 minutes. From these results, the peak age condition was shown to result from aging for a time of 16 hours and 40 minutes at a temperature of 205°C. Additional work is being done in order to confirm those results, since Alcoa has informed us that the peakage condition occurs with aging at 177°C for 18 hours.

FUTURE WORKS

Following these preparatory tests, and upon receipt of the new materials provided by Alcoa, (2090, 2090+In, and 2219 alloys), mechanical tests will be started on charged and uncharged specimens. These experiments will include Charpy impact, disk rupture, and stress state tests.

The Charpy impact tests will be performed in order to determine the effect of temperature on the hydrogen embrittlement for the uniaxial direction. The stress state tests will be performed with two holes into the sample, and for various orientations of the holes to vary fracture mode and to analyze the effect of hydrostatic stress with or without hydrogen. The disk rupture, or biaxial, test will simulate the application for high pressure tanks. The disk rupture test system has been upgraded with a Linear Variable Displacement Transducer (LVDT) in order to follow the evolution of the deformation with time and with pressure applied to the sample.

REFERENCES

1. R. P. Gangloff, G. E. Stoner, R. E. Swanson, "Environment Assisted Degradation Mechanisms in Al-Li Alloys", University of Virginia, Report No. UVA/528266/MS89/103, January 1989.

2. D. L. Dull and Louis Raymond, "Hydrogen Embrittlement Testing", Louis Raymond (ed.), STP 547, ASTM, Philadelphia, PA, June 1973, pp. 30-49.

3. K. S. Shin, S. S. Kim and Y. Ishida, "Hydrogen Embrittlement of 2090 Al-Li Alloy", 5th International Aluminum-Lithium Conference, to be published.

4. S. S. Kim, E. W. Lee and K. S. Shin, "Effect of Cathodic Hydrogen Charging on Tensile Properties of 2090 Al-Li Alloy", Scripta Metallurgica, 1988, vol. 22, pp. 1831-1834.

5. ASTM E23-82, "Standard Methods for Notched Bar Impact Testing of Metallic Materials", ASTM, vol. 03.01, 1984, pp. 210-233.

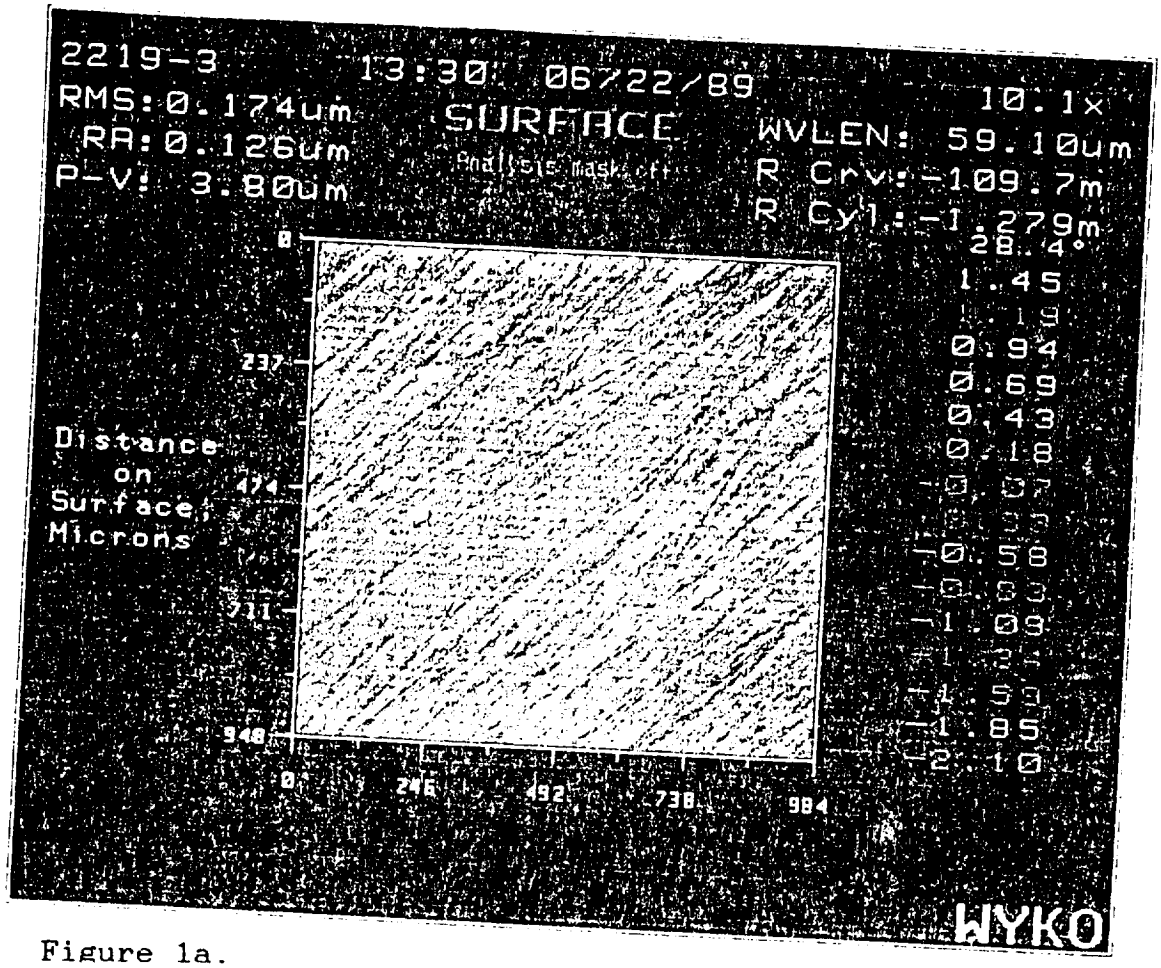

Figure 1a.

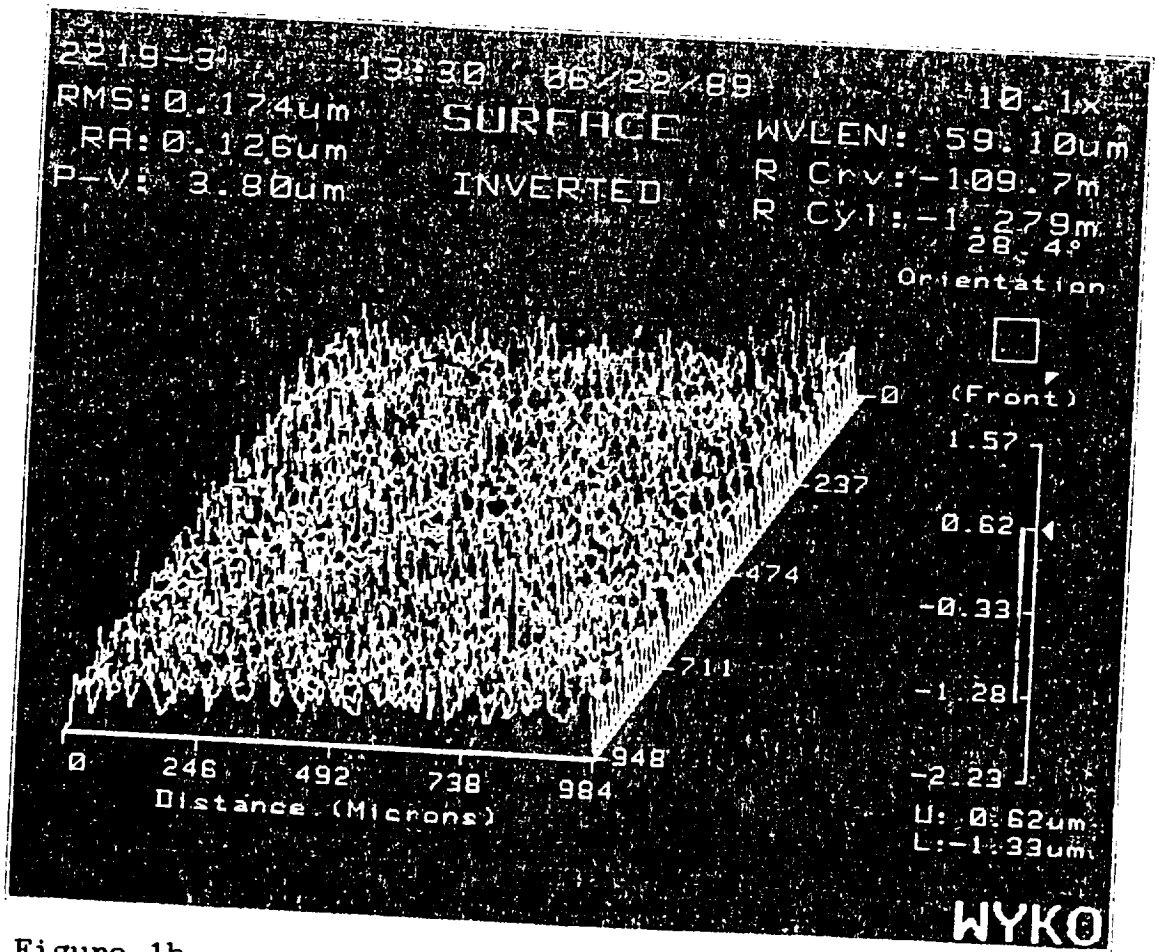

Figure 1b.

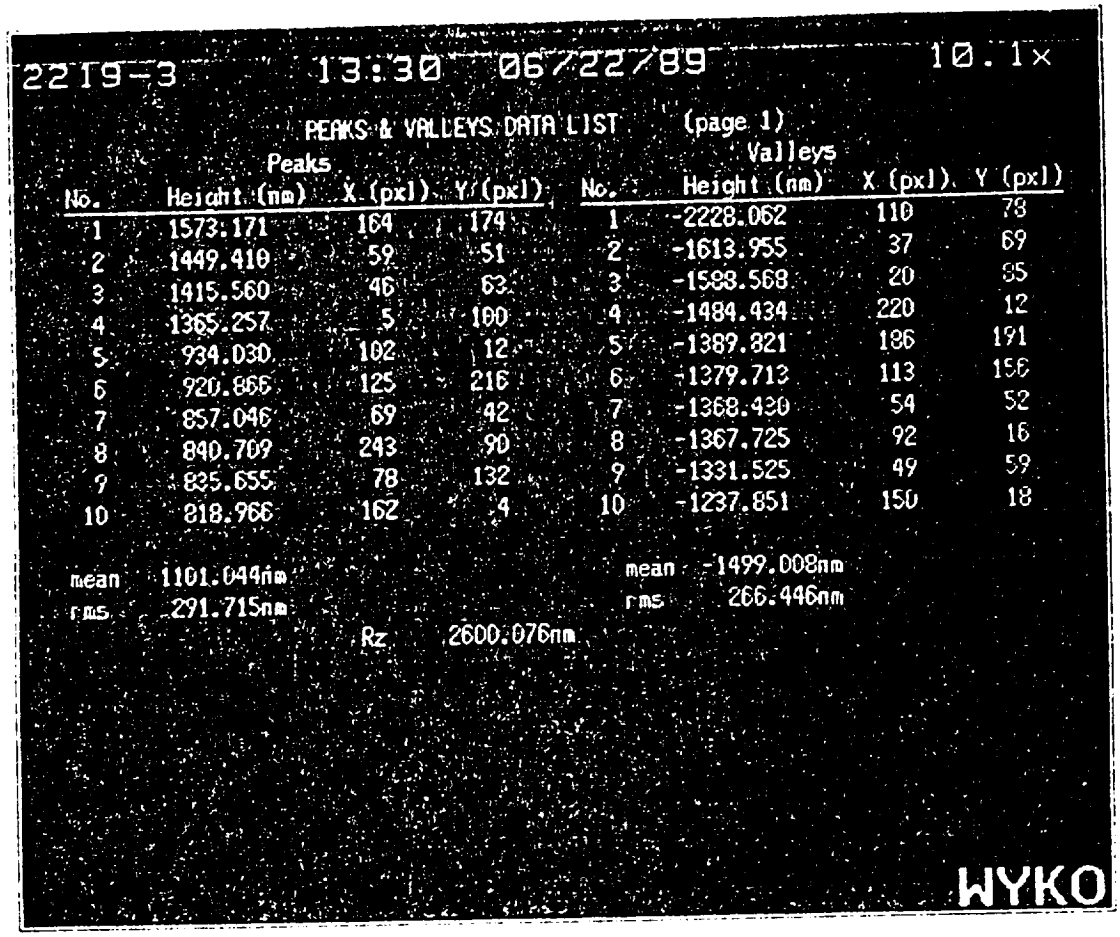

Figure 1c.

Figure 1: Roughness Analysis of 2219 Sample Before Being Cathodically Charged.

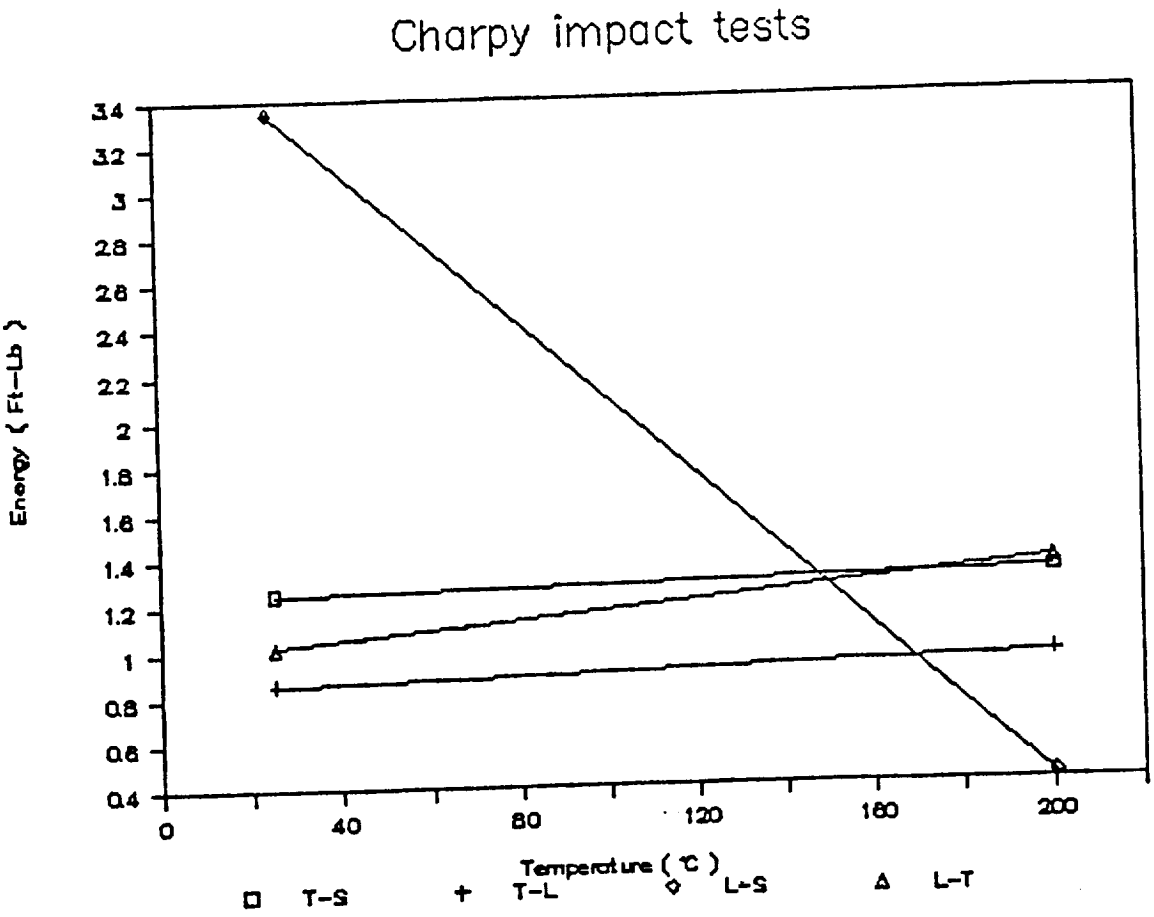

Figure 2a: Charpy Initiation Energy for Fracture of Peak Aged 2090 Al.

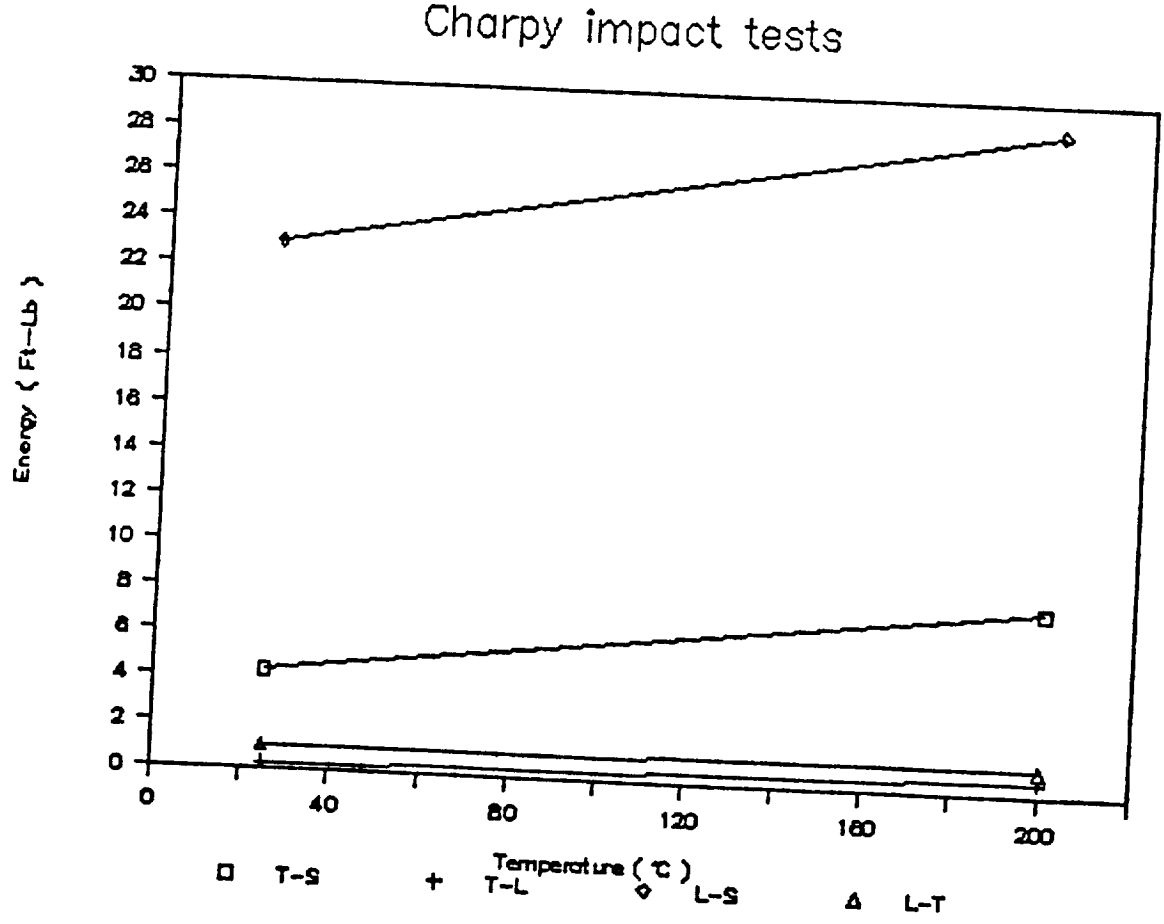

Figure 2b: Charpy Propagation Energy for Fracture of Peak Aged 2090 Al.

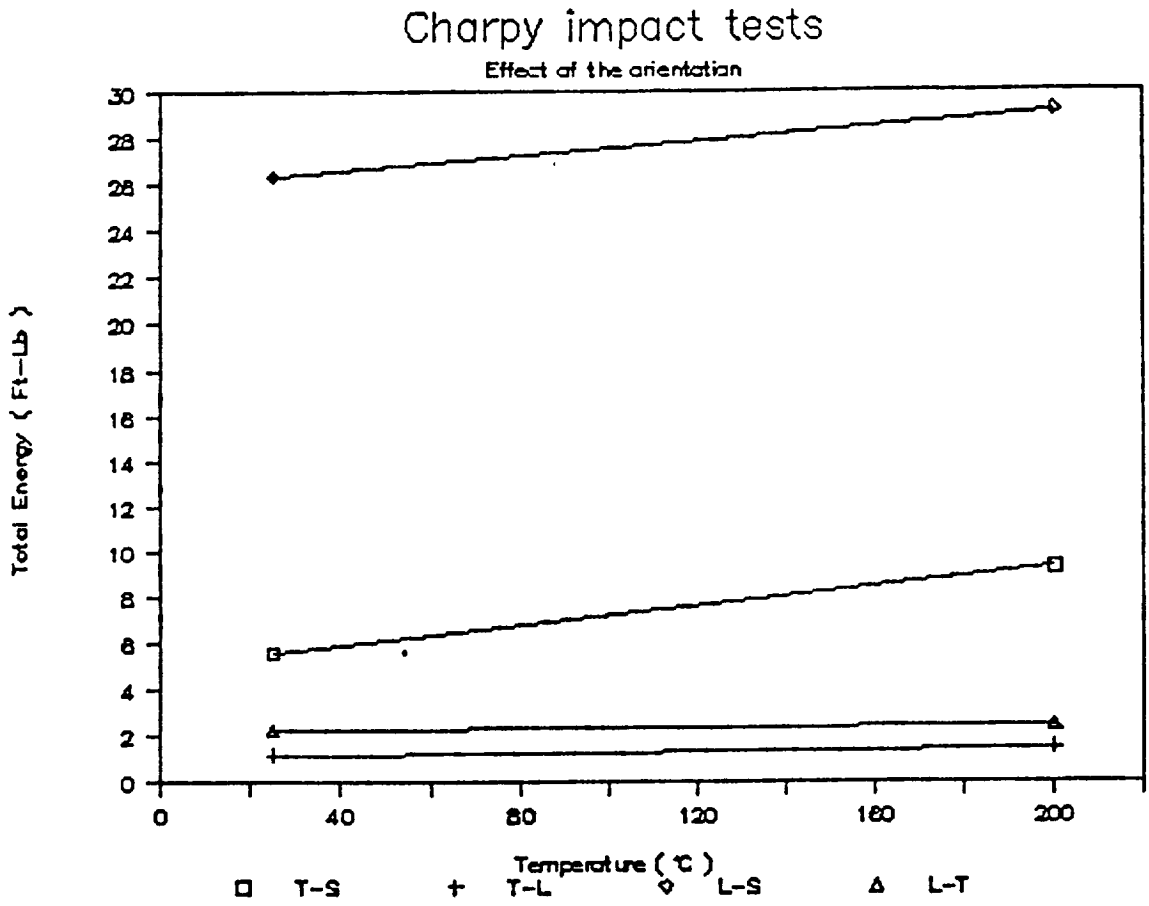

Figure 2c: Total Charpy Energy for Fracture of Peak Aged 2090 Al.

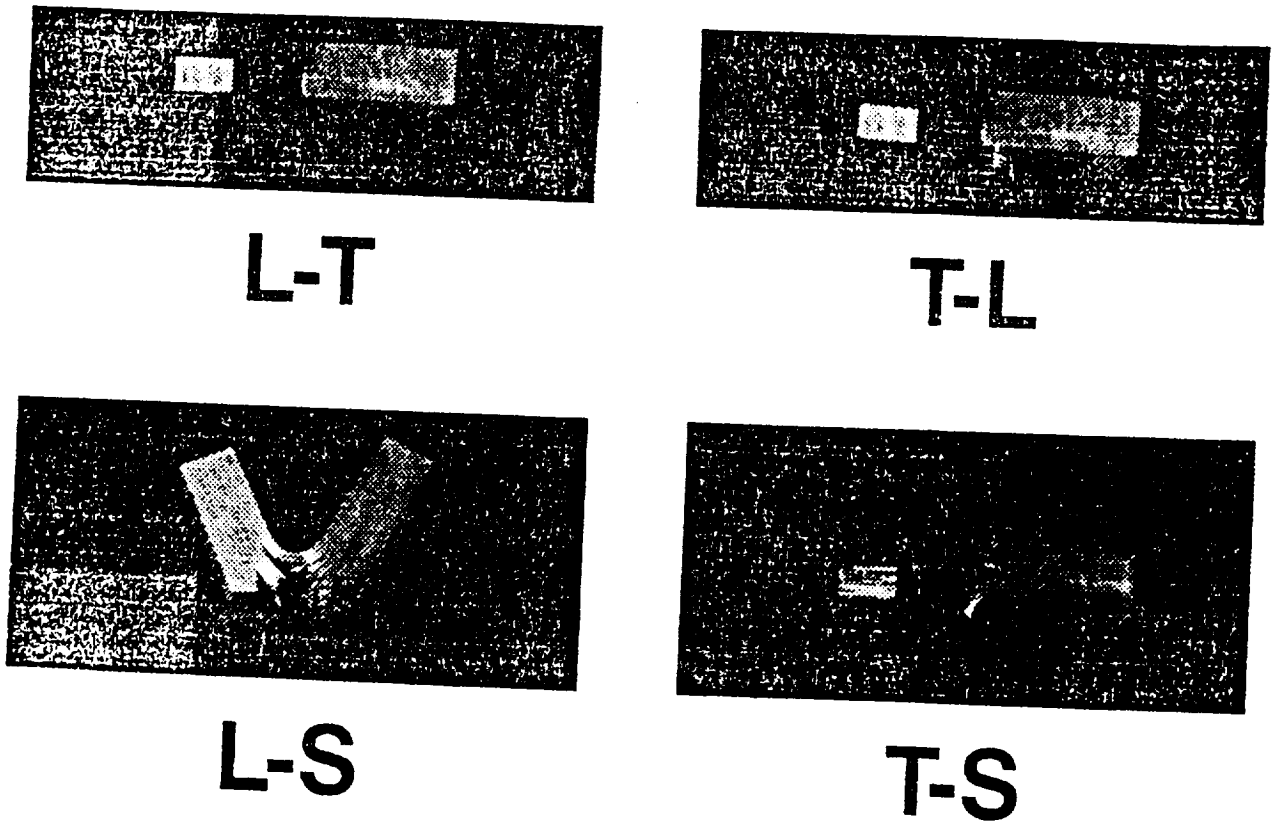

Figure 3: Fractured Charpy Bars - Peak Aged 2090 Al.

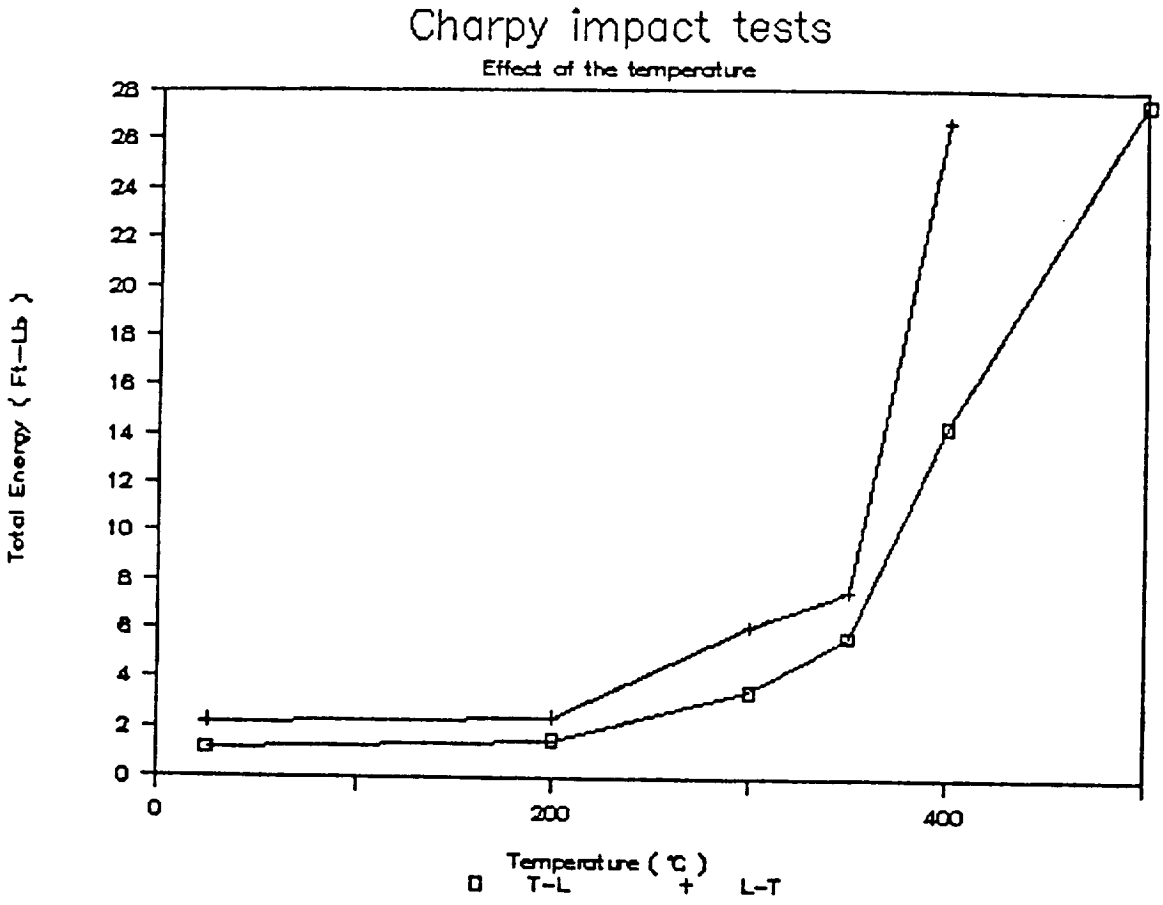

Figure 4: Effect of Temperature on Total Charpy Energy for Fracture of 2090 Al in T-C and L-T Orientation.

MICROHARDNESS VS TIME AND TEMPERATURE

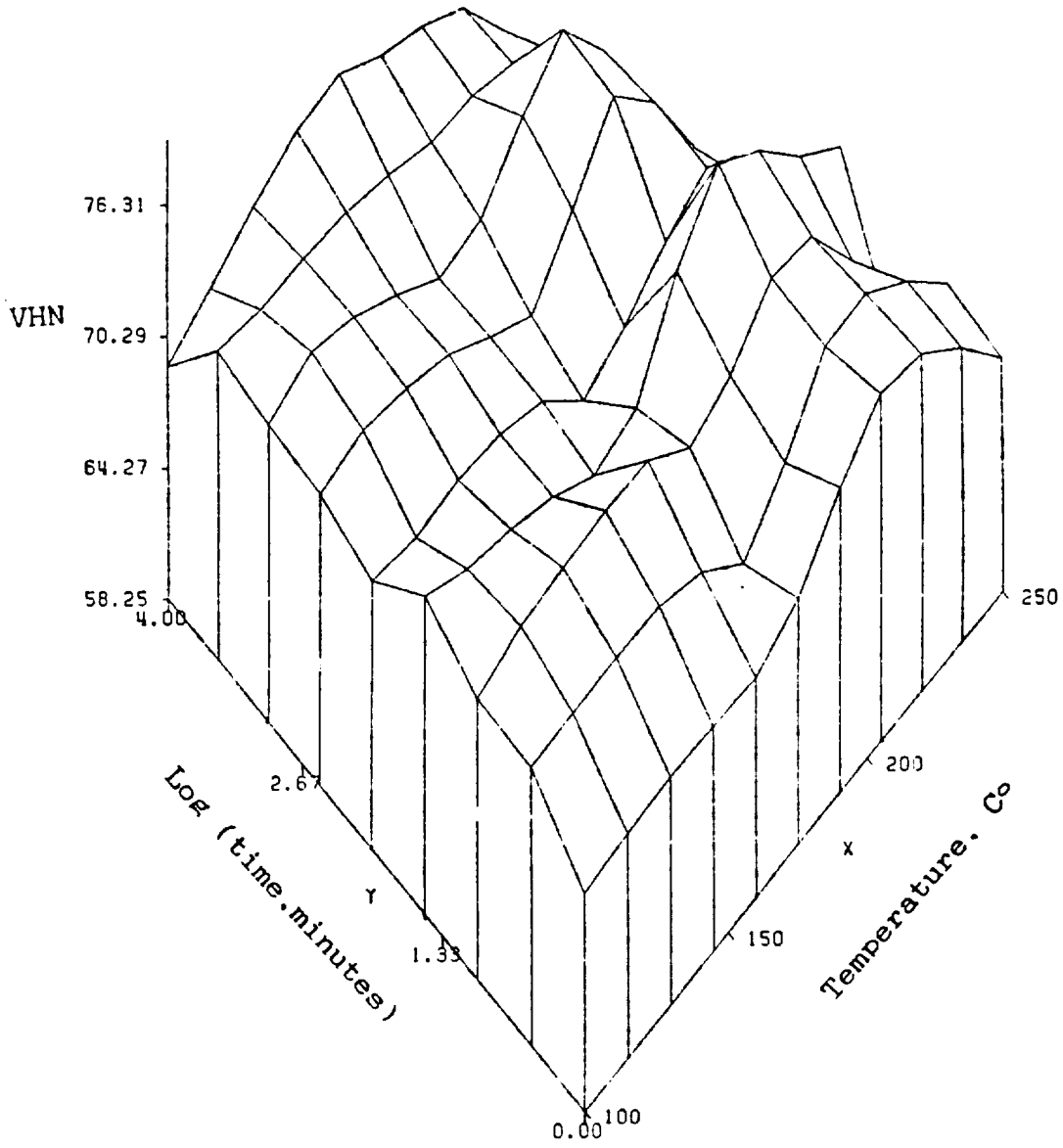

Figure 5: Aging Curve for 2219 Al Allov.

Program 7 **INVESTIGATION OF THE REACTION KINETICS BETWEEN SIC FIBERS AND SELECTIVELY ALLOYED TITANIUM MATRIX COMPOSITES AND DETERMINATION OF THEIR MECHANICAL PROPERTIES**

D.B. Gundel and F.E. Wawner

Objective

The objective of this study is to investigate fiber-matrix interactions in selected titanium reinforced composites and to define reaction kinetics and influence on mechanical properties of the composites.

Approach

The approach taken in this study is to fabricate titanium matrix composites using titanium that has been selectively alloyed to generate improved high temperature properties, and silicon carbide fibers as the reinforcement. The matrix alloy of immediate interest is a near-alpha alloy designated Ti-1100 which was recently developed. This alloy is a derivative of Ti-6242-Si and has the composition Ti-6Al-2.8Sn-4Zr-0.4Mo-0.45Si-0.07-0.02Fe. It offers improved creep, thermal stability and ductility over Ti-6242-Si. Ti-1100 will be obtained in the 8 mil sheet form for composite fabrication.

For comparison of reaction kinetics, samples will also be produced using the beta alloy Ti-15V-3Cr-3Sn-3Al. Recommendations will also be sought from LaRC technical personnel (W. Brewer) as to other matrices of most interest to NASA programs.

Silicon carbide fiber to be used as reinforcement can be obtained from two potential sources. Textron Specialty Materials in addition to its standard SCS-6 fiber is presently producing the fiber on a simplified reactor which should ultimately lead to a lower cost product than the conventional SCS type fibers. This fiber is available in 3 mil diameter (SCS-9) or 6 mil diameter (SCS-10). The fiber is chemically vapor deposited onto a carbon monofilament substrate (without a pyrolytic graphite layer that is used with standard SCS- fibers). These fibers have a surface layer, 3 microns thick, that is similar to the SCS-6 fiber. Tensile strengths for the fibers have been averaging 400-500 ksi in their early stage of development.

BP Corporation also produces a silicon carbide fiber designated Sigma fiber and is marketed by Atlantic Research Corporation in this country. This fiber is deposited on a tungsten substrate and does not have a carbon rich surface. Studies during the NASP program showed that a protective coating was necessary for the fiber to be effective. This fiber, if avail-

able, will be used for comparison with the Textron fiber and as a substrate for coating studies.

Part of this program will include a limited effort on the application and evaluation of diffusion barrier layers on SiC fibers for incorporation into Ti alloy composites. Major emphasis will be placed on ceramic coatings of borides or nitrides based on their large negative enthalpy of formation. However, certain metals or combinations thereof are also of interest. This project will be exploratory, but will be guided by theoretical considerations with regard to the selection of the coatings for minimum reactivity.

Kinetics of the Fiber/Matrix Reaction

The first part of this project is to determine the kinetics of SCS fiber/Ti matrix interactions at elevated temperatures. The growth of the reaction zone at the interface between matrix and fiber has been studied for several of these systems and has been shown to follow a parabolic growth law [1-4]

$$z = k(t^{1/2})$$

where z is the average reaction zone (RZ) thickness, t is the exposure time at a given temperature, and k is the temperature dependent reaction constant. The reaction constant, k, is the slope of a z versus $t^{1/2}$ plot at a certain temperature. Furthermore, the reaction can be described by an Arrhenius relation [1,3,4]:

$$\ln(k) = \ln(k_o) - Q/2RT$$

Here, k_o is the pre-exponential term, Q is the activation energy, R is the gas constant, and T is the absolute temperature. A plot of ln(k) versus 1/T using experimentally determined k values should be linear with a slope of -Q/2R.

Materials Acquired

The titanium alloy foils were obtained from Timet Corporation of Henderson, NV. The first foil from the supplier was 6 mils thick and was labelled Ti-1100. However, it was determined using EDX analysis that the chemistry of the foil was actually close to that of Ti-15-3. The manufacturer acknowledged that a mistake could have been made, but could not confirm that the material is Ti-15-3. The chemistry indicates that it is a beta-Ti alloy, so several experiments were done using this foil. In this report, the Ti alloy in this first foil will be referred to as foil-1. The second shipment contained foils that were 10 mils thick that were determined by EDX analysis to have chemistry close to the aim chemistry of Ti-1100.

The fibers were supplied by Textron Specialty Materials of Lowell, Mass. Fibers designated SCS-6, SCS-9, and SCS-10 were

received. The SCS-6 and SCS-10 fibers are 5.6 mils in diameter, whereas the SCS-9 fiber is 3.1 mils. The thickness of the protective layer on the SCS-10 and SCS-9 fibers is 3 microns, and 5 microns on the SCS-6.

Fabrication of Composites

Composites for the kinetic study were fabricated by diffusion bonding in a vacuum hot-press. The fabrication parameters (temperature, pressure, and time) were chosen to minimize the as-fabricated reaction zone thickness, but still insure complete consolidation. Layups of the fiber and foil were made by placing evenly spaced fibers over precleaned, one inch by one inch Ti-alloy foil and then applying a fugitive organic binder. Three such layups and a cover foil were then put into the vacuum hot-press. After a 60 millitorr or better vacuum was drawn, the temperature was slowly raised to 450°C and held for 2 hours to eliminate the binder, then raised again to the desired fabrication temperature. All of the composite samples were made with a pressure of 15 ksi for 30 minutes. The fabrication temperature for the composites was 850°C for the foil-1 matrix and 950-975°C for Ti-1100.

Kinetic Study

Each composite specimen prepared as described above was sectioned into several smaller samples. These smaller samples were all annealed at the same temperature, but for varying lengths of time. In order to prevent severe oxidation of the samples at the exposure temperatures, they were vacuum encapsulated in quartz tubes. The temperatures and times chosen for the study were 800°C, 900°C, and 1000°C for 5, 10, 25, 50, and 100 hours.

After the heat treatment, the samples were mounted in a cold cure resin with the fiber axis perpendicular to the plane of polish. The polishing was accomplished by using 180 grit SiC paper, followed by 30 and 6 micron metal-bonded diamond polishing wheels, and finally 1 micron alumina. To etch the polished samples, Kroll's etch (3% HF, 3% HNO_3, 94% H_2O) was swabbed on the foil-1 samples for 20 seconds , and the Ti-1100 samples for 10 seconds.

The samples were observed on a JEOL JSM-35 scanning electron microscope. Micrographs of the reaction zones of at least three different fibers per annealed sample were taken at a magnification suitable to make accurate measurements. Thirty or more measurements of the reaction zones of each sample were made and averaged using a LeMont Scientific Image Analysis System.

Results and Discussion

Composites were made consisting of foil-1/SCS-6, Ti-1100/SCS-6, and Ti-1100/SCS-9 with volume percent fiber of 15,

10, and 5, respectively. The low volume fraction of fiber in the Ti-1100 matrix results from the fact that the foil was relatively thick (10 mils). The as-fabricated reaction zone thicknesses were 0.42 microns for the Ti-1100 matrix, and 0.63 for the foil-1 matrix. Figure 1 shows the as-fabricated Ti-1100/SCS-6 composite.

SEM micrographs of the reaction zones of Ti-1100/SCS-6, Ti-6AL-4V/SCS-6 [1], and foil-1/SCS-6 composites that were annealed at 900°C for 25, 20, and 25 hours, respectively, are given in Figure 2. Note the relative sizes of the reaction zones (Ti-1100 is the smallest). Note also the uniformity of Ti-1100 RZ as compared to the other two. Rhodes and Spurling [5] have attributed the nonuniformity of the RZ in the Ti-6-4 to the fact that this is an alpha + beta alloy and the reaction progresses faster in the beta phase than in the alpha phase. According to them, the reason for this is that carbon (one of the main reacting species) has a higher diffusivity and lower solubility in beta-Ti. This might suggest that, with other effects being equal (such as the slow down of RZ growth with alloying additions to Ti as was noted by Martineau et. al. [3]), for a given temperature, the reaction will progress more rapidly in a Ti alloy that has more beta phase. This may be an important consideration in choosing a matrix to limit the rate of reaction in Ti alloy/SiC composites.

Thus far the kinetic parameters for the two Ti-1100 systems indicated above have been determined. RZ thickness versus $t^{1/2}$ for the SCS-9 fiber is plotted in Figure 3 (the Arrhenius plot is also given). The data obtained from the SCS-6 composite is virtually identical to that of the SCS-9 material, therefore this serves as a plot for Ti-1100/SCS-6 as well. The only real difference in the data between the two was at 1000°C for 100 hours where the surface layer on the SCS-9 fiber had been consumed by the reaction and that of the SCS-6 had not. The RZ thickness for the SCS-9 fiber was 9.11 microns and 8.35 microns for the SCS-6 fiber. The experimentally determined kinetic parameters for Ti1100/SCS-9,6 are given in Table 1. Also given are values determined by researchers studying the Ti-6-4/SCS-6 system. Figure 4 is a plot comparing data obtained in this study for the Ti-1100/SCS-9 to that obtained by Whatley (1) for a single coated SCS-6 fiber (35 volume %) in a Ti-6-4 matrix. It is evident that the Ti-1100 matrix reacts more slowly under these conditions than does the Ti-6-4.

Some problems were encountered in determining the kinetic parameters of the foil-1/SCS-6 system. At the 900°C and 1000°C exposure temperatures, large particles (up to 30 microns) were present in roughly a circular region around the fibers (see Fig. 5b). This was not seen in the Ti-1100 matrix composites (Fig. 5c). Backscattered electron imaging, which shows differences in compositions of areas, indicated that these particles had the same average atomic weight as the reaction zones. It has been determined by many workers that TiC is the major reaction product

in Ti alloy/SCS fiber composites [3-5,7,8]. If these particles surrounding the fibers are TiC, then they are probably due to the fact that foil-1 is a beta-Ti alloy which allows for faster carbon diffusion (i.e. extracting carbon from the SCS layer) into the matrix and, because of the low solubility of carbon in the beta phase, formation of isolated carbide phases after thermal exposure. Diffusion of carbon in the matrix has been noticed by Pailler et. al. in Ti-6-4 composites during long annealing times. Other evidence that suggests that these particles result from carbon diffusion from the SCS surface is that the RZ thickness when the surface layer of the fiber is completely consumed is about 10 microns for both Ti-1100 (from extrapolation) and Ti-6-4 [1], and only 6.4 microns for foil-1 (1000^{o}, 25 hr). In other words, even though the same amount of fiber has been consumed, the reaction zone at the interface in the foil-1 is smaller. If these particles indeed result from a depletion of carbon in the surface layer, and subsequent diffusion into the matrix to form TiC, then the reaction kinetics cannot be determined by simply measuring the RZ thickness, so other methods must be devised.

At the higher temperatures and longer annealing times, the Ti-1100/SCS fiber RZ appeared to have a four layer structure (see Fig. 6). Regions A and B are what remains of the carbon rich surface coating, C through F are reaction zone layers, and E is a matrix silicide. EDX analysis of the four reaction layers indicates that C, E, and F are silicon rich zones. Using TEM studies, Rhodes and Spurling [4] have seen a silicon rich zone adjacent to the fiber in as-fabricated Ti-6-4 composites. They also saw a silicon rich zone adjacent to the matrix, and identified the region in between these two layers as TiC. Different researchers have seen Si-rich zones next to the matrix in other systems [3-8].

Future Work

1. TEM studies of as-fabricated and heat treated samples of Ti-1100 composites to determine the nature of the reaction.

2. Continue comparisons of Ti-1100 kinetics to other matrices.

3. Evaluate the mechanical properties of annealed Ti-1100 samples and determine the effect of the reaction zone on them.

REFERENCES

1. Whatley, W.J., Ph.D. Dissertation, University of Virginia, (1985).

2. Metcalfe, A.G., "Fiber Reinforced Titanium Alloys," in Composite Materials Vol. 4 Metallic Matrix Composites K.G. Kreider eds. Academic Press, New York (1974).

3. Martineau,P., Pailler,R., Lahaye, M., Naslain, R., "SiC Filament/Titanium Composites Regarded as Model Composites II," J. Mat. Sci., Vol. 19, pp. 2749-2770 (1984).

4. Pailler, R., Martineau, P., Lahaye, M., Le Petitcorps, Y., Naslain, R., "Influence of Diffusion Formed Brittle Layers at Filament-Matrix Interfaces on the Mechanical Properties of SiC/Ti Composite Materials," in Reactivity of Solids Part B, Ed. Pierre Barret, Louis-Claude Dufour, Elsevier, New York (1985).

5. Rhodes, C.G., Spurling, R.A., "Fiber-Matrix Reaction Zone Growth Kinetics in SiC-Reinforced Ti-6Al-4V as Studied by Transmission Electron Microscopy," Recent Advances in Composites in the United States and Japan, Eds. J.R. Vinson, M. Taya, ASTM, Philadelphia, pp. 585-599 (1985).

6. Lerch, B.A., Hull, D.R., Leonhardt, T.A., "As-Received Microstructure of a SiC/Ti-15-3 Composite," NASA Technical Memorandum 100938, August (1988).

7. Dudek, H.J., Leucht, R., Ziegler, G., "Auger Electron Spectroscopy of the Interface of SiC Fiber Reinforced Titanium Alloys," Titanium: Science and Technology Vol. 3, Proc. 5th Int'l Conf. on Titanium, Munich, Eds. G. Lutjering, U. Zwicker, W. Bunk, (1985).

8. Jones, C., Kiely, C.J., Wang, S.S., "The Characterization of an SCS6/Ti-6Al-4V MMC Interphase," J. Mat. Res., Vol. 4, No. 2, Mar/Apr (1989).

	k (10^6 cm/$s^{1/2}$)		
^oC	Ti1100/SCS-6,9	Ti6-4/SCS-6 (1)	Ti6-4/SCS-6 (4)
800	0.11	0.16	
850		0.95	0.8
900	0.50	0.84	
950		2.0	1.8
1000	1.43	3.1	
1050			4.4
k_o (cm/$s^{1/2}$)	1.21	4.6	0.06
Q (kcal/mol)	68.8	71.4	49.6

Table 1 - Kinetic Parameters for some Ti/SiC fiber systems

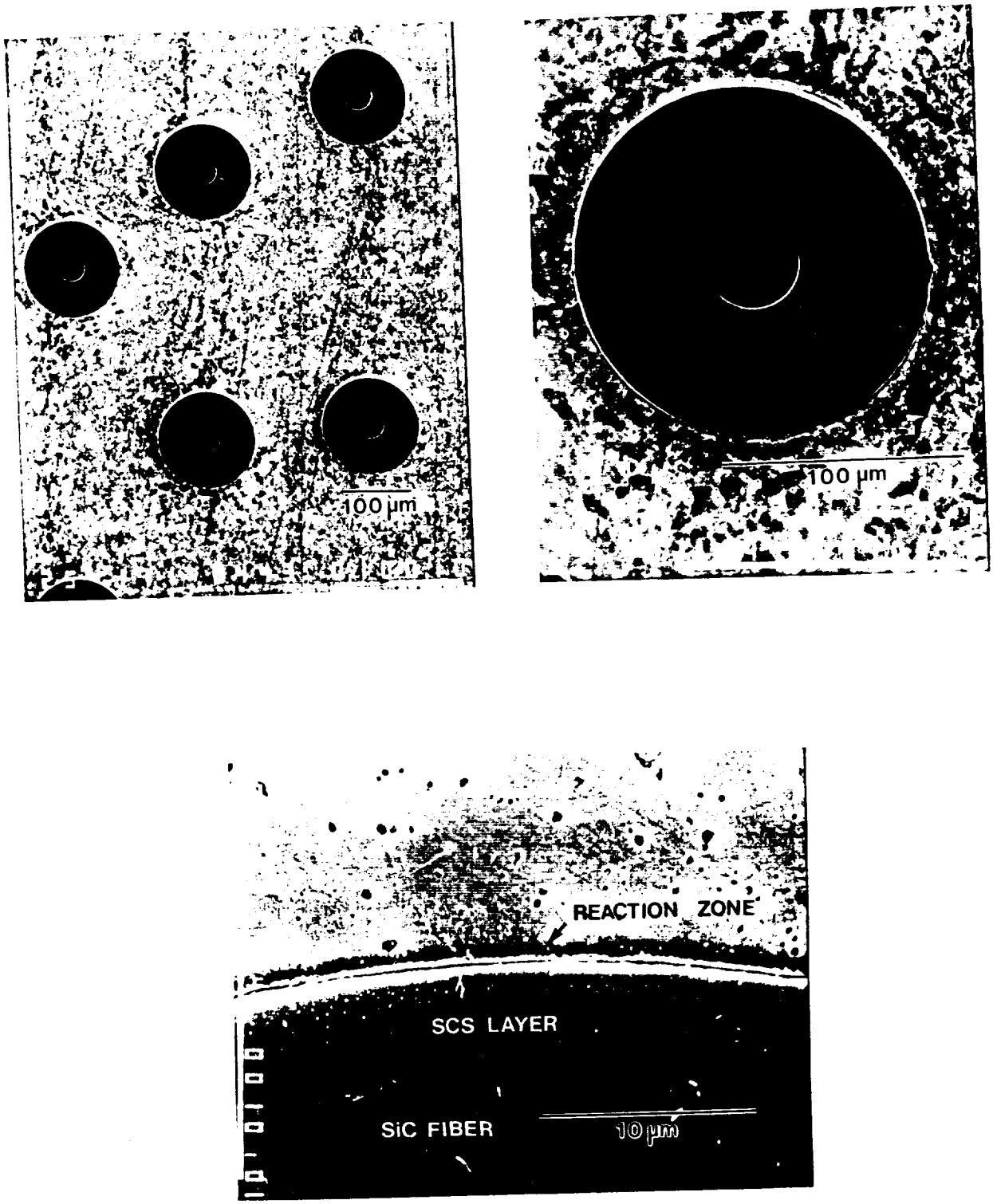

Figure 1- As-fabricated Ti-1100/SCS-6 composite

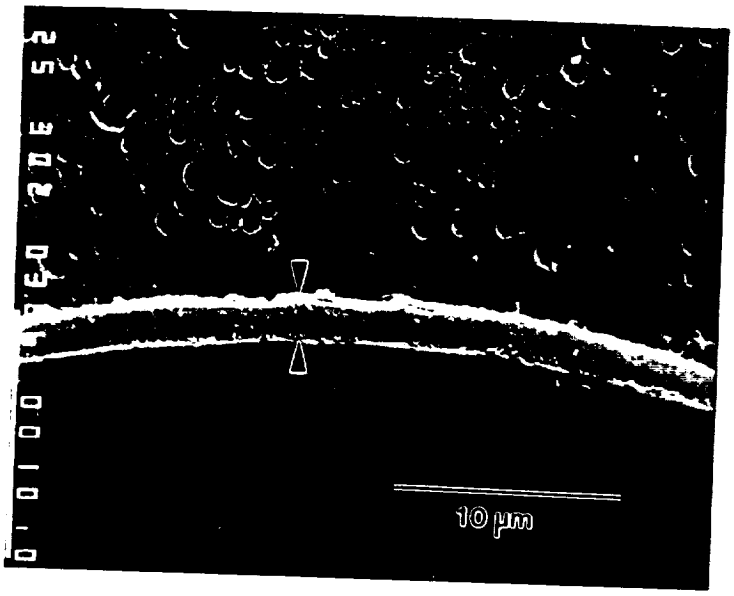

a) Ti-1100 - 900°C, 25 hours

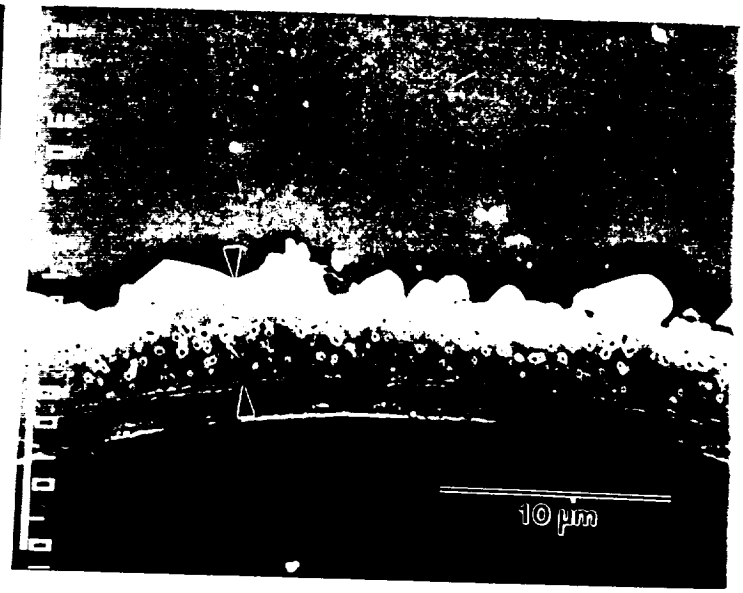

b) Foil-1 - 900°C, 25 hours

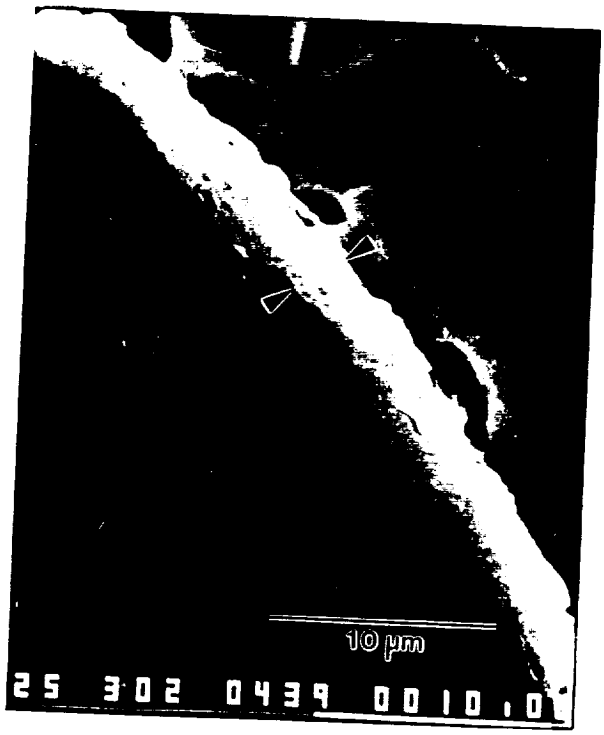

c) Ti-6-4 - 900°C, 20 hours
(from Whatley (1))

Figure 2- Reaction zones of annealed SCS-6 composites

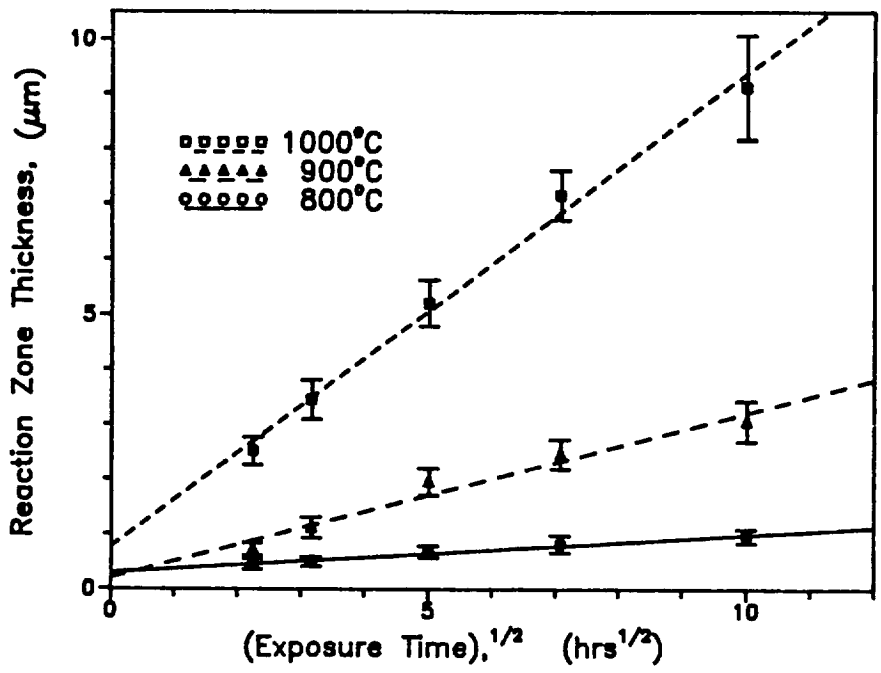

a)

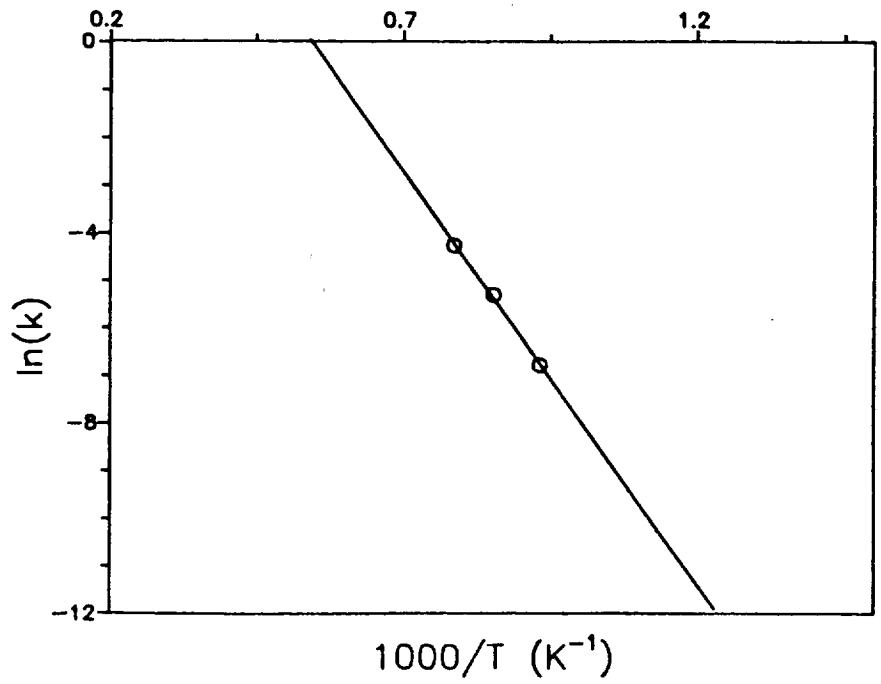

b)

Figure 3 - a) Parabolic reaction kinetics of Ti-1100/SCS-6,9

b) Arrhenius plot

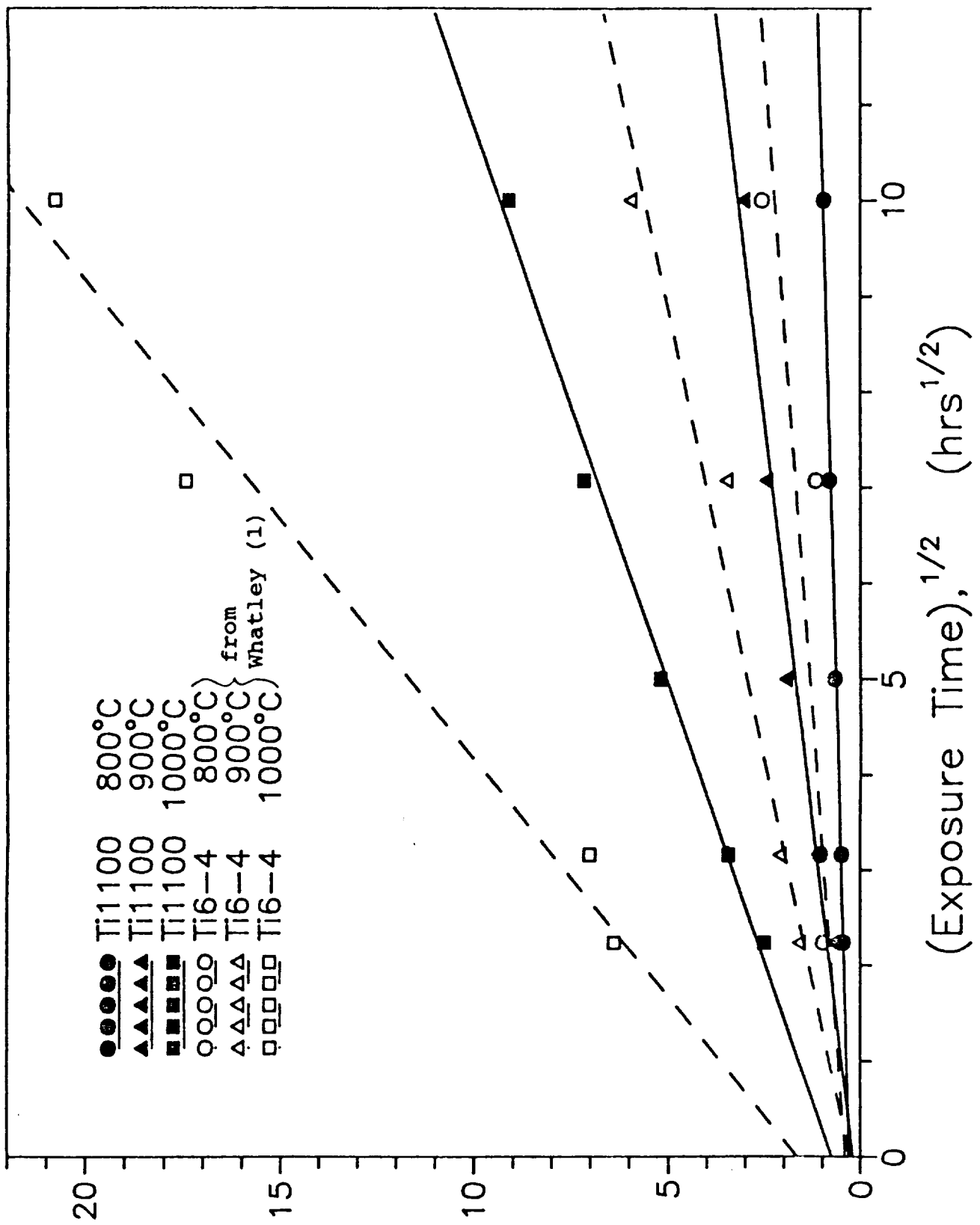

Figure 4 - Ti-1100 matrix vs. Ti-6-4

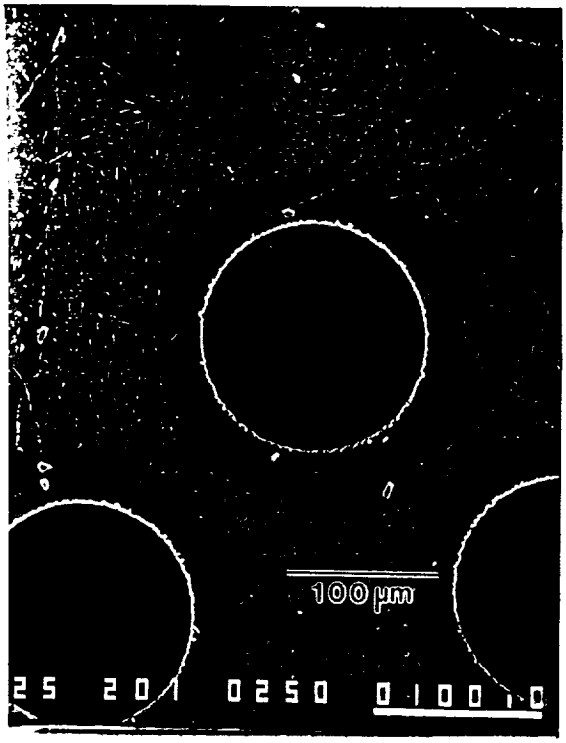

a) Foil-1, 900°C, 10 hours

b) Foil-1, 1000°C, 50 hours

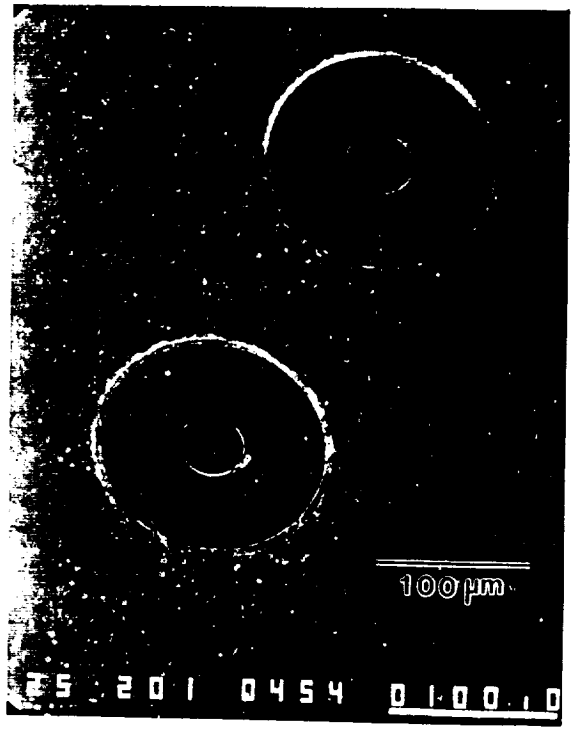

c) Ti-1100, 1000°C, 50 hours

Figure 5 - Annealed SCS-6 composite samples

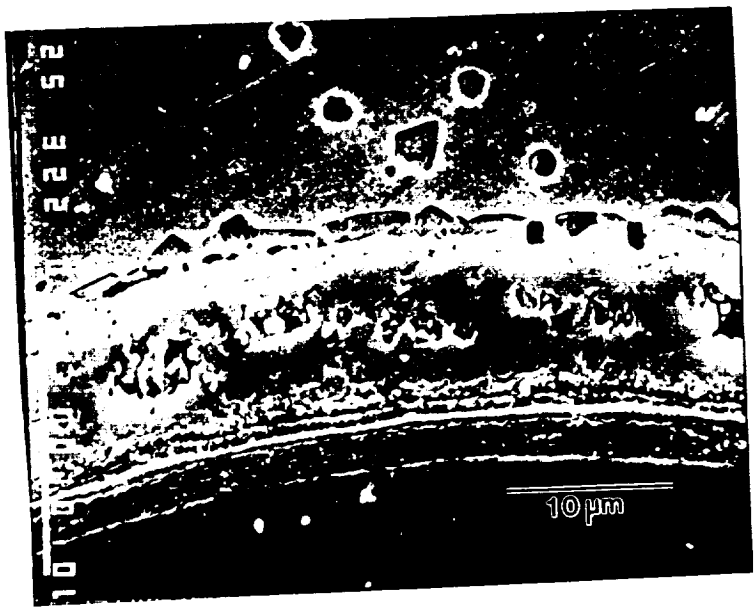

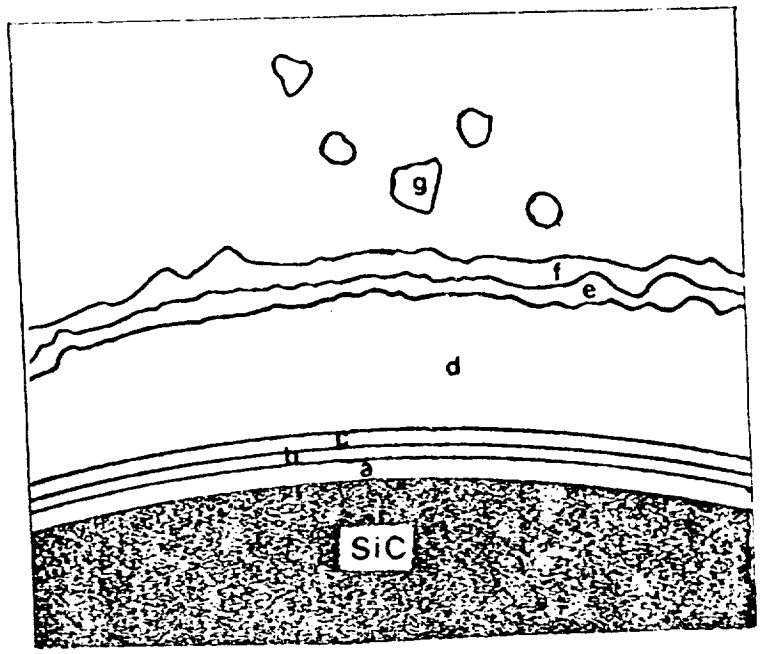

a ,b - remainder of SCS layer

c,e,f - silicon rich layers

d - TiC

g - matrix silicide

Figure 6- Ti-1100/SCS-6 interface after 100 hours at 1000°C

Program 8 **THE EFFECT OF NON-RANDOM PARTICLE DISTRIBUTION ON THE MECHANICAL BEHAVIOR OF STRUCTURAL MATERIALS**

Joseph B. Parse and John A. Wert

Project Objective

The objective of this project is to develop methods for quantitative analysis of the spatial distribution of second phases in structural materials. Coupling of these methods with models for deformation and fracture will reveal the effects of non-random phase distribution on material performance.

Nearly all structural materials contain more than one phase. Often, the second-phase particles (or fibers) are dispersed in a nonrandom fashion; they may be either regularly-spaced or clustered into clumps or bands. Examples of advanced aerospace materials which contain nonrandom phase dispersions include alloys fabricated by powder metallurgy methods, composite materials and superalloys. The effects of clustering or regular spacing of second phase particles on deformation and fracture of the materials are poorly understood. The problem of analyzing and understanding the effects of nonrandom particle dispersions on macroscopic material properties can be divided into two parts: i) characterizing the spatial distribution of the second phase particles, and ii) assessing the effect of non-random particle dispersions on deformation and fracture behavior.

The solution to the overall problem will necessarily be an interdisciplinary effort involving both material and mechanical sciences. The initial UVa effort is focusing on development of methods for characterizing the spatial distribution of second phases in structural materials since this part of the overall problem is least well-developed.

Progress During the Current Reporting Period

We seek to establish a method for analyzing the spatial distribution of particles in materials that will tell us whether particles are clustered, randomly distributed or anticlustered (regularly-spaced); and whether the particle dispersion is directional (banding). The analysis should yield parameters which characterize the degree and scale of clustering and, if the particle dispersion is banded, the direction of banding. For the purpose of this analysis, the problem is simplified by reducing each particle to a point located at the particle's center of mass.

For a two-dimensional particle dispersion, the Voronoi polygon corresponding to a particular particle is the smallest convex polygon that can be formed by the perpendicular bisectors of lines joining the chosen particle with all other particles in

the dispersion [1-3]. The adjacent particles which define the Voronoi polygon for a particular particle are near-neighbor particles. Once the Voronoi polygon has been determined for each particle, the polygons can be assembled into an area-filling tessellation: the Dirichlet or Primary tessellation [4,5]. A second tessellation - the set of Deaunay triangles - may be constructed using the lines joining near neighbor pairs; this procedure yields the Dual tessellation.

Our broad approach to the problem of characterizing the spatial distribution of second phases in structural materials involves the following steps.

- Use computer digitizing methods to describe the particle dispersion as a two-dimensional array of points.
- Construct the Voronoi polygon for each particle in the two-dimensional particle dispersion.
- Construct the Primary and Dual tessellations from the polygons.
- Establish statistical methods to deduce the particle distribution characteristics (degree and scale of clustering, banding) from distributions of the Voronoi polygon, Primary tessellation and Dual tessellation properties.
- Couple the statistical analysis methods for particle dispersions to micromechanical models for deformation and fracture of materials.

The long term result of this research project will enable the effects of nonrandom particle dispersions on bulk mechanical properties to be understood and predicted.

During the first 6 month reporting period of this project, computer software has been developed to carry out the first three steps listed above. The initial particle dispersions can be either real dispersions obtained by digitizing micrographs or computer-generated dispersions which have known types of clustering or banding. The particle positions are then used to construct the Voronoi polygon for each particle, and the Primary and Dual tessellations for the particle dispersion. The software which constructs the Voronoi polygons and the Primary and Dual tessellations can accept dispersions containing up to 1000 particles. Particle dispersions obtained by digitizing real micrographs usually do not contain more than a few hundred particles so the software developed thus far is directly applicable to analyzing real cases.

In addition to developing software for generating the Voronoi polygons and the Primary and Dual tessellations for particle dispersions, we are in the process of developing additional software that will enable us to apply statistical analysis meth-

ods to these geometrical constructs. This has already been accomplished for the Voronoi polygon case and current efforts are focusing on the Dual tessellation case.

Typical results for several computer-generated particle dispersions are shown in Figures 1 through 3. Part a) of each figure displays the particle dispersion with the primary tessellation superposed. The severity of clustering of the particles increases from Figure 1 to Figure 3. Part b) of each figure is a graph showing the cumulative distribution of Voronoi polygon areas. The distribution of Voronoi polygons area is seen to depend markedly on the severity of clustering. In addition to the distribution of polygon areas, a variety of other properties have been examined. These include equivalent circle diameter, length of the longest chord, orientation of the longest chord, deviation of the particle from the polygon center of mass, normalized perimeter length, and others.

Future Plans

During the next reporting period, attention will be focused on three areas of the overall problem:

1. Application of statistical analysis methods to the Voronoi polygon property distributions. The objective of this effort is to develop methods to extract parameters which characterize the original particle dispersion from these Voronoi property distributions. The starting point for this analysis is apparent from the graphs of Voronoi polygon area shown in Figures 1 - 3. It is clear that severe clustering causes the cumulative distribution to separate into two overlapping distributions, one associated with intra-cluster polygons and the other associated with inter-cluster polygons. Statistical analysis methods which can deconvolute the superposed distributions should enable us to separate the 2 classes of Voronoi polygons for analysis.

2. Development of similar methods for analyzing the Dual tessellation, which includes additional information not available from the individual Voronoi polygons.

3. Application of the analysis methods to real materials. At present, analyses are planned for several types of composite materials, including cast Al-SiC particulate composites and extruded Zn-Al-SiC composite materials. These materials were selected for initial analysis because samples are available for which we know the processing histories and one of the long term goals of the project is to correlate the particle dispersion characteristics with processing conditions.

References

1. D. Weaire and N. Rivier, Contemporary Physics, 25 (1984) 59-99.

2. W. Browstow, J.-P. Dussault and B.L. Fox, J. Computational Physics, 29 (1978) 81-92.

3. I.K. Crain, Computers and Geoscience, 4 (1978) 131-141.

4. A. Bowyer, The Computer Journal, 24 (1981) 162-166.

5. D.F. Watson, The Computer Journal 24 (1981) 167-172.

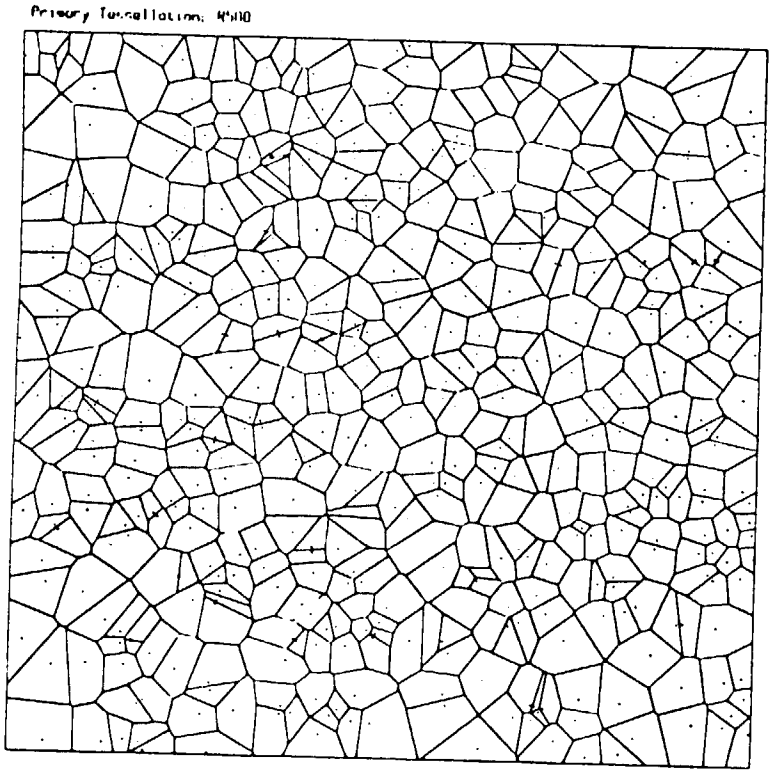

(a)

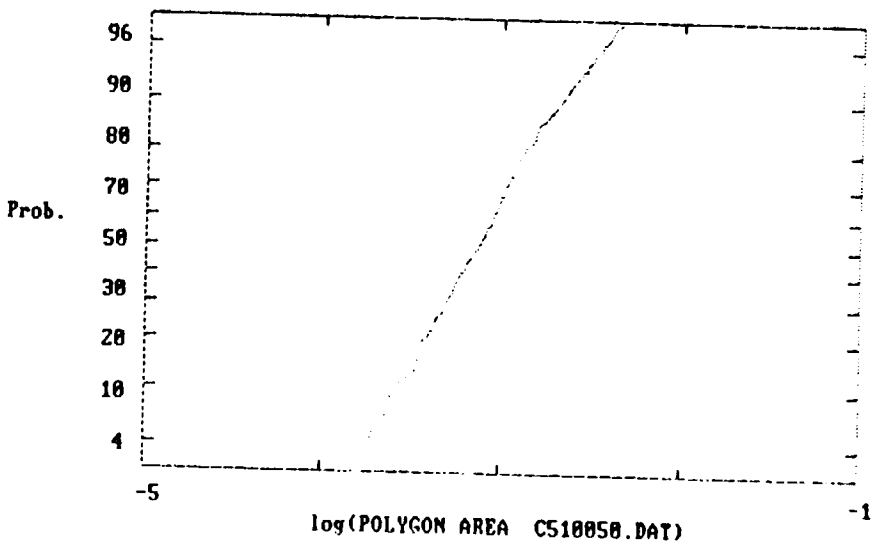

(b)

Figure 1. a) Particle distribution and superposed Primary tessellation for a computer-generated, random particle dispersion. b) Cumulative distribution plot for Voronoi polygon area.

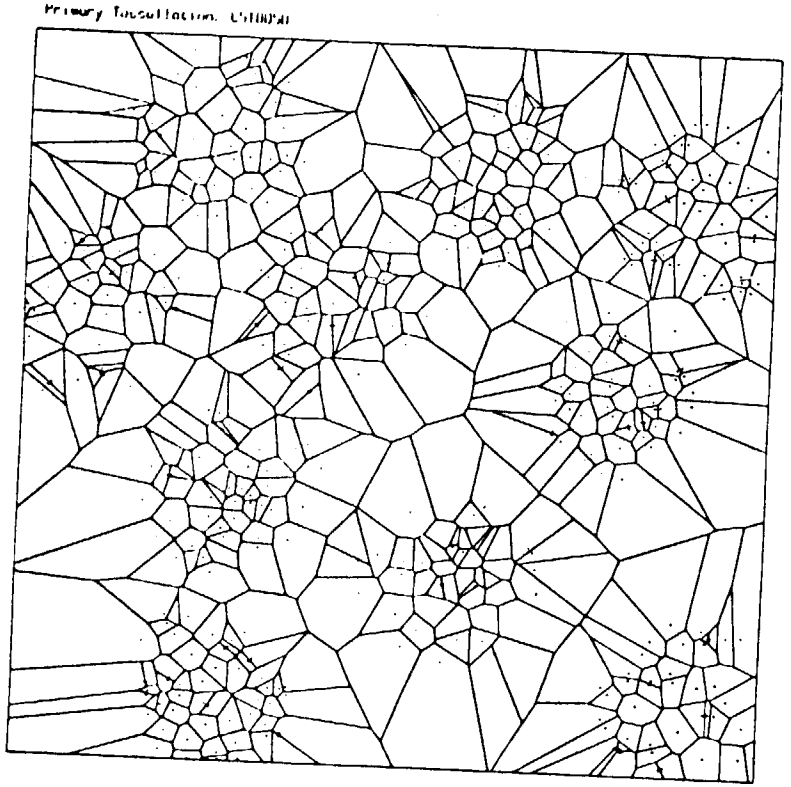

(a)

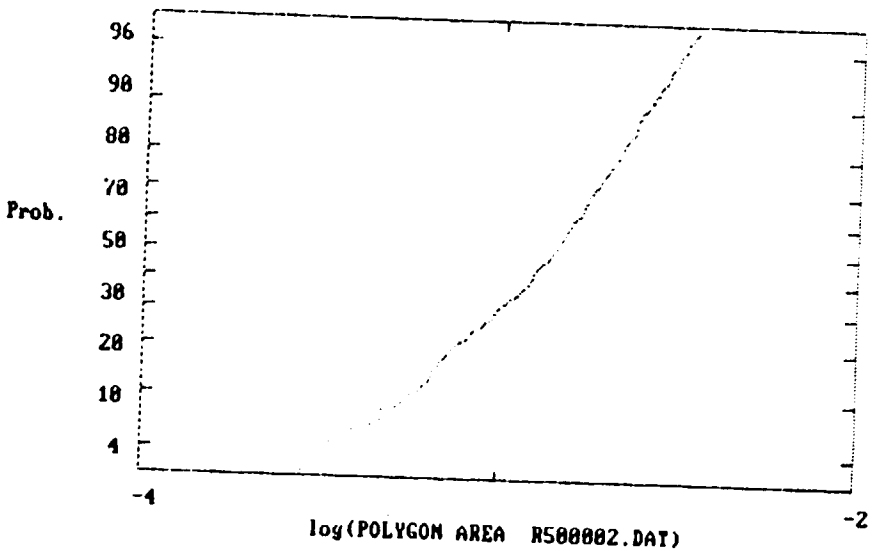

(b)

Figure 2. a) Particle distribution and superposed Primary tessellation for a computer-generated, moderately-clustered particle dispersion (cluster spacing is 2 times the cluster diameter). b) Cumulative distribution plot for Voronoi polygon area.

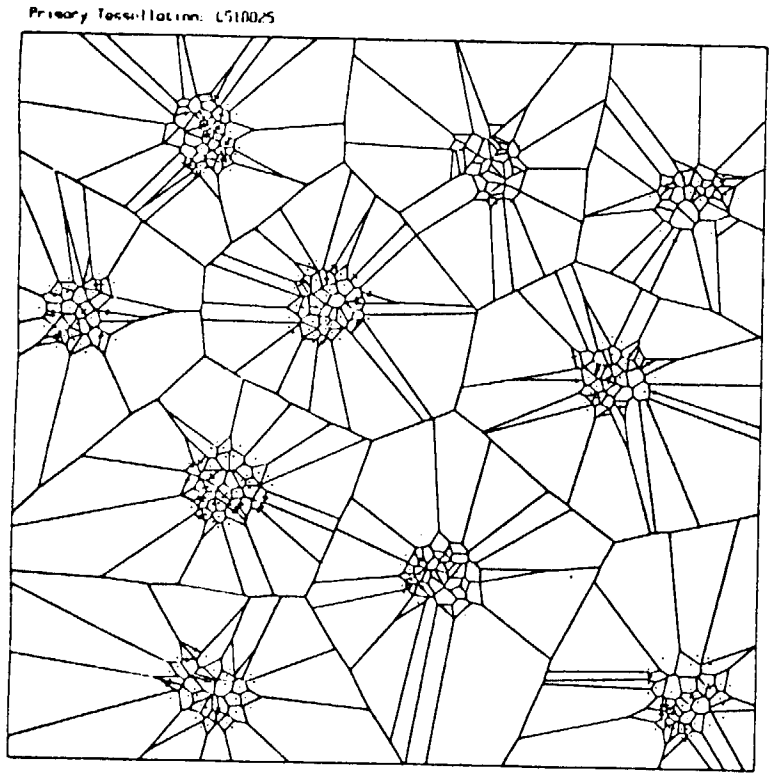

(a)

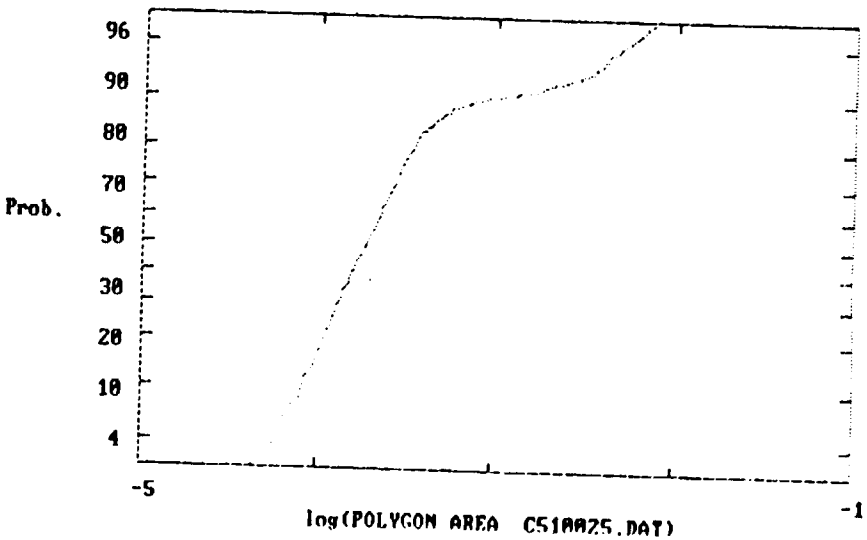

(b)

Figure 3. a) Particle distribution and superposed Primary tessellation for a computer-generated, strongly-clustered particle dispersion (cluster spacing is 4 times the cluster diameter. b) Cumulative distribution plot for Voronoi polygon area.

APPENDIX I: GRANT PUBLICATIONS

1. R. P. Gangloff, "Corrosion Fatigue Crack Propagation in Metals", in Environment Induced Cracking of Metals, R. P. Gangloff and M. B. Ives, eds., NACE, Houston, TX, in press (1989).

2. K. T. Venkateswara Rao, R. S. Piascik, R. P. Gangloff and R. O. Ritchie, "Fatigue Crack Propagation in Aluminum-Lithium Alloys", in Al-Li,V, E. A. Starke, Jr. and T. H. Sanders, eds., EMAS, Wardley Heath, UK, in press (1989).

3. J. A. Wagner, "Age Hardening Characteristics and Mechanical Behavior of Al-Cu-Li-Zr-In Alloys", TMS Pub., E. W. Lee, E. H. Chia, and N. J. Kim, eds., TMS-AIME, Warrendale, PA, in press (1989).

4. R. G. Buchheit and G. E. Stoner, "The Corrosion Behavior of the T_1 (Al_2cuLi) Intermetallic Compound in Aqueous Environments", in Al-Li,V, E. A. Starke, Jr. and T. H. Sanders, eds., EMAS, Wardley Heath, UK, in press (1989).

5. J. P. Moran and G. E. Stoner, "Solution Chemistry Effects on the Stress Corrosion Cracking Behavior of Alloy 2090 (Al-Li-Cu) and Alloy 2024 (Al-Cu-Mg)", in Al-Li,V, E. A. Starke, Jr. and T. H. Sanders, eds., EMAS, Wardley Heath, UK, in press (1989).

6. F. C. Rivet and R. E. Swanson, "Influence of Dissolved Hydrogen on Aluminum-Lithium Alloy Fracture Behavior", in Al-Li,V, E. A. Starke, Jr. and T. H. Sanders, eds., EMAS, Wardley Heath, UK, in press (1989).

APPENDIX II: GRANT PRESENTATIONS

1. R. S. Piascik and R. P. Gangloff, "Intrinsic Corrosion Fatigue Crack Propagation in Al-Li-Cu Alloys, presented at the International Conference on Fracture -- VII, Houston, TX, March, 1989.

2. R. S. Piascik, R. P. Gangloff, and R. O. Ritchie, "Fatigue Crack Propagation in Al-Li Alloys", presented at the Fifth International Al-Li Conference, Williamsburg, VA, March, 1989

3. R. P. Gangloff, "Measurement and Modeling of Hydrogen Environment Embrittlement: Continuum Perspective", presented at Corrosion '89 NACE, New Orleans, LA, April, 1989.

4. John A. Wagner, "Age Hardening Characteristics in Mechanical Behavior of Al-Cu-Li-Zr-In Alloys", presented at the TMS-Annual Meeting, Las Vegas, NV, February, 1989.

5. R. G. Buchheit and G. E. Stoner, "The Corrosion Behavior of the T_1 (Al_2CuLi) Intermetallic Compound in Aqueous Environments", presented at the Virginia Academy of Sciences meeting, Virginia Commonwealth University, Richmond, VA, May 26, 1989.

6. J. P. Moran and G. E. Stoner, "Solution Chemistry Effects on the Stress Corrosion Cracking Behavior of Alloy 2090 and Alloy 2024", presented at The 5th International Conference on Al-Li Alloys, Williamsburg, VA, March, 1989.

7. F. C. Rivet, "Damage of Al-Li Alloys Due to the Environment", presented at the 67th Annual Meeting of the Virginia Academy of Science, Virginia Commonwealth University, Richmond, VA, May, 1989.

8. F. C. Rivet and R. E. Swanson, "Influence of Dissolved Hydrogen on Al-Li Fracture Behavior", presented at the Fifth International Aluminum-Lithium Conference, Williamsburg, VA, March, 1989.

In: Environment Induced Cracking of Metals, R.P. Gangloff and M.B. Ives, eds., NACE, Houston, TX, in press (1989).

CORROSION FATIGUE CRACK PROPAGATION IN METALS

Richard P. Gangloff

Department of Materials Science
University of Virginia
Charlottesville, VA 22901
USA

I. ABSTRACT: CONCLUSIONS OF THE REVIEW

The objective of this paper is to critically compile and assess experimental results and mechanistic models for corrosion fatigue crack propagation in structural alloys exposed to ambient temperature gases and electrolytes. Only crack propagation is considered. Data and models are based on continuum fracture mechanics descriptions of crack tip stress and strain fields, coupled with continuum modeling of occluded crack mass transport and chemical reactions. The aim is to develop the state-of-the-art so as to inform the person seeking to broadly understand environmental effects on fatigue, to provide an ample experimental basis for evaluations of mechanistic models relevant to specialists, and to define worthwhile directions for future corrosion fatigue characterizations and mechanistic research.

Section II provides an introduction to corrosion fatigue. The state-of-the-art which emanated from the Storrs and Firminy conferences is summarized. Qualitative mechanisms for corrosion fatigue are presented.

Section III assesses the fracture mechanics approach to corrosion fatigue, while Section IV considers experimental methods. The following two conclusions are established:

1. Fracture mechanics descriptions of corrosion fatigue crack propagation; viz, growth rate as a function of stress intensity factor; provide an established and physically meaningful basis which couples alloy performance, damage mechanisms and life prediction studies through the concept of growth rate similitude. Extensive data bases have been developed for structural alloys over the past three decades. (See Section III.)

2. Experimental methods are developed for determinations of average crack growth rate as a function of continuum fracture mechanics crack tip parameters, particularly DK. Non-steady state crack growth, unique to corrosion fatigue, and crack closure are not sufficiently considered. Future procedures will incorporate precision crack length measurement and computer control of stress intensity to develop quantitative and novel corrosion fatigue crack growth rate data, particularly near threshold. Advances have been recorded in measurements of small crack growth kinetics, however, such approaches are not easily adapted to controlled environments. The fundamental problem is the lack of methods to directly probe the mechanical and chemical damage processes local to the corrosion fatigue crack tip. (See Section IV.)

Section V provides examples of important variables which affect corrosion fatigue crack growth rate behavior. It is concluded that:

3. A plethora of interactive variables influences the corrosion fatigue crack growth rate-stress intensity relationship. The effects of chemical, metallurgical and mechanical variables are well characterized and reasonably explained by qualitative arguments. Time, or loading frequency, is critical; complicating long-life component performance predictions based on shorter term laboratory data. Corrosion fatigue crack growth rates are affected by environment chemistry variables (viz: temperature; gas pressure and impurity content; electrolyte pH, potential, conductivity, and halogen or sulfide ion content); by mechanical variables such as DK, mean stress, waveform and overloads; and by metallurgical variables including impurity composition, microstructure and cyclic deformation mode. Limited studies show that yield strength is not a critical variable in cycle-time dependent corrosion fatigue. Fractographic analyses of microscopic crack paths provide a basis for failure analyses and input to mechanistic studies. (See Section V.)

deformation is time or environment sensitive. These limitations do not preclude the only quantitative approach developed to date to characterize subcritical crack propagation. Rather, they indicate the need for crack tip microchemical-mechanical modeling. (See Section VII.)

Section VIII provides necessary directions for future research in corrosion fatigue.

6. Opportunities exist for research on corrosion fatigue to: (a) broaden phenomenological understanding, particularly near threshold, (b) develop integrated and quantitative microchemical-mechanics models, (c) develop experimental methods to probe crack tip damage, and to measure near threshold time-cycle dependent crack growth, (d) characterize the behavior of advanced monolithic and composite alloys, and (e) develop damage tolerant life prediction methods and in situ sensors for environment chemistry and crack growth. (See Section VIII.)

A Table of Contents is provided in Appendix 1.

IX. ACKNOWLEDGEMENTS

Financial support for the preparation of this review and for research on corrosion fatigue in steels and aluminum alloys was provided by the NASA-Langley Research Center under Grant NAG-1-745 with D.L. Dicus as monitor, by the Newport News Shipbuilding and Drydock Company under Grant POM-7671-R with G.M. Cobb as monitor, and by the Virginia Center for Innovative Technology under Grant CIT-TDC-88-01 with K. Blurton as monitor through the University of Virginia Center for Electrochemical Sciences and Engineering. This support is gratefully acknowledged.

APPENDIX 1: TABLE OF CONTENTS

VIII.2.b. Experimental Methods

VIII.2.c. Fracture Mechanics Similitude

VIII.2.d. Micromechanical-Chemical Mechanism Modeling

VIII.2.e. Life Prediction

FATIGUE CRACK PROPAGATION IN ALUMINUM-LITHIUM ALLOYS

K.T. Venkateswara Rao*, R.S. Piascik+, R.P. Gangloff+ and R.O. Ritchie*

The oft-quoted outstanding fatigue crack propagation resistance of aluminum-lithium alloys is controlled by extrinsic mechanical crack tip shielding processes, and by chemical environment effects. Prominent microstructural influences are interpreted within these frameworks. Extensive data describe the growth kinetics of fatigue cracks in ingot metallurgy Al-Li alloys 2090, 2091, 8090, 8091 and in powder metallurgy alloys exposed to moist air. Crack growth is dominated by shielding from tortuous crack paths and resultant asperity wedging. Beneficial shielding is minimized for small cracks, for high stress ratios and for certain loading spectra. While water vapor and aqueous chloride environments enhance crack propagation, Al-Li-Cu alloys behave similarly to 2000 series aluminum alloys, being more resistant to corrosion fatigue than 7000 alloys. Loading frequency, ΔK, water vapor pressure and electrode potential are the critical variables. Cracking in water vapor is controlled by hydrogen embrittlement, with little influence of surface films on cyclic plasticity; mechanisms for corrosion fatigue in aqueous environments are unclear.

INTRODUCTION

The durability and defect/damage tolerance characteristics of advanced materials are of considerable importance in the design of reliable safety-critical structures. These aspects are particularly relevant for the successful application of low density aluminum-lithium alloys, as they are targeted for high performance aerospace applications, replacing traditional 2000 and 7000 series aluminum alloys.

Studies to date indicate that the fatigue crack growth resistance of Al-Li alloys is superior to conventional aluminum alloys. This behavior is

* Center for Advanced Materials, Lawrence Berkeley Laboratory, and Department for Materials Science and Mineral Engineering, University of California at Berkeley, Berkeley, CA, 94720, USA.

+ Department of Materials Science, University of Virginia, Charlottesville, VA, 22901, USA.

Both extrinsic shielding and intrinsic crack tip damage processes are environment sensitive. For the former, corrosion products affect closure, however, environmental influences on surface roughness and crack wake plasticity are also possible [15]. Investigations of these processes are limited for aluminum alloys. An exception is moist air oxide induced crack closure which has a secondary influence on near-threshold crack propagation in Al alloys, in contrast to behavior in steel [6,24,25]. Additional work is required to explore the environmental mechanisms of crack tip shielding.

Hydrogen embrittlement and film rupture/anodic dissolution/ repassivation have been proposed as mechanisms of intrinsic crack tip damage for environmental fatigue of aluminum alloys. Studies of these mechanisms are hindered because of the inaccessibility of the crack tip to direct measurements, and because crack growth rate data are often obtained for closure dominant conditions which incorporate extrinsic and intrinsic damage. This latter problem has hindered acquisition and interpretation of meaningful corrosion fatigue crack propagation data for advanced Al-Li alloys. Recent successes in this regard are highlighted below.

Corrosion Fatigue Crack Propagation: Al-Li Alloys in Water Vapor

Water vapor enhances the rates of fatigue crack propagation in Al-Li alloys; the mechanism is likely hydrogen embrittlement. In these regards the crack growth behavior of Al-Li alloys is analogous to that of conventional 2000 and 7000 series Al alloys, as established by Wei and coworkers [22,26].

Typical data are presented in Fig. 7 for alloy 2090 [10,11]. Extrinsic and transient crack growth effects were minimized by experimental design; each data point represents about 0.3 mm of crack extension at constant ΔK. High ΔK data were obtained with short edge crack lengths (< 0.8 mm) at low R, while near-threshold data were obtained with longer cracks and $R > 0.85$. Intermediate growth rates were obtained at constant K_{max} with R values between these limits. Crack growth in moist air is represented by the solid line, consistent with Fig. 3. Growth rates in pure water vapor are similar to those for moist air and are enhanced relative to fatigue in purified helium, oxygen and dynamic vacuum. The environmental effect is maximum near the threshold and diminishes to nearly zero at the highest ΔK levels examined. The near-threshold regime has been largely unexplored, particularly void of closure effects.

Several mechanistic inferences are drawn from the data in Fig. 7. Crack growth is accelerated by hydrogen produced by the oxidation reaction between clean Al-Li at the crack tip and water vapor. Based on the equality of rates for oxygen and the inert environments, crack surface films do not affect crack growth by influencing the morphology and reversibility of plastic deformation. Speculatively, oxide formed in water vapor behaves similarly to that produced in dry oxygen. Similar crack growth rates in inert gas, vacuum and oxygen environments were reported for 2024 and 7075 alloys; at least at growth rates above 10^{-6} mm/cycle [26,27]. Secondly, the region of nearly K-independent crack growth in moist air and water vapor is environmental in origin. This behavior correlates with the ΔK level where the cyclic plastic

Al-Li alloys which promote crack deflection display lower crack growth rates when compared based on total applied stress intensity. For example, of the various peak-aged alloys, fine grained 8091 shows the most linear crack paths; crack growth rates are faster than the other alloys. Conversely in 2090, crack paths are highly deflected and branched; correspondingly this alloy exhibits the best "long crack" propagation resistance (Fig. 1).

The principal effect of deflected and tortuous crack paths in Al-Li alloys is to induce high crack closure levels. Slip band cracking along planes parallel to {111} is the dominant failure path for fatigue in moist air, at least within the Paris regime. (Additional cracking morphologies are possible, as discussed in an ensuing section.) As shown in Fig. 2a, marked slip planarity results in faceted crack growth along intersecting slip bands and promotes periodic deflection in the direction of crack growth. In addition the pronounced deformation texture in wrought Al-Li promotes faceted crack path tortuosity through the plate/specimen thickness (Fig. 2b). Planar slip induced meandering and deformation texture induced tortuosity lead to significantly slower growth rates by: i) increasing crack path length, ii) deflecting the crack from the plane of maximum tensile stress, and most importantly iii) developing high roughness-induced crack closure levels via the wedging of large fracture surface asperities within the crack (Fig. 2a).

Shielding mechanisms are common in coherent particle hardened aluminum alloys; however; their influence is generally limited to near-threshold ΔK levels, where the cyclic plastic zone size is comparable to the grain or subgrain size. Al-Li alloys are remarkable in that the faceted fracture mode, and hence high closure levels, persist to higher ΔK levels, accounting for improved crack growth properties up to 10^{-6} m/cycle.

Long-Crack Behavior: High, Programmed Stress Ratios

Fatigue crack propagation at high stress ratios provides a reasonable approach to examine microstructural and environmental effects on intrinsic crack propagation. In this regard, programmed load-shedding procedures based on decreasing ΔK at constant K_{max}, therefore increasing R, provide meaningful results [13]. Typical data are presented in Fig. 3 for Al-Li alloys.

In the absence of significant closure, likely at stress ratios above about 0.8, Al-Li-Cu alloys exhibit equivalent growth rates compared to other 2000 series alloys. Faster growth rates are observed for 7000 series alloys, perhaps due to the enhanced environmental sensitivity of these materials. When compared to low R growth rate data, based on applied ΔK, results of high mean stress experiments show greatly reduced values of ΔK_{th} and reduced variability for different microstructures (Fig. 1 compared to Fig. 4).

Comparison of programmed high R data with crack growth rates plotted in terms of effective stress intensity range ($\Delta K_{eff} = K_{max} - K_{cl}$) indicates the propriety of the former for measurements of intrinsic cracking. A typical result for 2090 (LT) is plotted in Fig. 3. For this alloy, the two methods provide upper and lower bounds for the intrinsic threshold. High stress ratio data are realistic, provided that the shielding closure is minimal; a fact

zone diameter is less than the subgrain size of about 10 μm. Coupled with fractographic findings, this result suggests that hydrogen transport within the plastic zone determines the shape of the intrinsic da/dN (ΔK) relationship.

The ratio of water vapor partial pressure to loading frequency is the primary variable which controls corrosion fatigue crack propagation in Al-Li alloys [10,11]. For fixed frequency (5 Hz), constant environmental growth rates are observed for water vapor pressures above 0.5 Pa; da/dN decreases with decreasing pressure below this saturation level and reaches the inert environment rates shown in Fig. 7. This result has two implications. The "saturation" water vapor pressure is extremely low, particularly for near-threshold cracking. Ultra-high vacuum (better than 1 μPa with minimal wall outgassing and leakage), or very high loading frequencies (above 30 Hz), are required to obtain truly "inert environment" fatigue data. Experiments with Al-Li alloys in moderate vacuum systems will yield crack growth data which are equivalent to values for water vapor or moist air. Secondly, the behavior of Al-Li alloys is well described by a fast surface reaction/gas phase mass transport limited crack growth model developed by Wei and coworkers for 2000 and 7000 series alloys [26]. The saturation pressure is possibly lower than that predicted by the transport model, and indicative of localized slip deformation or discontinuous crack propagation. This calculation is clouded by uncertainties in the geometric parameters which describe impeded molecular (Knudsen) flow, particularly at high R.

Corrosion Fatigue Crack Propagation: Al-Li-Cu in Aqueous Chloride

Aqueous chloride solutions enhance rates of fatigue crack propagation in Al-Li alloys; the damage mechanism is unclear, although both hydrogen embrittlement and dissolution/film rupture are possible. Typical data are presented in Fig. 8 for peak-aged alloy 2090 [10,12]. Extrinsic and transient crack growth effects were minimized, as discussed for Fig. 7. Compared to inert helium, the NaCl environment enhances rates of crack propagation for both anodic and cathodic polarizations. Crack growth rates are particularly increased near-threshold. These data are comparable to recent results of Yoder and coworkers on alloy 2090 [28], which were; however; limited to relatively high levels of K and low R with a substantial closure influence.

For corrosion fatigue, crack geometry dependent occluded cell mass transport and time dependent chemical reactions can cause nonsteady-state crack growth which is poorly described by applied ΔK [15,22,23]. Crack growth rate laws are not unique; for example, short cracks can grow at remarkably fast rates compared to long cracks and due to chemical mechanisms [29]. This issue, an extrinsic effect of sorts, has not been explored for environmental cracking of aluminum alloys. Results for alloy 2090 in Fig. 8 provide some insight in this regard. The corrosion fatigue behavior of short cracks sized between 0.2 and 2 mm is identical to that of long cracks for NaCl. No evidence is available to suggest that short corrosion fatigue cracks grow at unpredictably rapid rates.

Two variables strongly influence corrosion fatigue crack propagation in aluminum alloys exposed to aqueous chloride: cyclic loading frequency and

moist air, pure water vapor and aqueous NaCl), cracking proceeds along several microscopic paths [10]. Slip band cracking occurs at high stress intensities and for chemical conditions where environmental cracking is reduced. In this ΔK regime, intersubboundary cracking is observed for water vapor and NaCl; the proportion of this mode increases and slip band cracking decreases as stress intensity is reduced. Cleavage is the dominant fracture mode in hydrogen producing environments near-threshold. Notably, subboundary cracking transitions to cleavage with decreasing ΔK in the vicinity of the "plateau" in the da/dN (ΔK) relationship, Figs. 7 and 8. Etch pit studies establish that cleavage occurs along either {100} or {110} planes; the exact facet orientation is not yet defined. The occurrence of cleavage is consistent with the behavior of 7000 series alloys [26,31].

Future Research

Corrosion fatigue crack growth rates and fractographic measurements are limited to peak-aged alloy 2090; work is required to determine the behavior of Al-Li-Cu alloys which contain substantial amounts of magnesium. Grain size, strengthening precipitate/dispersoid and cyclic deformation mode effects on intrinsic corrosion fatigue crack growth must be characterized and modeled. Environmental effects near-threshold are particularly important in these regards. In addition to intrinsic damage mechanisms, environmental effects on crack tip shielding must be explored.

For fatigue in water vapor, the mass transport and reaction model must be further developed and tested, particularly for the threshold regime. The effect of surface oxide films on crack tip plasticity must be more broadly characterized. The mechanism by which hydrogen promotes the various brittle crack paths must be determined.

For crack growth in aqueous electrolytes, crack chemistries must be modeled and measured for reasonable corrosion fatigue conditions. Coupled micromechanical-crack chemistry models will identify the contributions of anodic dissolution, hydrogen uptake and film rupture, and explain the effects of variables such as frequency and electrode potential.

Comparisons with Conventional Aluminum Alloys

The environmental cracking resistance of Al-Li alloys is often intuitively judged to be low due to the "reactivity" of lithium and to the well known sensitivity of these alloys for intergranular stress corrosion cracking. This assessment is false.

From an applications perspective, the corrosion fatigue resistance of commercial aluminum-lithium alloys is good, comparable to the behavior of 2000 series alloys and improved compared to 7000 series Al alloys which are of known sensitivity to hydrogen embrittlement. Specific data are presented in Fig. 9 [21]. Behavior in the low R, high ΔK regime demonstrates similar cracking in Al-Li-Cu alloy 2090 and conventional alloys 2024 and 2618 exposed to NaCl at typical free corrosion potentials for aerated solutions. The environmental effect is small compared to helium or vacuum and is

7. Venkateswara Rao, K.T., Yu, W. and Ritchie, R.O., Metall. Trans. A, Vol. 19A, 1988, pp. 563-69.

8. Venkateswara Rao, K.T. and Ritchie, R.O., Mater. Sci. Technol., Vol. 6, 1989, in press.

9. Venkateswara Rao, K.T. and Ritchie, R.O., Mater. Sci. Technol., Vol. 6, 1989, in press.

10. Piascik, R.S., "Intrinsic Damage Mechanisms for Environmental Fatigue Crack Propagation in Al-Li-Cu Alloys", Ph.D. Dissertation, University of Virginia, in preparation, 1989.

11. Piascik, R.S. and Gangloff, R.P., in "Advances in Fracture Research". Edited by K. Salama, K. Ravi-Chandar, D.M.R. Taplin and P. Rama Rao, Pergamon Press, London, 1989, pp. 907-918.

12. Piascik, R.S. and Gangloff, R.P., "Aqueous Environment Effects on Intrinsic Corrosion Fatigue Crack Propagation in an Al-Li-Cu Alloy", in "Environment Induced Cracking of Metals". Edited by R.P. Gangloff and M.B. Ives, NACE, Houston, TX, in press, 1989.

13. Herman, W.A., Hertzberg, R.W. and Jaccard, R., Fat. Engr. Matls. and Struc., Vol. II, 1988, pp. 303-320.

14. Donald, J.K., Fracture Technology Associates, Unpublished Research, 1989.

15. Gangloff, R.P. and Ritchie, R.O., in "Fundamentals of Deformation and Fracture". Edited by B.A. Bilby, K.J. Miller and J.R. Willis, Cambridge University Press, Cambridge, UK, 1985, pp. 529-558.

16. Ritchie, R.O. and Lankford, J., Matls. Sci. and Engr., Vol. 84, 1986, pp. 11-16.

17. Gangloff, R.P., in "Advances in Crack Length Measurement". Edited by C.J. Beevers, EMAS, United Kingdom, 1982, pp. 175-231.

18. Venkateswara Rao, K.T. and Ritchie, R.O., in "Advances in Fracture Research". Edited by K. Salama, K. Ravi-Chandar, D.M.R. Taplin and P. Rama Rao, Pergamon Press, London, in press, 1989.

19. Chanani, G.R., Scarich, G.V. and Bresnahan, K.M., in "Mechanical Properties and Phase Transformations in Engineering Materials". Edited by S.D. Antolovich, R.O. Ritchie and W.W. Gerberich, TMS-AIME, Warrendale, PA, 1986, pp. 271-291.

20. Bucci, R.J., Mehr, P.L., Sowinskki, G., Malcolm, R.C., Kaiser, W.T. and Wygonik, R.H., Alcoa Technical Report No. 57-88-30, Pittsburgh, PA, 1988.

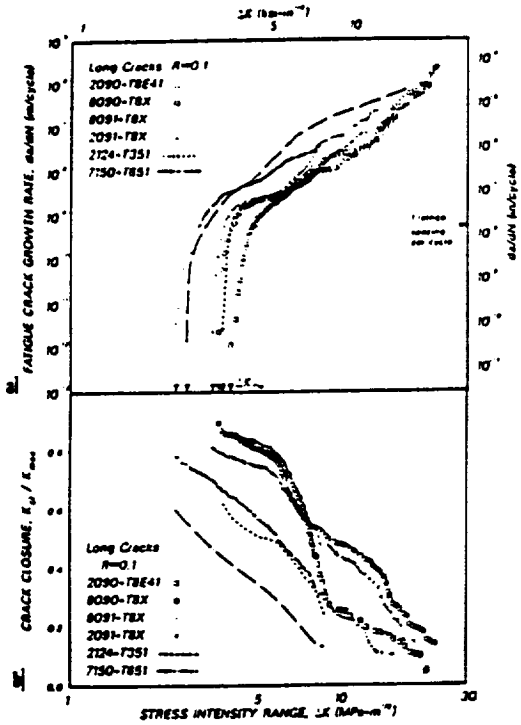

Fig. 1: a) Constant amplitude fatigue crack propagation rates and b) corresponding crack closure levels for long cracks in peak-aged Al-Li alloys 2090, 2091, 8090, 8091, and conventional aerospace aluminum alloys 2124-T351 and 7150-T651 (LT orientation, R = 0.1). Note the superiority of lithium containing alloys, consistent with high closure levels [9].

Fig. 2: Crystallographic crack path tortuosity observed during fatigue crack growth in Al-Li alloys, induced by a) planar slip in the direction of crack growth (arrow), and b) pronounced texture through the plate thickness. As shown in (a), deflected crack paths promote premature crack surface contact, viz. roughness-induced crack closure. 2090-T8E41 alloy plate tested in the LT orientation, R=0.1 [9].

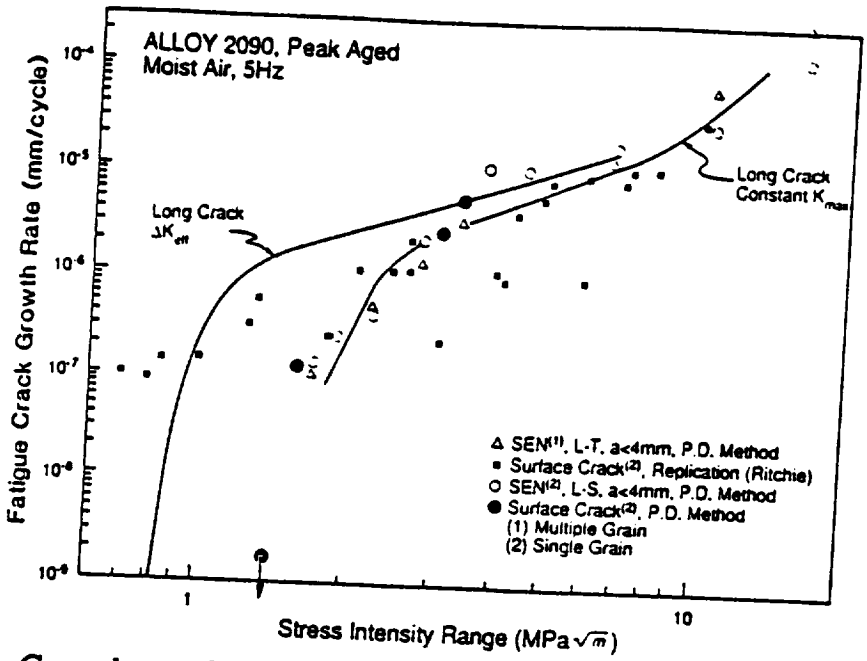

Fig. 5: Growth rate behavior of microstructurally small (2 to 1000 μm) surface cracks (replication); small surface (100 to 400 μm) or through-thickness (300 to 4000 μm) cracks continuously monitored by electrical potential; and long ($\geq$ 10 mm) cracks in peak-aged 2090, as a function of ΔK. Note the close correspondence between long and small crack behavior when the former are corrected for closure in terms of ΔK_{eff} or constant K_{max} procedures [10].

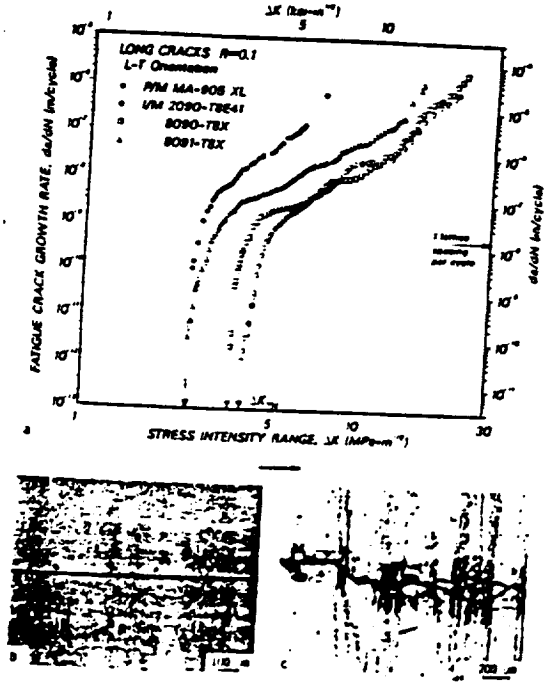

Fig. 6: Comparison of a) fatigue crack growth rates and b,c) crack paths in Al-Li alloys processed through ingot metallurgy (2090, 8090 and 8091) versus powder metallurgy (mechanically alloyed Novamet MA905-XL). Growth rates in the fine grained P/M alloy are 1 to 2 orders of magnitude faster, consistent with a linear crack paths and lower closure levels [18].

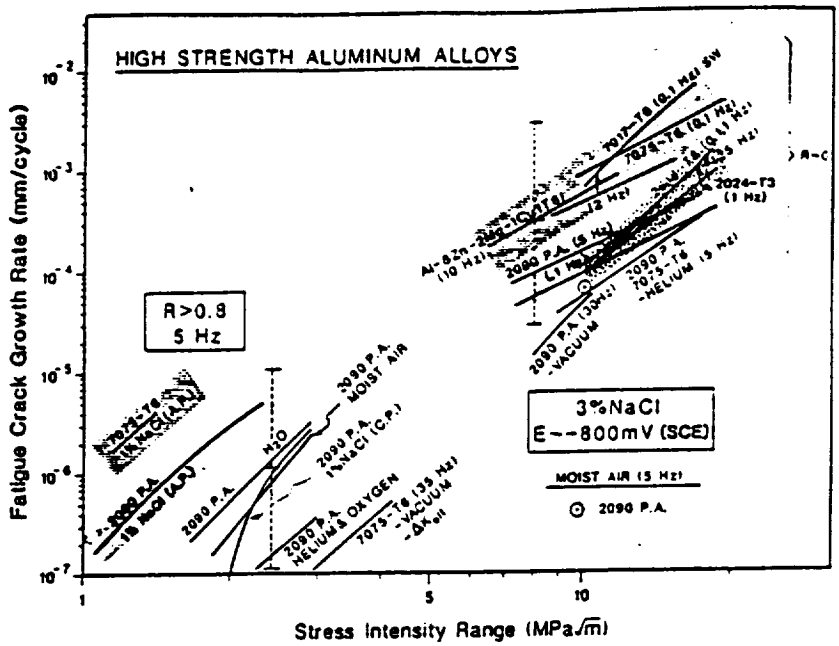

Fig. 9: Corrosion fatigue crack growth properties of Al-Li alloy 2090 compared to traditional high strength aluminum alloys in aqueous and gaseous environments. Note the superior environmental crack growth resistance of Al-Li alloys, similar to other 2000 series materials [10].

A90-41491

AGE HARDENING CHARACTERISTICS AND MECHANICAL BEHAVIOR OF Al-Cu-Li-Zr-In ALLOYS

John A. Wagner
NASA Langley Research Center, Metallic Materials Branch
Hampton, VA

Abstract

An investigation was conducted to determine the age hardening response and cryogenic mechanical properties of superplastic Al-Cu-Li-Zr-In alloys. Two alloys with compositions Al-2.65Cu-2.17Li-0.13Zr (baseline) and Al-2.60Cu-2.34Li-0.16Zr-0.17In were scaled-up from 30 lb. permanent mold ingots to 350 lb. DC (direct chill) ingots and thermomechanically processed to 3.2 mm thick sheet. The microstructure of material which contained the indium addition was partially recrystallized compared to the baseline suggesting that indium may influence recrystallization behavior. The indium-modified alloy exhibited superior hardness and strength compared to the baseline alloy when solution heat treated at 555°C and aged at 160°C or 190°C. For each alloy, strength increased and toughness was unchanged or decreased when tested at -185°C compared to ambient temperature. By using optimized heat treatments, the indium-modified alloy exhibited strength levels approaching those of the baseline alloy without deformation prior to aging. The increase in strength of these alloys in the T6 condition make them particularly attractive for superplastic forming applications where post-SPF parts can not be cold deformed to increase strength.

Introduction

Cryogenic fuel tanks are responsible for a large portion of the structural weight of current and proposed launch vehicles. Currently, conventional 2219 aluminum alloy is used to fabricate the Space Shuttle external tanks. The integrally stiffened tanks are machined from 38.1 mm thick plate, with approximately 75% of the starting plate removed as scrap. Therefore, it is possible that a significant improvement in material buy-to-fly ratio can be made by using advanced processing techniques and advanced alloy systems to manufacture cryogenic tanks for future launch vehicles. Specifically, it is envisioned that by using Al-Li alloys and superplastic forming (SPF) techniques, a significant cost and weight savings could be realized in the fabrication of expendable cryotanks.

Expendable tanks will be used to contain liquid hydrogen (-253°C) and liquid oxygen (-173°C) propellants. Therefore, alloys used in the fabrication of these tanks must exhibit high strength, toughness and stiffness at cryogenic operating temperatures. Recent work on Al-Cu-Li-Zr alloys has shown that this alloy family exhibits dramatically improved strength-toughness combinations at low temperatures (1) compared to conventional aluminum alloys, making them appealing candidate materials for cryogenic tank applications.

One alloy being investigated in the current study is of a 2090-type composition with a minor alloy addition of indium. Al-Li alloys have lower density, higher modulus and good cryogenic properties compared to conventional aerospace aluminum alloys, making them attractive for cryogenic tank application. Because the 2090+In alloy can be superplastically formed (2), major machining requirements and scrap handling can be reduced, and the poor mechanical properties associated with thick plate Al-Li alloys can be avoided. Furthermore, increased formability associated with SPF will provide additional weight savings by permitting the forming of complex stiffener configurations with increased structural efficiencies. It has also been observed that 2090+In exhibits strength levels approaching those of the base alloy in the T8 condition without the need for deformation prior to aging (3). This makes 2090+In particularly attractive for superplastic forming where post-SPF parts can not be deformed to increase strength levels.

The objectives of this investigation were to demonstrate that the beneficial effect of minor alloy additions of indium on the hardness and strength of 2090 based alloys could be scaled-up from a 30 lb. laboratory permanent mold casting to a 350 lb. DC (direct chill) casting, and to investigate ambient flow and fracture properties of the scaled-up indium-modified alloy. Finally, the cryogenic behavior of Al-Cu-Li-Zr-In sheet alloys was evaluated and compared to those of 2219 aluminum alloy, the current cryogenic tank material.

Experimental Materials and Test Methods

The Al-Li base alloy used in this investigation had a composition similar to alloy 2090 (4) as shown in Table I. The second alloy contained indium added to the base 2090 composition. Iron and silicon levels were minimized to reduce cavitation at constituent particles during SPF. Both the baseline and the indium bearing materials were produced from 350 lb. DC cast pilot ingots. Also shown in Table I are the various product forms and process histories of the alloys evaluated in this investigation. The material was hot rolled at 468°C to a thickness of 15.9 mm and thermomechanically treated according to a thermomechanical schedule used to process material for subsequent SPF (TMT C, ref.2). This schedule consists of a homogenization treatment at 538°C, cold water quench, and overage at 413°C for 16 hours. In the overaged condition, the material was preheated to 288°C and rolled to 3.2 mm with 288°C reheats.

Table I. Chemical Compositions and Process Histories of Al-Cu-Li-Zr and Al-Cu-Li-Zr-In Alloys

Alloy 2090: Al-2.65Cu-2.17Li-0.13Zr-0.06Fe-0.05Si (wt%)
2090+In: Al-2.60Cu-2.34Li-0.16Zr-0.05Fe-0.04Si-0.17In (wt%)

Material available:

1. 2090 Base chemistry		
- 3.2mm sheet	SHT	3% stretch
- 3.2mm sheet	TMT C	
2. 2090 + In		
- 3.2mm sheet	TMT C	

Differential scanning calorimetric (DSC) studies were conducted to identify the appropriate solution heat treatment. A typical DSC scan is presented in Fig. 1 and shows that there is a fairly narrow window between the dissolution of T_2 and where incipient melting occurs. After processing according to TMT C, a solution heat treatment temperature of 555°C and aging temperatures of 160°C or 190°C were used in this study.

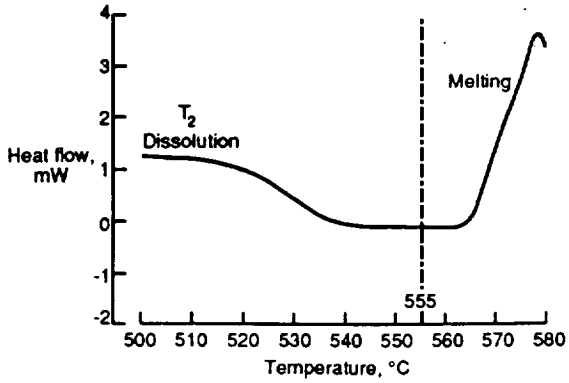

Figure 1 - Differential Scanning Calorimetric Scan of 2090 + In alloy.

Aging behavior of sheet material was characterized by hardness tests conducted at 23°C. Mechanical properties were evaluated using uniaxial tensile and notched Kahn Tear tests at room temperature and -185°C. Specimens were solution heat treated at 555°C and aged at 160°C for times of 20, 75 and 120 hours. The lower of the two aging temperatures was used to avoid the copious grain boundary precipitation that occurs at higher aging temperature and leads to deleterious effects on the fracture behavior of Al-Li alloys (5). Tensile specimens, 3.2 mm square in cross section, were machined from both Al-Li alloys and 2219-T87 in the

longitudinal direction. Data from back-to-back strain gages and extensometers were used to determine modulus and elongation, respectively. The Kahn Tear test was used to obtain a relative toughness ranking of these alloys. Specimens, 3.2 mm thick, were machined in the LT orientation with a notch root radius of 0.013 mm, Fig. 2. Tests were conducted on a servohydralic test machine operated in stroke control at an actuator speed of 1.27 mm/minute with load, actuator displacement and temperature continuously monitored. Tear strength (TS), unit initiation energy (UIE) and unit propagation energy (UPE) were calculated using the methods outlined by Kaufman et al. (6-8). The expressions used to evaluate these quantities are shown below and illustrated in Fig. 2:

Tear Strength, $TS=P/A+MC/I=P/bt+3P/bt=4P/bt$

Unit Initiation Energy, UIE=initiation energy/bt

Unit Propagation Energy, UPE=propagation energy/bt

where: P=maximum load
A=net section area
M=bending moment
C=distance from centroid to extreme fibers
I=moment of inertia
b=total ligament length from notch tip
t=thickness

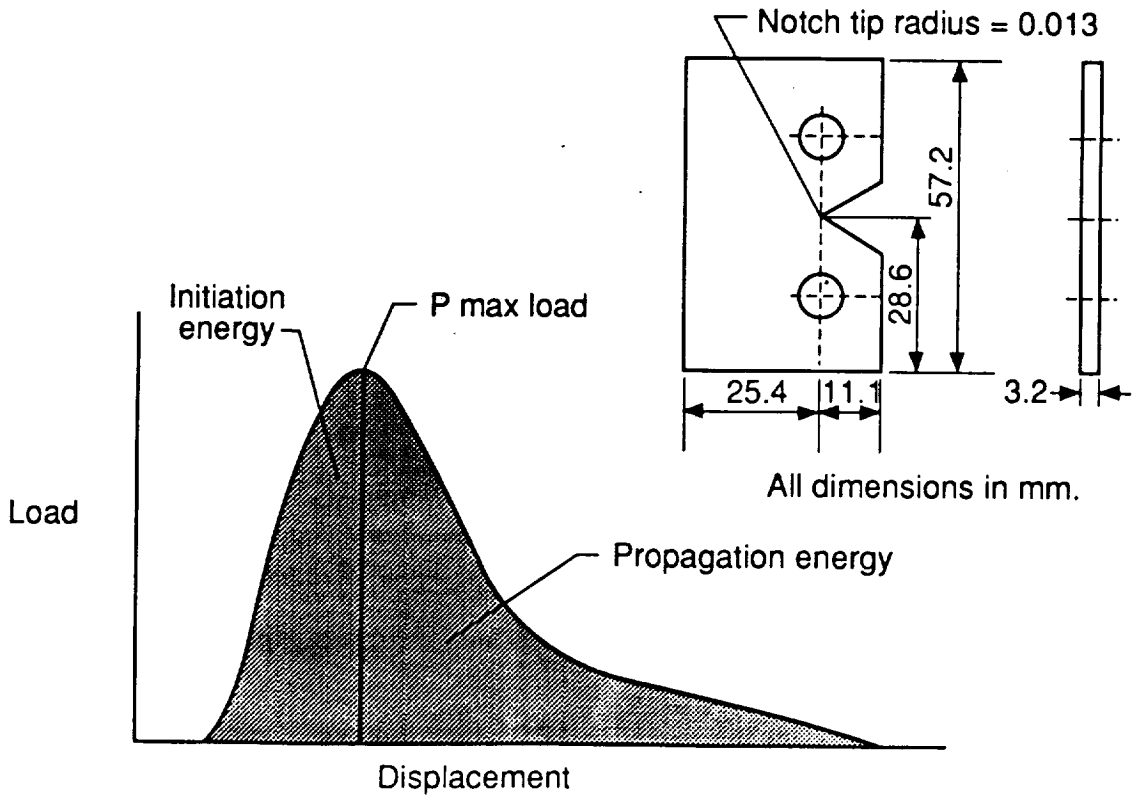

Figure 2 - Kahn Tear specimen and typical load-displacement record.

Results and Discussion

Microstructures

Optical microscopy revealed that there was a significant difference in recrystallization behavior due to the combined effect of the addition of indium and the processing schedule, TMT C. Photomicrographs of two sheet alloys are shown in Fig. 3. The Al-Cu-Li-Zr (2090) and the Al-Cu-Li-Zr-In (2090+In) in the T6 (unstretched) condition were processed according to TMT C, solution heat treated, and aged at 160°C for 75 hrs. The baseline 2090-T6 microstructure was characterized by fine subgrains typical of a recovered structure. The 2090+In alloy exhibited a partially recrystallized structure resulting from growth of selective subgrains within several adjacent prior high angle grains. The baseline 2090 alloy in the T8 (stretched) condition had an optical microstructure very similar to the baseline 2090-T6, but with a corresponding higher number density of precipitate phases (9).

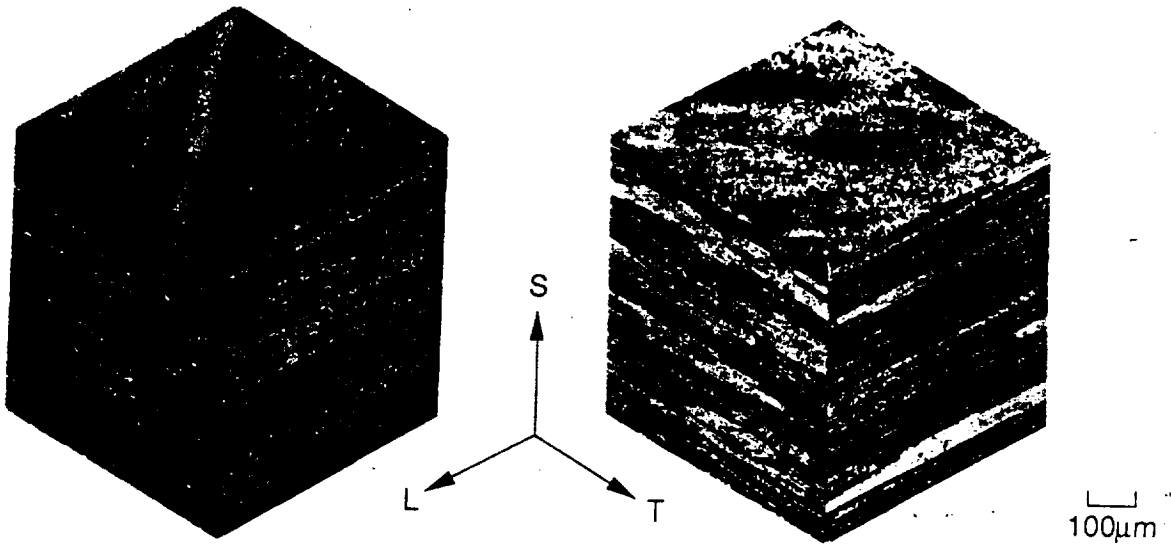

Figure 3 - Microstructure of Al-Li alloys which have been processed according to TMT C, solution heat treated and aged at 160°C for 75 hours.

Since 2090-T6 and 2090+In-T6 were processed using the same thermomechanical treatment, it appears that the addition of indium to the baseline composition is influencing the recrystallization behavior of that alloy. Further studies will be necessary in order to determine which variable(s) (the indium addition and/or the thermomechanical treatment variation) is affecting the recrystallization behavior of this alloy family.

Aging Kinetics

The isothermal aging responses of alloys which have been solution heat treated at a temperature of 555°C and aged at 160°C and 190°C are summarized in Figs. 4 and 5.

The age hardening response of an alloy which was prepared with an addition of indium is presented in Fig. 4. Also plotted is the behavior of 3.2 mm baseline material in the T6

(unstretched) and T8 (stretched) conditions. In the T6 condition, the 2090+In alloy obtained a higher hardness for a given aging time compared to the baseline 2090 alloy. Furthermore, the addition of indium promoted high hardness levels, similar to the effect of stretch deformation in the T8 condition. The higher hardness associated with the indium-modified alloy is most

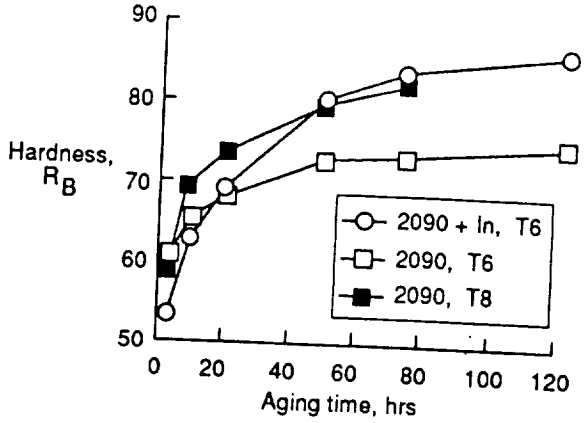

Figure 4 - Hardness, R_B, as a function of aging time for 2090 and 2090 + In processed according to TMT C, solution heat treated at 555°C and aged at 160°C.

apparent at longer aging times. The hardening response of the same group of alloys, but aged at 190°C, is shown in Fig. 5, where the beneficial effect of the indium addition is again apparent. In addition, the aging kinetics of the T8 alloy were more rapid than the T6 alloys when age hardened at 190°C.

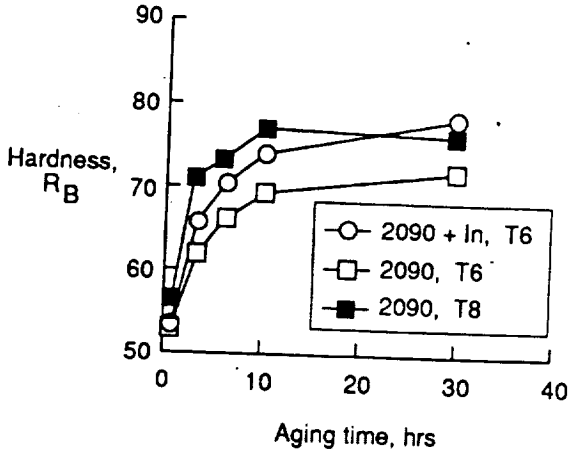

Figure 5 - Hardness, R_B, as a function of aging time for 2090 and 2090 +In aged at 190°C.

The change in the aging response of the indium bearing alloy supports the conclusions of Blackburn et al. (9). This previous study used material which was processed from laboratory (30 lb.) permanent mold castings. The change in the aging behavior of 2090+In was attributed to an increased number density and homogeneity of T_1 and theta-prime phases. In the present study, indium also had a significant effect on aging behavior, increasing the hardness of the T6 alloy to a level approaching that of the baseline T8 without the need for deformation prior to aging. However, mechanisms to explain these results are complicated by differences in the microstructure of the two alloys. The 2090+In alloy had a more recrystallized structure compared to the baseline.

Mechanical Behavior

1. Tensile Properties

Results of uniaxial tensile tests conducted at room and cryogenic temperatures are summarized in Table II. Each value represents the average of two tests except where noted.

Table II. Tensile Results of Al-Li and 2219 Alloys

Alloy	Aging Time hrs.	Temp. C	YS MPa	UTS MPa	Modulus GPa	Elongation %
2090+In-T6	20	23	321	425	78.6	5.9
		-185	358	533	79.3	13.2*
	75	23	370	496	79.3	7.1
		-185	440	561	89.6	12.5*
	120	23	388	506	79.3	10.4
		-185	434	584	83.4	10.4*
2090-T6	20	23	328	429	77.9	7.6
		-185	357	528	81.4	15.0*
	75	23	365	456	80.0	4.8*
		-185	381	536	81.4	10.5*
	120	23	390	471	78.6	3.4*
		-185	382*	512*	80.7*	
2090-T8	20	23	412	470	78.6	4.3*
		-185	467	577	80.7	12.1*
2219-T87		23	381	474	71.7	10.8
		-185	450	577	73.1	12.3

*Value from one test only

At room temperature, alloying with indium increased the ultimate tensile strength of 2090 based alloys, but had no effect on yield strength as shown in Fig. 6. The addition of indium, however, was not as effective as using a post-solution heat treatment stretch to increase the ultimate strength. Specifically, 2090-T8 had higher strength compared to the base 2090-T6 and 2090+In-T6 at an aging time of 20 hours. This result is consistent with hardness values shown in Fig. 4 for an aging time of 20 hours at 160°C. Another observation that can be made from Fig. 6, is that there was a continuous increase in yield strength and ultimate tensile strength with increasing aging time for both alloys. This indicates that substantial overaging, as measured by yield strength, did not occur even at an aging time of 120 hours.

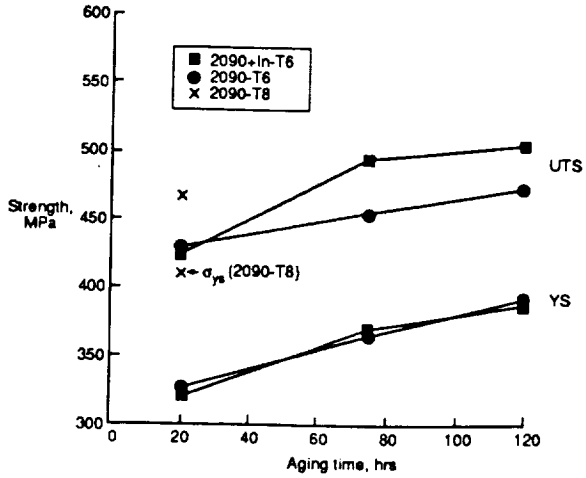

Figure 6 - Variation in room temperature strength with aging time at 160°C.

At cryogenic temperatures, the addition of indium significantly increased the ultimate tensile strength, and notably also the yield strength, Fig. 7. Furthermore, Fig. 8 shows that there was an improvement in yield and ultimate tensile strengths of 2090 baseline and 2090+In-T6 alloys at cryogenic temperatures; behavior which is characteristic of Al-Li alloys. Increased strength of Al-Li alloys at low temperatures has been related to an increase in the thermal component of strength due to the temperature dependence of solute atoms which act as weak barriers to dislocation movement and to an increase in the strain hardening rate (10,11). Finally, the cryogenic yield and ultimate tensile strengths of 2090-T8 were higher than both 2090 baseline and 2090+In-T6, similar to the trends observed at room temperature.

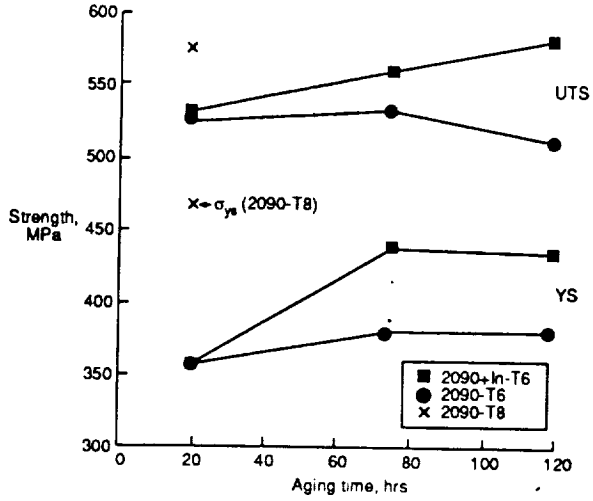

Figure 7 - Variation in cryogenic strength with aging time at 160°C.

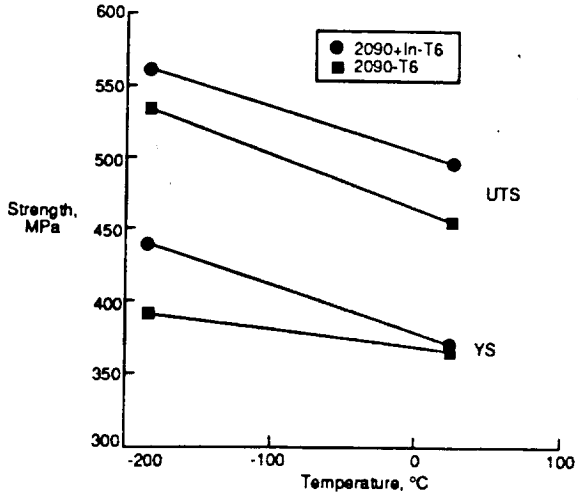

Figure 8 - Ambient and cryogenic tensile properties of 2090 and 2090 + In aged at 160°C for 75 hours.

Increases in the elongation and modulus at cryogenic temperatures are also common for Al-Li alloys and the data from the present investigation are consistent with this trend (1,12). The overall trend was for a significant increase in elongation to failure at -185°C. It is also apparent that the improvement in strength from indium additions did not result in loss of ductility. Most of the alloys in this study also showed a modest increase in the cryogenic modulus of approximately 2%, however, the 2090+In alloy exhibited an increase in the cryogenic modulus of approximately 11% at an aging time of 75 hours and approximately 5% at an aging time 120 hours.

Conventional cryogenic tank material 2219-T87 showed the same trend of increasing strength, elongation and modulus with decreasing temperature as did the Al-Li alloys. However, 2219-T87 had a much lower modulus at both 23°C and -185°C.

Comparison of the hardness behavior in Fig. 4 with the ambient ultimate tensile properties in Fig. 6 revealed that in both cases the addition of indium had its most pronounced effect at longer aging times. Furthermore, the observation that indium enhanced the ambient ultimate tensile strength, but had no effect on the yield strength suggests that indium promotes work hardening in these alloys. However, this hypothesis is complicated by the fact that the microstructure of the indium-modified material was partially recrystallized. The decrease in yield strength typically associated with a partially recrystallized structure could be offsetting any beneficial that indium has on the ambient yield strength. The actual mechanism by which indium additions improve the yield strength at cryogenic temperatures remains to be determined.

2. Kahn Tear Tests

The Kahn Tear test, because of its advantage in terms of simplicity and specimen size, was used to rank alloys and tempers in terms of relative toughness. Historically, two parameters from the Kahn Tear test, UPE and tear strength to yield strength ratio (TS/YS), have been used to screen sheet toughness of aluminum alloys. There are, however, some problems associated with this approach. For example, the separation of initiation energy and propagation energy at maximum load, Fig. 3, is arbitrary and does not necessarily coincide with the actual load and deflection at which a crack initiates from the machined notch. Also, traditional correlations of UPE with K_{Ic} seem inappropriate for Al-Li alloys where crack deflection during the tear test is common and results in a measured propagation energy which has no relationship to material initiation toughness. Therefore, the tear strength to yield strength ratio which measures the resistance of a material to fracture in the presence of a stress raiser (6) was used as a relative measure of the toughness of the Al-Li alloys in this study.

Results of Kahn Tear tests at ambient and cryogenic temperatures are shown in Table III. Conventional cryotank material 2219-T87 exhibited relatively no change in the TS/YS ratio and an increase in UPE at cryogenic temperatures consistent with other investigations (8,13). In contrast, the baseline 2090-T8 alloy had lower toughness at cryogenic temperatures.

Figs. 9 and 10 show the variation in tear strength to yield strength ratio with temperature for 2090+In and 2090 alloys in the three aging conditions studied in this investigation. Both alloys exhibited a significant decrease in the tear strength to yield strength ratios with increasing aging time when tested at room and cryogenic temperatures. The relative decrease in toughness with increasing aging time can be attributed to increased yield strength and to an increase in grain boundary precipitates at longer aging times which promote intergranular microvoid fracture in Al-Li alloys (14).

Table III. Kahn Tear Results of Al-Li and 2219 Alloys

Alloy	Aging Time hrs.	Temp. C	TS MPa	UIE Nmm/mm^2	UPE Nmm/mm^2	TS/YS
2090+In-T6	20	23	487	96.0	43.3	1.52
		-185	460	70.2	9.5	1.29
	75	23	394	59.7	1.2	1.07
		-185	346	32.8	1.7	0.79
	120	23	307	28.4	0.3	0.79
		-185	304	25.9	0.5	0.70
2090-T6	20	23	502	111.9*	53.8*	1.53
		-185	523	93.3	23.6	1.47
	75	23	401	58.8	11.2	1.10
		-185	397	46.2	3.5	1.04
	120	23	393	69.5*	2.1*	1.01
		-185	362	37.7	2.1	0.95
2090-T8	20	23	465	82.3*	14.5*	1.13
		-185	438	58.3	7.9	0.94
2219-T87		23	483	98.6	19.1*	1.27
		-185	565	96.0*	34.3	1.26

*Value from one test only

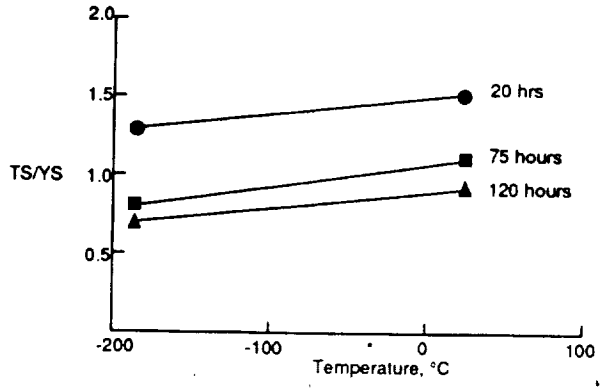

Figure 9 - Tear strength to yield strength ratio of 2090 + In-T6 at -185°C and 23°C for various aging times at 160°C.

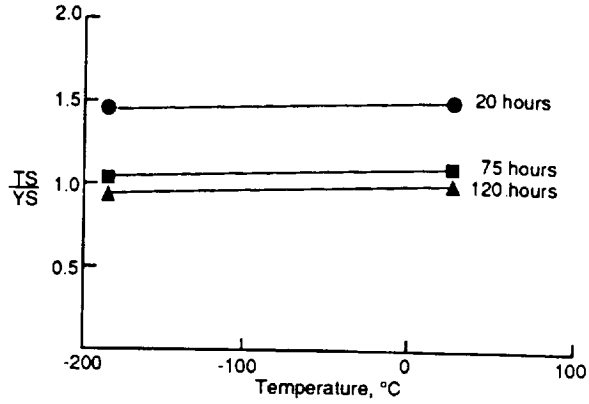

Figure 10 - Tear strength to yield strength ratio of 2090-T6 at -185°C and 23°C for various aging times at 160°C.

The 2090+In and 2090 baseline alloys both exhibited a decrease in relative toughness when tested at cryogenic temperatures as indicated by the decrease in tear strength-yield strength ratios shown in Figs. 9 and 10, respectively. The decrease in the cryogenic toughness of these Al-Li alloys tested in the LT orientation is contrary to many literature results reported to date. For example, significant increases in toughness at cryogenic temperatures have been observed for many Al-Li plate alloys: 2090- T8E41 (1,15), 2090-T8X (16), 2090-T81, 2090-T351, 8090-T8X and 8091-T8X (15). The mechanisms to account for the increase in toughness at low temperatures focus on higher strain hardening rates at cryogenic temperatures and the loss of through thickness constraint from enhanced intergranular splitting, with no associated change in the fracture mode. In contrast, observed decreases in toughness at cryogenic temperatures have been reported for 2091-T8X, 8090-T351, and 8091-T351 plate alloys (15). Along with the decrease in toughness of these alloys, Rao et al. observed a change in fracture mode from ductile microvoid coalescence at ambient temperatures to transgranular shear with some delamination at cryogenic temperatures. In 2090 sheet alloy thermomechanically processed for SPF and peak aged (17), there was a change in fracture mode from ductile shear to increasingly intergranular fracture associated with a loss of toughness at cryogenic temperatures. In the present investigation, a decrease in toughness at cryogenic temperatures was also observed for sheet alloys which were thermomechanically processed and aged at 160°C for various times.

Conclusions

A study was conducted to determine the age hardening response and cryogenic mechanical properties of 2090 and 2090+In sheet alloys. Based on the results of this investigation the following conclusions can be made:

1. The effect of minor alloy additions of indium resulting in increased hardness and strength has been demonstrated for 350 lb. DC ingots of 2090 type alloys. A possible mechanism to account for this behavior could be related to enhanced work hardening.

2. Alloys in this study exhibited increases in yield strength, ultimate tensile strength, elongation to failure and modulus when tested at cryogenic temperatures similar to other Al-Li alloys.

3. The Al-Li alloys in this investigation exhibited a decrease in toughness, as measured by a decrease in tear strength-yield strength ratio, at cryogenic temperatures. This decrease could be related to differences in the microstructure associated with processing sheet material.

4. For alloys processed according to TMT C, solution heat treated and aged, indium additions to base chemistries promote recrystallization.

References

1. J. Glazer, S. L. Verzasconi, E.N.C. Dalder, W. Yu, R.A. Emigh, R.O. Ritchie and J.W. Morris, Jr., "Cryogenic Mechanical Properties of Al-Cu-Li-Zr Alloy 2090," Adv. Cryo. Eng. Mat., vol. 32, 1986, pp. 397-404.

2. S. P. Agrawal, "Enhancement of the Superplastic Formability and Post-SPF Properties in Al-Li Alloys," for presentation at the Fifth International Al-Li Conference, Williamsburg, VA, 1989.

3. L. B. Blackburn and E.A. Starke, Jr., "Microstructure-Mechanical Property Relationships for Al-Cu-Li-Zr alloys with Minor Additions of Cadmium, Indium or Tin," to be published in the Proceedings of the Symposium on Light-Weight Alloys for Aerospace Applications, TMS Annual Meeting, Las Vegas, NV, 1989.

4. Alcoa Green Letter No. 226: Alcoa Alloy 2090, Alcoa Laboratories, Alcoa Center, PA, 1988.

5. E. A. Starke, Jr., "A Review of the Development, Microstructure and Properties of New Al-Li Alloys," Proceedings 15th Congress of the International Council of the Aeronautical Sciences, eds. P. Santini and R. Staufenbiel, London, 1986, pp. 934-943.

6. J. G. Kaufman and Marshall Holt, "Fracture Characteristics of Aluminum Alloys," Technical Paper No. 18, Alcoa Laboratories, Alcoa Center, PA, 1965.

7. J. G. Kaufman and H. Y. Hunsicker, "Fracture Toughness Testing at Alcoa Research Laboratories," STP 381, ASTM, Philadelphia, 1965, pp. 290-309.

8. J. G. Kaufman and M. Holt, "Evaluation of Fracture Characteristics of Aluminum Alloys at Cryogenic Temperatures," Adv. Cryo. Eng., vol. 10, 1965, pp. 77-85.

9. L. Blackburn, W. Cassada, G. Colvin and E.A. Starke, Jr., "The Effect of Processing on the Microstructure, Strength and Fracture Behavior of Aluminum-Lithium Alloys," Aluminum-Lithium Alloys: Design, Development and Application Update, eds. R.J. Kar et al., ASM, Metals Park, Ohio, 1988, pp. 187-235.

10. J. W. Morris, Jr. and J. Glazer, "Mechanical Properties of High Strength Aluminum Alloys at Cryogenic Temperatures," presented at the 1988 International Cryogenic Materials Conference, Shenyang, China.

11. J. Glazer and J.W. Morris, Jr., "Tensile Properties of Commercial Aluminum-Lithium Alloys at Cryogenic Temperatures," presented at the 1988 ASM Aluminum-Lithium Symposium, Los Angeles.

12. J. Glazer, J.W. Morris, Jr., S.A. Kim, M.W. Austin and H.M. Ledbetter, " Temperature Variation of the Elastic Constants of Aluminum Alloy 2090-T81," AIAA Journal, vol. 25, No. 9, 1987, pp. 1271-1272.

13. J.G. Kaufman, F.G. Nelson and E.W. Johnson, "The Properties of Aluminum Alloy 2219 Sheet, Plate and Welded Joints at Low Temperatures," Adv. Cryo. Eng., vol. 8, pp. 661-670.

14. S. Suresh, A.K. Vasudevan, M. Tosten and P.R. Howell, "Microscopic and Macroscopic Aspects of Fracture in Lithium-Containing Aluminum Alloys," Acta Met., vol. 35, 1987, pp. 26-46.

15. K. T. Venkateswara Rao, Weikang, Yu and R.O. Ritchie, "Cryogenic Toughness of Commercial Aluminum-Lithium Alloys: Role of Delamination Toughening," to be published Met. Trans. A., 1989.

16. R. C. Dorward, "Cryogenic Toughness of Al-Cu-Li Alloy AA 2090," Scripta Met., vol. 20, 1986, pp. 1379-1383.

17. J. Glazer, J. W. Morris, Jr. and T. G. Nieh, "Tensile Behavior of Superplastic Al-Cu-Li-Zr Alloy 2090 at Cryogenic Temperatures," Adv. Cryo. Eng., vol. 34, 1988, pp. 291-298.

Presented at the Fifth International Aluminum-Lithium Conference, Williamsburg,VA, March, 28th, 1989.

THE CORROSION BEHAVIOR OF THE T_1 (Al_2CuLi) INTERMETALLIC COMPOUND IN AQUEOUS ENVIRONMENTS

R.G. Buchheit and G.E. Stoner *

The intermetallic compound T_1 (Al_2CuLi) is suspected to play an important role in the localized corrosion at subgrain boundaries in Al-Li-Cu alloys. The intermetallic was synthesized for characterization of its corrosion behavior. Experiments performed included open circuit potential measurements, potentiodynamic polarization and corrosion rate vs. pH in solutions whose pH was varied over the range of 3 to 11. Subgrain boundary pitting and continuous subgrain boundary corrosion are discussed in terms of the data obtained in these experiments. Evidence suggesting the dealloying of copper from this compound is also presented.

INTRODUCTION

Aluminum-lithium-copper alloys have demonstrated a susceptibility to localized corrosion when exposed to aqueous chloride environments. The T_1 phase, the dominant subgrain boundary precipitate in Al-Li-Cu alloys, has been implicated in preferential subgrain boundary corrosion which is widely thought to contribute to intergranular and stress corrosion cracking in these alloys (1-7).

At least two mechanisms involving T_1 have been proposed for preferential subgrain boundary corrosion. The first mechanism proposes that the T_1 precipitate is the most active phase present

in 2090 and subgrain boundary corrosion proceeds by selective T_1 dissolution (1-6). This argument is based largely on the speculation that the high lithium content of the T_1 precipitate makes it an extremely active phase. A second, less widely accepted mechanism in Al-Li-Cu alloys proposes that a copper depleted zone forms along a subgrain boundary as subgrain boundary T_1 plates grow during aging (7). The copper depletion occurring in these zones renders them active and subgrain boundary corrosion proceeds as these regions dissolve. This mechanism, proposed to occur in Al-Cu and Al-Cu-Mg alloys (8-12), is based on the observation that as aging time increases, subgrain boundary pitting increases but matrix (subgrain interior) pitting does not.

Proponents of the second mechanism assert that the above observation is inconsistent with a selective T_1 dissolution mechanism since T_1 precipitation within subgrains occurs as the peak aging times are approached.

The first objective of this study was to synthesize the T_1 intermetallic in bulk form so that conventional electrochemical test techniques could be employed to generate ancillary data on its corrosion behavior. The second objective of this study was to compare the corrosion behavior of the precipitate phase to that of a copper depleted zone and the α-Al matrix to clarify the mechanism of subgrain boundary corrosion.

Open circuit measurements, cyclic potentiodynamic polarization and corrosion rate determinations were employed in

the present study. These experiments were carried out on three different materials intended to simulate the three different phases suspected to participate in subgrain boundary corrosion processes. Solution heat treated (SHT) 2090 was used to simulate an α-Al matrix, 1100 Al was used to simulate a copper depleted zone (a worst case scenario considering the ennobling effects of copper in aluminum) and the synthesized T_1 was used to simulate the subgrain boundary precipitate phase.

EXPERIMENTAL PROCEDURE

Materials Preparation

A 600 gram T_1 ingot was prepared by mixing stoichiometric amounts of Al (99.9), Cu (99.9) and Li (99.5). The components were melted in an induction furnace under 1 atm argon. The melt was allowed to solidify in the crucible. Qualitative analysis by X-ray diffraction was performed on two different powder samples collected while sectioning the ingot. All measured peaks corresponded to T_1 peaks suggesting that the ingot was largely T_1. The diffraction data and JCPDS Card File data are listed in Table 1. It should be noted that the relative intensities for some of the measured peaks are not consistent with those from the reference. However, the data cited in the JCPDS Card File were T_1 reflections obtained from X-ray diffraction of dilute Al-Li-Cu alloys while the peaks measured here were from a bulk sample (13). Pathological overlap of peaks from some other compound was considered as a factor contributing to the anomalous relative intensities. However, none of the possible compounds fit the measured peaks.

The 2090 alloy used in this study was provided by the Alcoa Technical Center, Pittsburgh, PA. The alloy was 38 mm plate solution heat treated and subjected to a 6 % stretch. The pure aluminum used here was a 99.99 % cast aluminum ingot.

The T_1 specimens were prepared for tests by sectioning using a low speed diamond wheel, mounting in epoxy and dry polishing through 600 grit SiC. The SHT 2090 and 1100 Al specimens were prepared by wet polishing through 600 grit SiC.

Open Circuit Potential Measurements

Open circuit potentials were measured for the synthesized T_1, 1100 aluminum and SHT 2090 using a PAR Model 173 Potentiostat/Galvanostat controlled by an electrochemical experiment software package. A PAR 276 Interface linked the potentiostat to an ATT PC which was used for data collection and storage. Measurements were made for each material in aerated 3.5 w/o NaCl solution, argon deaerated 3.5 w/o NaCl solution and per ASTM G69 (Measurement of Corrosion Potentials in Aluminum Alloys). In the deaerated and aerated solutions, the open circuit potential was monitored as a function of time until a steady-state response was obtained. The stabilized potential was then recorded. In the ASTM solution (58.5 g/l NaCl + 3 ml/l 30% H_2O_2), the open circuit potential was determined per the specification.

Potentiodynamic Polarization

Cyclic potentiodynamic polarization was performed on the T_1 ingot, 1100 aluminum and solution heat treated 2090 in aerated

and deaerated (argon) 3.5 w/o NaCl solution. Experiments were performed using the standard three electrode configuration in a cell driven by the equipment described above. A scan rate of 0.1 mV/sec was used in each experiment.

Corrosion Rate Measurements

Corrosion rate measurements were performed using a Tafel line extrapolation technique. Potentiodynamic polarization was used to generate the potential vs. log current density response over a range of 100 millivolts on either side of the corrosion potential. A curve fit was performed on the anodic and cathodic charge transfer regions to obtain Tafel line equations. The Tafel equations were solved simultaneously to obtain the corrosion current and the corrosion potential. The curve fits were considered acceptable if the corrosion potential obtained by solving the equations and the measured corrosion potential differed by no more than 5 mV.

This experiment was performed on the synthesized T_1 phase in aerated 3.5 w/o NaCl solutions whose pH was adjusted using HCl orNaOH. Six experiments were performed for solution pH values of 3, 4, 6, 8, 10 and 11.

Results

Open Circuit Measurements

Table 2 lists the open circuit potentials measured for T_1, 1100 Al and SHT 2090 in the three environments used in this study. The initial potential measured for T_1 specimens was typically 100 mV more active than the steady-state potential.

Potentiodynamic Polarization

All three materials were subjected to cyclic polarization but only plots for T_1 and 1100 Al in deaerated 3.5 w/o NaCl solution are presented here (figs. 1a and b). The scans were begun at point (A) on the diagram in the positive direction. Point (B) indicates the corrosion potential on the positive scan. The scan is continued to -0.5 V_{SCE} then reversed. Point (C) is the corrosion potential on the return scan.

Corrosion Rate Measurements

Figure 2 is a plot of T_1 corrosion rate (Log corrosion current density) vs. pH. Data for the corrosion rate of pure aluminum is also plotted in this figure for comparison (14).

DISCUSSION

The Role of T_1 in Subgrain Boundary Corrosion

Relative Corrosion Behavior. Table 3 lists the corrosion potentials and corrosion current densities for the three materials used to simulate the phases present in the subgrain boundary region. In deaerated solution the corrosion potentials of the 1100 Al and the T_1 are very nearly equal. However, a comparison of the corrosion current densities shows that the T_1 phase would corrode much more quickly than a copper depleted region along a subgrain boundary.

Subgrain Boundary Pitting. Figure 3a is an optical micrograph of a surface of a 2090 aged 14 hours at 162°C and subjected to

anodic polarization in 3.5 w/o NaCl solution. The surface is characterized by many small pits, most of which have formed along the subgrain boundaries. This type of attack is widely attributed to the selective dissolution of T_1 precipitates on the subgrain boundaries. The pH of this solution is typically in the range of 5 to 5.5 in this type of experiment. An examination of Figure 2 shows that in this pH range the corrosion rate of pure aluminum (a similar response for a α-Al matrix is observed) is near its minimum while the T_1 is dissolving at a rate of 0.1 mA/cm^2.

The second aspect of subgrain boundary attack discussed here concerns the pitting behavior of the subgrain boundary region and the subgrain interiors. It has been observed that subgrain boundary pitting increases as aging time increases. Pitting of the subgrain interiors, on the other hand, is minimal and largely insensitive to aging up to the peak aged condition (7,18). This behavior appears to be inconsistent with a selective T_1 dissolution mechanism since matrix precipitation of T_1 is known to occur; particularly in alloy products stretched prior to aging.

There are, however, two important differences between subgrain boundary and subgrain interior T_1 precipitation. First, along a given segment of subgrain boundary, only one T_1 variant is observed (19). That is that all the precipitates have the same orientation and the average plate spacing is quite small. In the subgrain interior, different variants can exist and the average plate spacing is greater. The second difference is that

T_1 precipitates on the boundary are generally larger than precipitates within the matrix (5). Based on these observations, the dissolution of a T_1 plate on the boundary is more likely to expose another T_1 plate than the dissolution of a matrix plate. As a result, subgrain boundary pitting is more sensitive to aging than matrix pitting up to the peak aged condition.

Continuous Subgrain Boundary Corrosion. In occluded environments like pits and crevices, the corroded subgrain boundary region exhibits a different type of morphology (fig. 3b). In this situation, the subgrain boundaries are continuously attacked in a fashion which is usually termed intergranular or interfragmentary corrosion (6,15). Pits and crevices in Al-Li-Cu alloys have solution pH values reported to be in the range of 3 to 4.5 when coupled to an aerated, chloride-containing bulk environment (16,17,18). When not coupled to a bulk environment an alkaline pit and crevice solutions develop. Reported pH values range from 9 to 11 in this situation (16,17,18). These regions are indicated in Figure 2. In these regions the corrosion rate of aluminum is increased compared to that observed at intermediate pH values.

The corrosion morphology and corrosion rate data suggest a two part process for this type of attack:

1.) T_1 precipitates on the subgrain boundaries dissolve

2.) The dissolution of the T_1 exposes α-Al subgrain faces whose corrosion rate is increased in the crevice solution generating the continuous subgrain boundary

corrosion.

Copper Dealloying

The dealloying of copper has been observed in Al-Cu-Mg and Al-Li-Cu precipitation hardened alloys (8,16,17,18). Copper enrichment around pits and crevices in Al-Cu-Mg and Al-Li-Cu alloys suggests that dissolved copper ions are physically transported through solution from the site of dissolution to a site favorable for their reduction (11,17,18). Copper deposits near a crevice or pit can accelerate localized corrosion by facilitating hydrogen reduction kinetics. Table 4 compares hydrogen reduction kinetics on copper and aluminum.

Visual examination of T_1 specimens after exposure to an aqueous environment showed, without exception, that the specimen surface was covered with a copper colored layer. However, X-ray microanalysis of exposed and unexposed T_1 surfaces could not conclusively distinguish copper enrichment due to the high copper content of the T_1 phase (25 a/o).

Data obtained in polarization experiments using T_1 supports a copper dealloying process of this phase. Figure 1a shows a polarization curve for 1100 Al in deaerated solution. In this experiment, the corrosion potential on the return scan is more negative than the corrosion potential on the positive scan. This type of response is expected since the surface is pitted during the scan through the transpassive region. On the return scan (the negative direction), more total current is passed at the

corrosion potential causing a shift in the active direction (C).

A different situation exists for a T_1 specimen subjected to the same type of experiment (Fig. 1b). In this case, corrosion occurring in the transpassive region causes the surface of the electrode to become enriched with copper by the dealloying process. On the return scan, the electrode has been ennobled by the copper and the exchange current density for the hydrogen reduction reaction has been increased. As a result the corrosion potential is shifted in the positive direction (C).

CONCLUSIONS

1.) Based on open circuit potential, potentiodynamic polarization and corrosion rate determinations, T_1 is an extremely active phase with a corrosion potential of -1100 mV_{SCE} and a corrosion current of 0.1 mA/cm^2 in 3.5 w/o NaCl solution.

2.) Corrosion rate data and corrosion morphology in the subgrain boundary region suggest that T_1 plays an important role in both subgrain boundary pitting and continuous subgrain boundary corrosion associated with occluded environments.

3.) Visual examination and polarization behavior support copper dealloying of the T_1 phase in Al-Li-Cu alloys

ACKNOWLEDGEMENTS

The authors wish to thank NASA, Langley Research Center, Hampton, VA for supporting this research. This research was performed under Grant No. NAG-1-745-2, D.L. Dicus, Contract Monitor. The authors also wish to thank the ALCOA Technical Center,

Pittsburgh, PA for supplying test material for this research. Last, thanks to J.P. Moran for many insightful discussions and suggestions concerning this work.

REFERENCES

(1) J.G. Rinker, M. Marek and T.H. Sanders, Jr., "Aluminum-Lithium Alloys II", TMS-AIME, Warrendale, PA, 1984, pp. 597-626.

(2) M. Ahmad,**Journal de Physique**, 9, 48, Sept. 1987, pp. C3-871-C3-879.

(3) E.I. Meletis, J.M. Sater and T.H. Sanders, Jr., "Aluminum Alloys: Their Physical and Mechanical Properties", Vol. II, EMAS, West Midlands, UK, 1986, pp. 1157-1175.

(4) E.L. Colvin , S.M. Murtha and R.K. Wyss, "Aluminum Alloys:Their Physical and Mechanical Properties", Vol. III, EMAS, West Midlands, UK, 1986, pp. 1853-1867.

(5) E.I. Meletis, **Mat. Sci. Engg.**, 93, 1987, pp. 235-245.

(6) R.C. Dorward and K.R. Hasse, **Corrosion**, 44, 12, 1988, pp. 932-941.

(7) C. Kumai, J. Kusinski, G. Thomas and T. M. Devine, Report prepared for USDOE under contract No. DE-AC03-76SF00098, March, 1987.

(8) I.L. Mueller and J.R. Galvele, **Corrosion Sci.**, 17, 1977, pp. 179-193.

(9) A. Garner and D. Tromans, **Corrosion**, 35, 2, 1979, pp. 55-60.

(10) K. Sugimoto, K. Hoshino, M. Kageyama and Y. Sawada, **Corrosion Sci.**, 15, 1975, pp. 709-720.

(11) K. Urushino and K. Sugimoto, **Corrosion Sci.**, 19, 1979, pp. 225-236.

(12) J.R. Galvele, S.M. de DeMicheli, I.L. Mueller, S.B. de Wexler and I.L. Alanis, "Localized Corrosion", NACE, Houston, TX, 1974, pp. 580-599.

(13) A.K. Hardy and J.M. Silcock, **J. Inst. Metals**, 84, 1955-56, p. 423.

(14) A. Ya. Chatalov in M. Pourbaix, "Atlas of Electrochemical Equilibria in Aqueous Solutions", NACE, Houston, TX, 1974, p. 173.

(15) Handbook Committee, "Metals Handbook, Vol. 13", ASM, Metals Park, OH, 1987, p. 590.

(16) N.J.H. Holroyd, , A. Gray, G.M. Scamans and R. Hermann, "Aluminum-Lithium Alloys III", Institute of Metals, London, 1986, pp. 310-320.

(17) J.G. Craig, R.C. Newman, M.R. Jarrett and N.J.H. Holroyd, **J. de Physique**, 9, 48, Sept., 1987, pp. C3-825-C3-833.

(18) R.G. Buchheit, J.P. Moran and G.E. Stoner, work in progress.

(19) M.H. Tosten, A.K. Vasudevan and P.R. Howell, "Aluminum-Lithium Alloys III", Institute of Metals, London, 1986, pp.490-495.

(20) G. Kortum and J. O'M. Bockris, "Textbook of Electrochemistry", Vol. II, Elsevier, Amsterdam, 1951.

(21) A. Theil and W. Hammerschmidt, **Z. Anorg. Allgem. Chem.**, 132, 1923, pp. 15-35.

TABLE 1 - X-ray Diffraction Data for Al_2CuLi

Reference (JCPDS #28-12)		Measured	
dA	I/I_1	dA	I/I_1
9.39	20		
4.69	100	4.66	83
4.31	30	4.29	24
3.90	30	3.90	12
3.15	30	3.16	5
2.53	20		
2.333	60	2.34	27
2.187	30	2.19	29
2.145	100	2.15	19
2.047	30	2.06	45
1.949	100	1.95	100
1.865	20		
1.70	10	1.71	5
1.62	10		
1.579	30	1.58	69
1.554	10		
1.53	10		
1.468	20	1.46	6
1.41	10		
1.367	30		
1.333	30	1.33	20
1.320	30		
1.300	10		
1.261	20		
1.240	30	1.24	6

Table 2 - Open Circuit Potentials (in mV_{SCE})

	Aerated	Deaerated	ASTM G69
1100 Al	-820	-1020	-840
SHT 2090	-730	-730	-740
Al_2CuLi	-1100	-1055	-815

TABLE 3 - Corrosion Potentials and Corrosion Currents for 1100 Al, SHT 2090 and T_1 (Al_2CuLi)*

	E_{CORR} (mV_{SCE})	i_{CORR} (A/cm^2)
1100 Al	-1020	3.3×10^{-7}
SHT 2090	-730	2.8×10^{-7}
T_1	-1055	8.0×10^{-5}

*in deaerated 3.5 w/o NaCl solution

TABLE 4 - Exchange Current Densities and Hydrogen Overpotentials for Aluminum and Copper* (20,21)

	i_o (A/cm^2)	η (V)
Aluminum	3.16×10^{-10}	very large
Copper	3.16×10^{-7}	0.19

* in 1 M H_2SO_4.

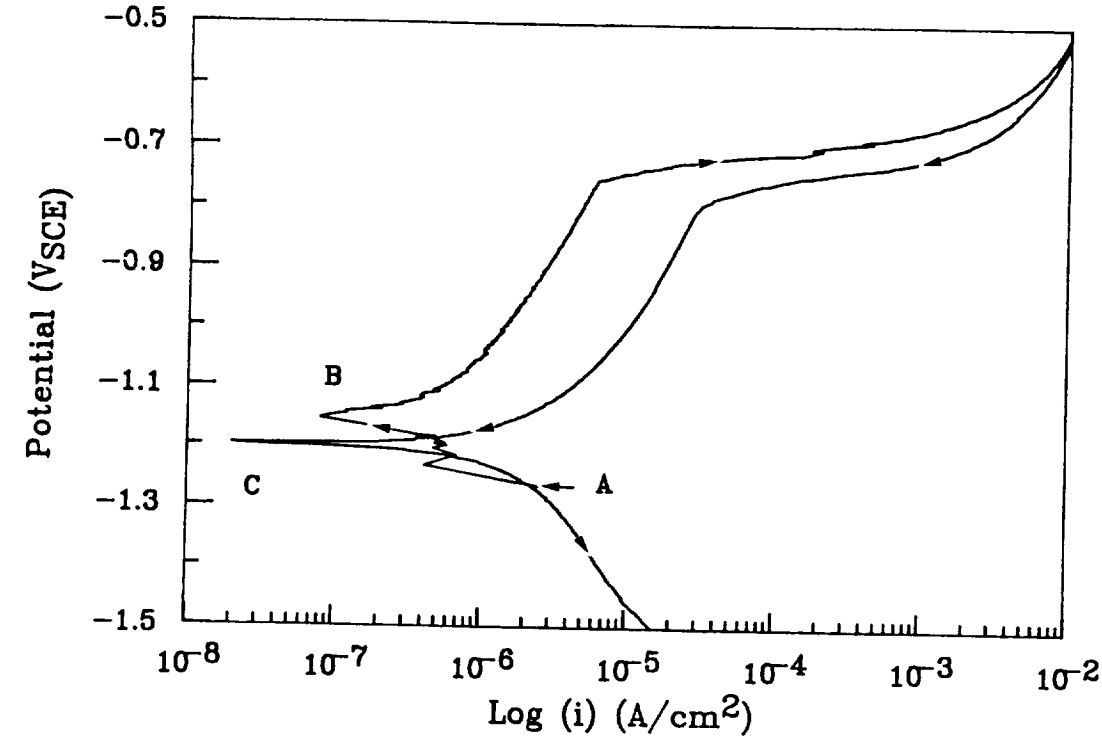

Figure 1 a. Polarization scan for 1100 Al in deaerated 3.5 w/o NaCl solution, scan rate = 0.1 mV/sec.

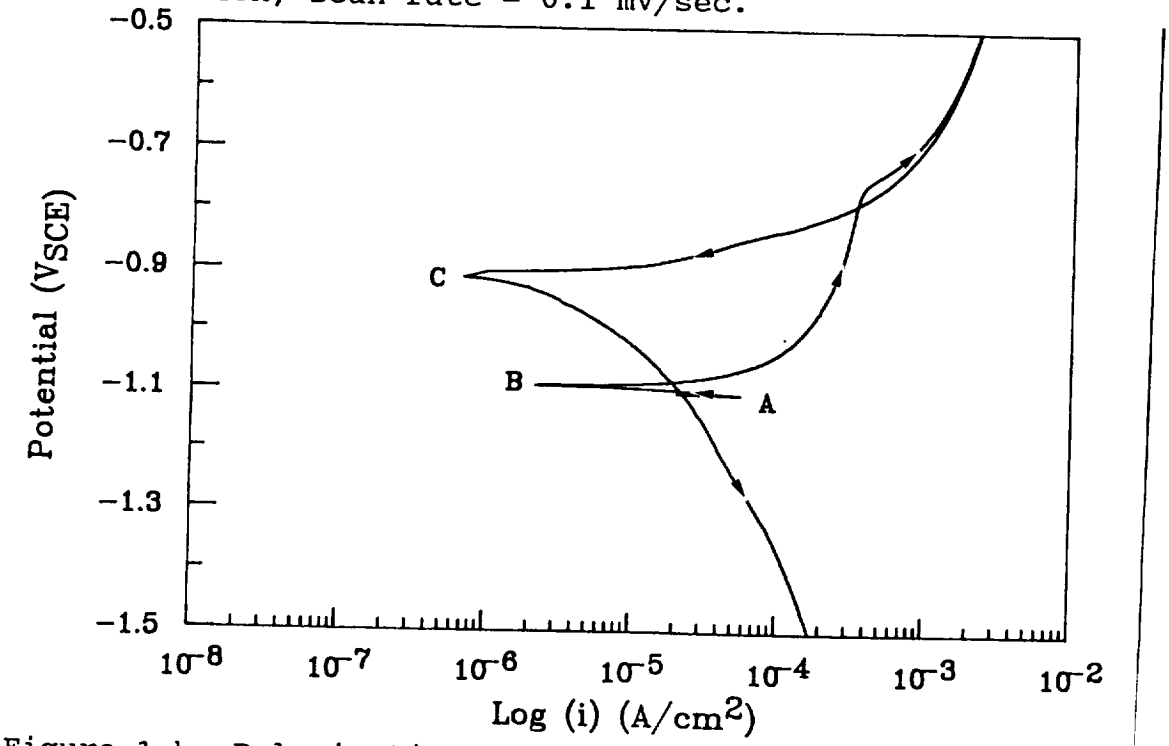

Figure 1 b. Polarization scan for synthesized T_1 in deaerated 3.5 w/o NaCl solution, scan rate = 0.1 mV/sec.

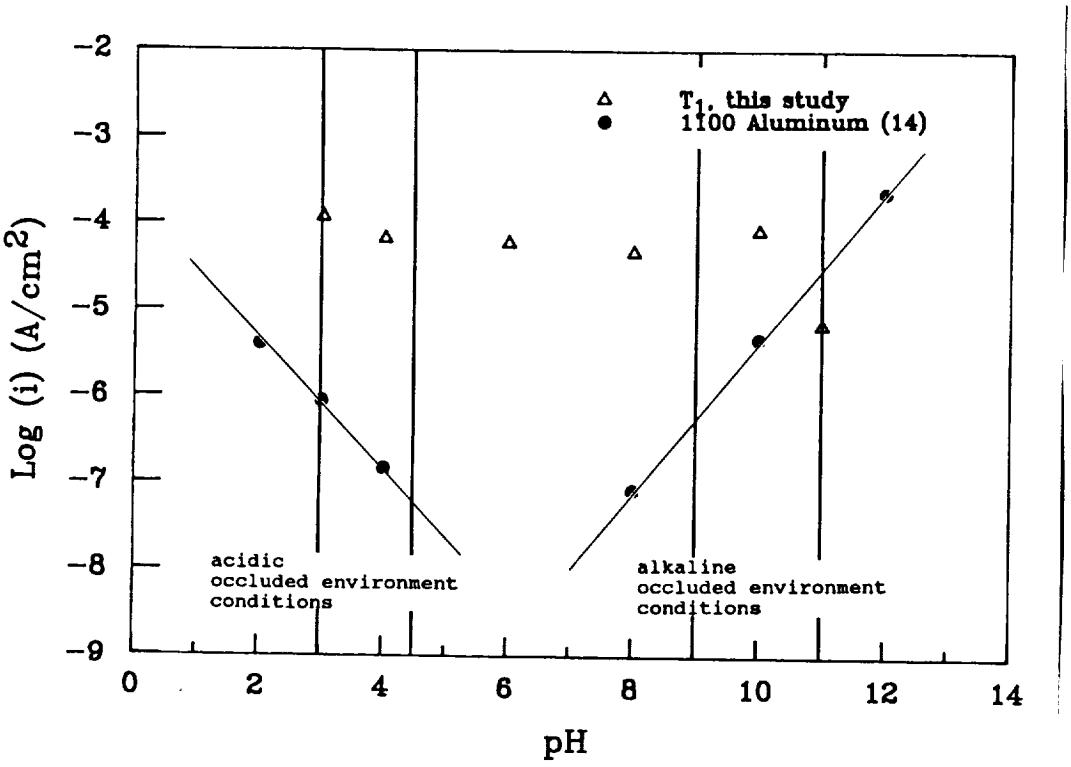

Figure 2. Plot of corrosion current versus pH for T_1 and 1100 aluminum.

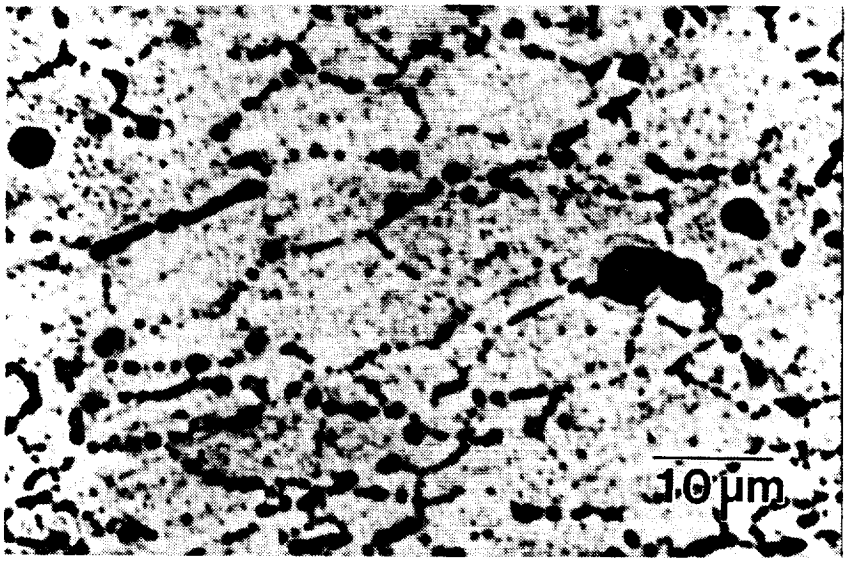

Figure 3 a. Optical micrograph of subgrain boundary pitting.

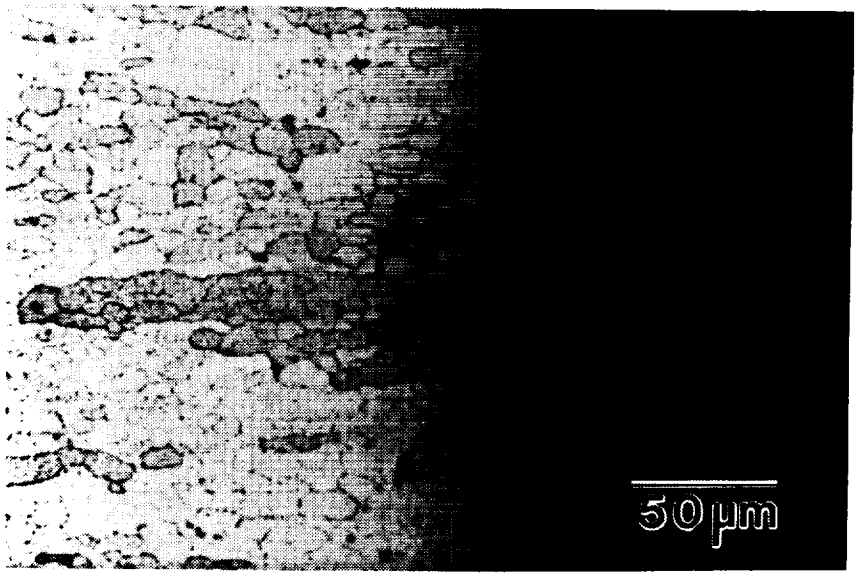

Figure 3 b. Optical micrograph of a large pit showing continuous subgrain boundary corrosion.

SOLUTION CHEMISTRY EFFECTS ON THE STRESS CORROSION CRACKING BEHAVIOR OF ALLOY 2090 (Al-Li-Cu) AND ALLOY 2024 (Al-Cu-Mg)

James P. Moran and Glenn E. Stoner

Center for Electrochemical Sciences and Engineering
Dept. of Materials Science, The University of Virginia
Charlottesville, VA 22901

(As submitted to The 5th Int'nl Al-Li Conference, March, 1989)

ABSTRACT

The stress corrosion cracking (SCC) initiation behavior of alloys 2090 and 2024 was investigated in various NaCl-based environments. SCC specimens immersed in NaCl did not fail after as long as 30 days. However, for specimens removed from NaCl after 6 days, exposure to lab air resulted in fracture within 24 hours, while exposure to a CO_2-FREE environment did not promote fracture. Constant immersion in NaCl/Li_2CO_3 accelerated SCC, while immersion in NaCl/Na_2CO_3 did not promote failure. In addition to SCC data, polarization experiments and simulated-crevice pH measurements were performed. Based on these data, a mechanism of passivation by precipitation of Li_2CO_3 is suggested to account for the changes in SCC behavior. The effects of bulk/local solution chemistries on SCC are shown to overshadow microstructural changes caused by aging.

INTRODUCTION

Aluminum-lithium-copper alloys have been observed to be susceptible to both localized corrosion and stress corrosion cracking (SCC) in chloride containing environments. Much of the available evidence suggests that the subgrain boundary phase T_1 plays a major role in the pitting and SCC behavior (1-5). A common factor in most of the proposed mechanisms is the dissolution of T_1.

The role of localized environments in the SCC performance of Al-Li alloys has also been investigated (6-8). Several investigators have shown that alternate immersion enhances SCC rates, relative to constant immersion, for 8090 (6,7) and 2090 (8). Alloy 8090 was found to be immune to SCC when

constantly immersed in NaCl solutions, but can fail rapidly when removed from solution and exposed to lab air (7). Removal into a CO_2-FREE environment, however, did not promote failure. Under constant immersion, the occluded environment is considered too aggressive, thereby promoting general attack within the fissures. The need for CO_2 is attributed to its role in the carbonation and acidification of alkaline fissures, eventually producing passivation by precipitation of $LiAlO_2$, creating a critical active/passive balance, necessary for SCC. Constant immersion of 8090 in NaCl with Li_2CO_3 additions promoted accelerated SCC, with a similar active/passive balance being the suggested mechanism (7).

In the present work, the pre-exposure and bulk/local solution chemistry effects discovered by Holroyd et al. (6,7) on 8090-type alloys have been investigated for alloy 2090. Emphasis is on the effect of bulk solution chemistries and atmospheric CO_2 on the occluded cell environment, and the role of the occluded environment in the crack initiation and early-stage propagation processes.

EXPERIMENTAL PROCEDURE

Material

Both alloys were commercially prepared 38 mm ingot-cast plates. The 2090 plate was supplied by The ALCOA Technical Center, Pittsburgh, PA. It was solution heat treated and subjected to a 6% deformation prior to shipping. The 2024 plate was purchased in a T-351 temper. Aging times and temperatures, along with average mechanical properties are given in TABLE 1.

TABLE 1 - Summary of aging times and mechanical properties.

Alloy	Temper	Aging Temp. (°C)	Aging Time (hours)	YS (MPa)	UTS (MPa)	Plastic Strain (%)
2090	UA*	160	4	385	530	4.0
2090	PA	160	13	440	490	1.0
2024	UA	190	3	470	500	4.0

* UA = Under-aged, PA = Peak-aged

SCC Testing

All SCC experiments were of the Time-to-Failure (TTF) type. Smooth tensile bars (gage length = 3 mm dia x 20 mm) were machined such that the stress would be applied in the short transverse direction. Specimens were stressed, using ASTM G-49 stressing frames, to an arbitrarily chosen value of 240 MPa (55-65% of yield strength). The combination of poor fracture toughness (9), low ductility and small tensile bar diameter should produce fast fracture of 2090 specimens after a relatively limited amount of sustained crack growth. Therefore, times-to-failure should provide a reasonably accurate measure of crack initiation times. Reported TTF's represent the average of 5-8 specimens.

Constant immersion experiments. Test solutions were naturally aerated 3.5 w/o NaCl in distilled water, with individual additions of selected species (see TABLE 3). All solutions were buffered with dilute HCl or NaOH to pH=10. Stressed specimens were then immersed in these environments until failure.

Pre-exposure experiments. Stressed specimens were immersed in 3.5 w/o NaCl (bulk pH $\simeq$ 6) for a period of six days. Upon removal from the solution, the specimens were lightly rinsed with distilled water, followed by exposure to laboratory air or exposure to a CO_2-free environment (an enclosed container of super-saturated NaOH solution).

Potentiodynamic Polarization Scans

Potentiodynamic polarizations were performed on both alloys using the standard three-electrode configuration (SCE reference, Pt counter) in a cell driven by a PAR 273/351 automated corrosion measurement system. After immersing a specimen in solution and allowing a steady-state corrosion potential to develop (typically 4-6 hours), a polarization scan was performed, starting at the corrosion potential, and scanning in the electro-positive direction at a rate of 0.2 mV/sec. Triplicate tests were conducted in all solutions used for constant immersion SCC tests.

Simulated Crevice Experiments

A cylindrical bore 2.5 mm in diameter and 10 mm in depth was machined into blocks of alloy measuring 1 x 1 x 1.5 cm. The barrel of a pH microelectrode (≈ 2.45 mm diameter) was inserted into the bore to form a crevice. Alloy 2090 was subjected to all SCC test environments, including a pre-exposure simulation (after immersion in NaCl, the bulk environment was removed, thus isolating the crevice). Alloy 2024 was subjected only to NaCl and pre-exposure simulation. Two to three specimens were subjected to each environment, with good experimental agreement.

RESULTS

SCC Results

Pre-exposure experiments. After a six-day pre-exposure in NaCl, the surfaces of the pre-exposed specimens were decorated with numerous, relatively large pits, as illustrated in Fig. 1a. Upon removal from solution, 2090 exposed to lab air exhibited failure times of roughly 12 hours. Fig. 1b illustrates a sharp crack growing from one of the blunted surface pits. Exposure to a CO_2-FREE environment, however, did not produce fracture after more than 60 days. This is in good agreement with earlier work on alloy 8090 (6,7).

Alloy 2024 did not fail in normal lab air; however, exposure to lab air of near 100% relative humidity (R.H.) did produce fracture after 4-6 days. Surface pits similar to those observed on 2090 decorated the surface of the 2024 tensile bars.

Constant immersion experiments. TABLE 3 summarizes the TTF data for the various test environments. For alloy 2090, no failures were observed in NaCl or NaCl/Na_2CO_3 solutions. Surface attack and pitting occurred in both of these environments, with NaCl/Na_2CO_3 being the more severe of the two. Immersion in NaCl/ Li_2CO_3, however, promoted rapid failure (1-2 days). Examination of the tensile bar surface revealed that only extremely limited pitting had occurred, relative to the other environments. This remained true even for specimens left immersed, after fracture, for 30 days. Immersion in NaCl/LiCl solution produced only moderate increases in failure rates (10-15 days), and resulted in tensile bar surfaces similar to those in NaCl (e.g., Fig. 1a).

TABLE 2 - Times to Failure (days) After NaCl Immersion For 6 Days.

ENVIRONMENT	Alloy 2024	Alloy 2090UA
Lab Air (≈ 50% R.H.)	> 60*	0.6±0.1**
Lab Air (≈ 100% R.H.)	5±1	---
CO_2-Free Air (≈ 100% R.H.)	> 60	> 60

TABLE 3 - Times to Failure (days) Under Constant Immersion.

ADDED SPECIES***	Alloy 2024	Alloy 2090UA	Alloy 2090PA
None	> 60	> 30	> 30
LiCl	> 60	16.0±3.0**	10.7±2.7
Li_2CO_3	5.7±1.5	1.0±0.3	1.70±.1
Na_2CO_3	> 60	> 60	> 60

TABLE 4- Polarization Data for Alloy 2090, Peak-Aged.

ADDED SPECIES***	E_{corr} (mV vs. SCE)	i_{pass} ($\mu A/cm^2$)	E_{br} (mV vs. SCE)
None	-735±13**	---	-725±7
LiCl	-735±6	---	-735±6
Li_2CO_3	-737±5	0.75	-600±21
Na_2CO_3	-1210±10	56	-370±13

Footnotes to Tables 2-4:

* "> X" = Test ended after X days, with no failures.

** Mean ± Standard Deviation.

*** All environments have aerated 3.5 w/o NaCl as their base, with 0.1 M of the listed species added. The exception is LiCl, where 0.2M LiCl was added to 2.6 w/o NaCl, in an effort to keep Cl^- and Li^+ concentrations consistent with Li_2CO_3. All initial pH = 10. Chemicals were all reagent grade.

In those environments that did promote failure, there appears to be some effect of aging time. For $NaCl/Li_2CO_3$, peak-aged specimens failed in roughly twice the time as under-aged, on average. The opposite effect was observed for NaCl/LiCl, with the under-aged temper TTF's being slightly longer than peak-aged.

The constant immersion data for alloy 2024 exhibit trends similar to those of alloy 2090, with two exceptions : no failures were observed in NaCl/LiCl, and failure times in $NaCl/Li_2CO_3$ were ≈ 2-3 times longer than 2090. Tensile bar surface conditions were similar to those of 2090 specimens.

Polarization Data

TABLE 4 summarizes the anodic polarization behavior for alloy 2090 peak-aged. The corrosion potential (Ecorr) was independent of environment, with the exception of $NaCl/Na_2CO_3$, where a 400 mV decrease was measured. No passive current was measured in NaCl or NaCl/LiCl, indicating that 2090 is above its pitting potential in these environments. A passive region was observed, however, in $NaCl/Li_2CO_3$ for approximately 135 mV. These values are consistent with the appearance of the tensile specimen surfaces; pitting was readily observed in NaCl and NaCl/LiCl, but not in $NaCl/Li_2CO_3$. Exposure in $NaCl/Na_2CO_3$ promoted a large "pseudo-passive" region. The term "pseudo-passive" is chosen here because, although the region is indeed potential-independent, the current density is still relatively large. Although the breakaway potential is unusually high, the large current density and associated active corrosion potential result in this being a severely corrosive environment. These data are consistent with a recent study of the polarization behavior of alloy 6061 in [alkali metal]-carbonate solutions, although the addition of chloride appears to have magnified the differences of Li^+ vs. Na^+ (10).

Simulated Crevice Measurements

Figure 2 illustrates the occluded cell pH response for alloy 2090 peak-aged. The highly buffered carbonate solutions remain at pH=10. The NaCl and NaCl/LiCl environments, however, exhibit a rapid decline initially, followed by a gradual decline to pH≈4. For an initial solution pH of 6, a slight increase is observed early, followed by gradual decline to pH≈4. The pH response for simulated pre-exposure conditions is displayed in Figure 3. A

gradual increasing trend is observed for both 2090 and 2024.

DISCUSSION

Role of CO_2 in the SCC Process

Perhaps the most significant result of this work is the effect of atmospheric CO_2 on the SCC behavior of pre-exposed specimens. With this in mind, the following discussion will propose a series of critical events occurring during the pre-exposure process, with emphasis on the role of CO_2 in the formation of a SC crack. Supporting experimental evidence will be included where appropriate.

Upon immersion in NaCl, intergranular fissures initiate at surface flaws and propagate inter-subgranularly. In the presence of a bulk solution, oxygen reduction on the external surfaces will be the primary cathodic reaction. Therefore, cathodic consumption of H^+ within the fissure will be minimal, and the occluded pH should be governed by the following Al(III) hydrolysis equilibria (see Fig. 4) (11,12) :

$$Al^{3+} + H_2O = AlOH^{2+} + H^+ \qquad pK_{11} = 4.97 \qquad (1)$$

$$Al^{3+} + 2H_2O = Al(OH)_2^+ + 2H^+ \qquad pK_{12} = 9.9 \qquad (2)$$

$$Al^{3+} + 3H_2O = Al(OH)_3 + 3H^+ \qquad pK_{13} = 15.6 \qquad (3)$$

These equilibria predict a steady-state pH≈4, as measured (Fig. 2). The rate of metal dissolution should continue to increase as the pH decreases, thereby inhibiting the formation of a sharp crack tip.

Removal of the bulk solution forces the cathodic reaction (hydrogen evolution) to occur within the fissures. The consumption of H^+ gradually increases the fissure pH, as measured (Fig. 3). As pH increases, the solubility of Al (III) decreases (Fig. 4), most likely promoting precipitation of $Al(OH)_3$. As the pH rises above 7, the equilibrium pH should be governed be Eq. 3 and:

$$Al^{3+} + 4H_2O = Al(OH)_4^- + 4H^+ \qquad pK_{14} = 23 \qquad (4)$$

In the presence of Li^+ the insoluble (13) $LiAlO_2$ should precipitate (AlO_2^- is equivalent to $Al(OH)_4^- \ 2H_2O$).

Although the above series of events predicts precipitation of at least two species, it is unlikely that these species play a major role in the passivation of fissures, since their precipitation will occur with or without the presence of atmospheric CO_2. On the other hand, atmospheric CO_2 <u>will</u> directly effect the concentrations of dissolved CO_2 and its ionic species, which are governed by the following equilibria (14,15) and Henry's Law (15) (see Fig. 5):

$$CO_2\ (g) = CO_2\ (aq) \qquad pK_{aq} = 4.97 \qquad (5)$$

$$CO_2\ (aq) + H_2O = HCO_3^- + H^+ \qquad pK_1 = 5.75 \qquad (6)$$

$$HCO_3^- + H_2O = CO_3^{2-} + H^+ \qquad pK_0 = 9.10 \qquad (7)$$

As the pH increases (due to hydrogen evolution), these equations predict the percentage of CO_2 in its ionic forms will increase. This is where the presence of atmospheric CO_2 becomes critical. Figure 6 predicts the total concentrations of dissolved CO_2 species with and without exposure to atmospheric CO_2 (i.e. saturated and unsaturated, respectively). From these calculations, it is evident that as the alkalinity of a fissure increases, the concentrations of bicarbonate and carbonate will be orders of magnitude greater in the presence of atmospheric CO_2.

Given the fact that atmospheric CO_2 will significantly increase the carbonate/bicarbonate concentration within fissures, the next issue to be addressed is the role of this increased concentration in the SC initiation process. The evidence suggests a mechanism of fissure passivation by precipitation of Li_2CO_3. Upon removal of the bulk solution, continued metal dissolution should increase the local Li^+ concentration ($[Li^+]$), and exposure to CO_2 will increase $[CO_3^{2-}]$. Given the low solubility of Li_2CO_3 ($.pK_p$=2.74) (13), it is likely that precipitation of Li_2CO_3 could occur, and its passivating nature has been documented in this and earlier work (10).

As an example, consider a local pH of 10. Without CO_2, precipitation is predicted at $[Li^+]$ = 13 Molar; however, exposure to CO_2 would allow precipita-

tion at $[Li^+]$ = 0.1 Molar. Unfortunately, this lithium concentration is roughly 50 times higher than measured values for 8090 crevices (6), and a high pH is not achieved (Fig. 3). Nevertheless, it is likely that the local pH and lithium concentration at the base of a fissure could be greater than the measured averages, thus exceeding the local solubility. In addition, the high total ionic concentration will tend to decrease the solubility (13,14).

The constant immersion data is consistent with this argument. Exposure to NaCl/LiCl did not promote failure. NaCl/Na_2CO_3 also did not promote failure, and the solubility for Na_2CO_3 is 2-3 orders of magnitude higher than Li_2CO_3 (13). Neither lithium alone nor carbonate (and its buffered pH) alone was a sufficient requisite for the passivity of fissures.

A similar argument can be made for alloy 2024, with passivation now occurring by precipitation of Mg_2CO_3 (pK_{sp} = 4.59) (13). The fact that 2024 did not break in lab air could be due to evaporation prior to achieving a critical crack length. Cracking was achieved under 100% R.H., but again only in the presence of atmospheric CO_2.

Effects of Aging

The trend of improved SCC resistance with increased aging observed for NaCl/Li_2CO_3 is consistent with the literature (1,2,6). The opposite trend, however, is displayed for NaCl/LiCl. Clearly, more work is needed to better define the effects of aging, and further experiments are planned and underway. Nevertheless, one observation is already clear - namely that the changes in SCC performance due to aging are quite small, relative to the effects of the bulk and local environments.

CONCLUSIONS

1) Constant immersion in NaCl does not promote SCC in alloy 2090 or alloy 2024. Upon removal from NaCl, however, SCC is quickly facilitated, but ONLY in the presence of atmospheric CO_2.

2) The need for CO_2 is attributed to an increase in carbonate concentrations, eventually allowing passivation of blunted fissures by precipitation of Li_2CO_3.

3) Although further work is needed to determine with confidence the effects of aging on SCC performance of 2090, it is quite clear that any effects due to aging are small in magnitude, relative to the effects of subtle changes to the bulk/local solution chemistries.

ACKNOWLEDGEMENTS

This research was sponsored by a fellowship from ALCOA, E.L. Colvin and S.C. Byrne program monitors. Additional support was provided by a grant from The NASA, Langley Research Center (Grant No. NAG-145-2), D.L. Dicus, contract monitor. Special thanks are extended to R.G. Buchheit, our colleague at UVA. His input and interaction in this research has been a most valuable resource.

REFERENCES

(1) J.G. Rinker, M. Marek and T.H. Sanders, Jr., "Al-Li Alloys II", TMS-AIME, Warrendale, PA, 1984, pp. 597-626.

(2) E.L. Colvin, S.M. Murtha and R.K. Wyss, "Al Alloys:Their Physical & Mechanical Properties",EMAS, West Midlands, UK, 1986, pp. 1853-1867.

(3) C. Kumai, J. Kusinski, G. Thomas and T.M. Devine, Report prepared for USDOE, contract No. DE-AC03-76SF00098, March, 1987.

(4) R.G. Bucheitt, Jr., J.P. Moran and G.E. Stoner, work submited for review to Corrosion, March, 1989.

(5) R. Dorward and K. Hasse, Corrosion, 44, 1988, pp. 932-941.

(6) H.J.H. Holroyd, A. Gray, G.M. Scamans and R. Hermann, "Al-Li Alloys III", Inst. of Metals, London, 1986, pp. 310-320.

(7) J.G. Craig, R.C. Newman, M.R. Jarret and N.J.H. Holroyd, J. de Physique, 48, 1987, pp. C3-825 - C3-833.

(8) P.P. Pizzo, In Ref. 2, pp. 627-656.

(9) A.K. Vasudevan, P.R. Ziman, S.C. Jha and T.H. Sanders, Jr.,

In Ref. 7, pp. 303-309.

(10) J. Gui and T.M. Devine, Scripta Met., 21, 1987, pp. 853-857.

(11) C.F. Baes and R.E. Mesmer, The Hydrolysis of Cations, R.F. Krieger Publ., Malabar FL, 1986 pp. 112-123.

(12) N.J.H. Holroyd, G.M. Scamans and R. Hermann, Corrosion Chemistry Within Pits, Crevices and Cracks, A. Turnbull ed., HMSO, London, 1987, pp. 495-511.

(13) Lange's Handbook of Chemistry, J.A. Dean, ed. McGraw-Hill.

(14) T.L. Brown and H.E. LeMay, Chemistry - The Central Science, Prentice-Hall, 1977, pp. 501-504 and pp. 524-525.

(15) G. Barrow, General Chemistry, Wadsworth, Benton, CA, 1972.

Figure 1. Micrographs illustrating the pitting behavior of tensile bars subjected to the pre-exposure test: (a) pits along surface of specimen; (b) optical cross-section illustrating a crack initiating from a blunted fissure.

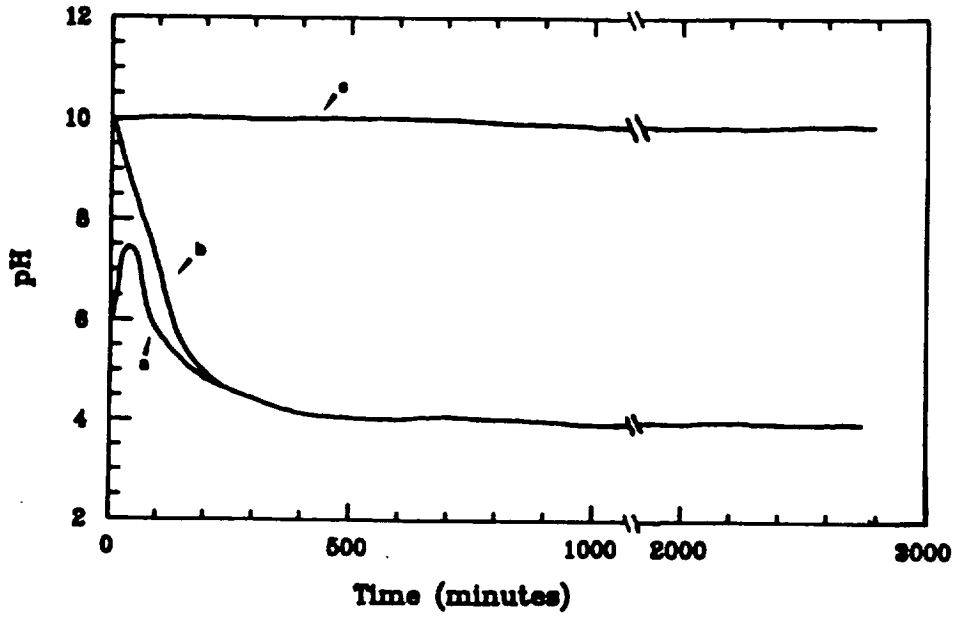

Figure 2. Simulated crevice pH vs. time data representative of alloy 2090 in the following environments : (a) NaCl, pH-6 ; (b) LiCl/NaCl or straight NaCl, pH-10 ; (c) Li_2CO_3/NaCl or Na_2CO_3/NaCl, pH-10. Curve (a) is also representative of alloy 2024 in NaCl, pH-7.

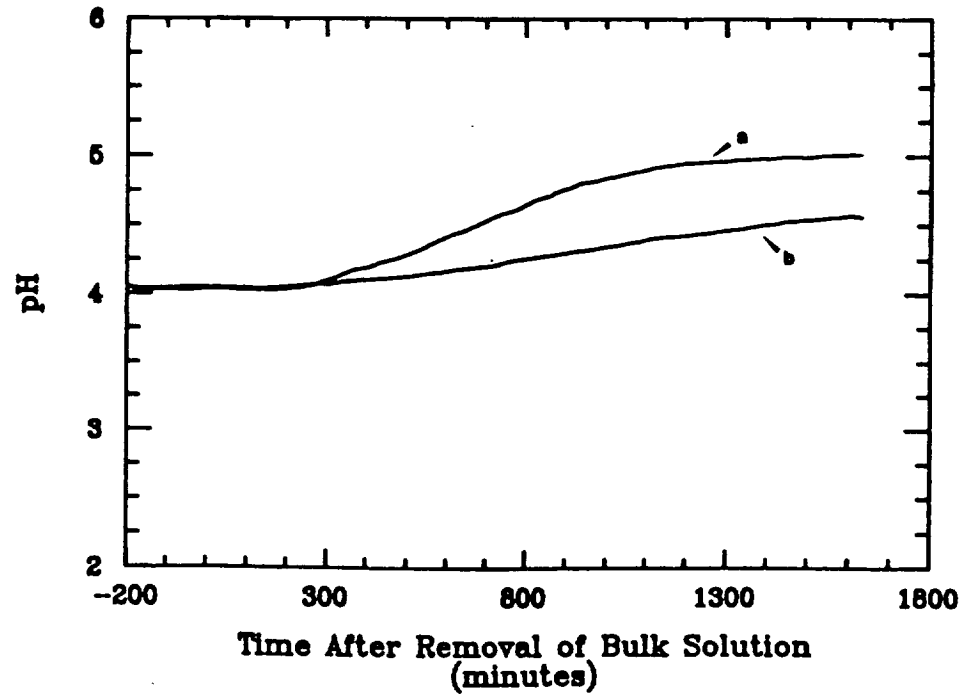

Figure 3. Simulated crevice pH vs. time data, illustrating the effect of removing the bulk environment (NaCl, pH-6) on the occluded cell pH : (a) alloy 2090 ; (b) alloy 2024.

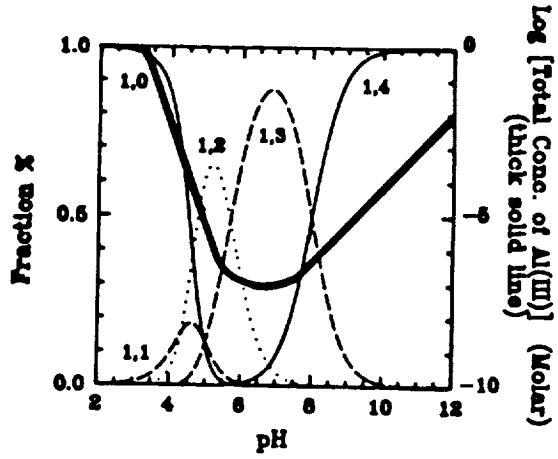

Figure 4. Stability diagram illustrating the distribution of mononuclear Al(III) hydrolysis products $Al_x(OH)_y^{(3x-y)+}$. The thick line is the total solubility of Al(III) (12).

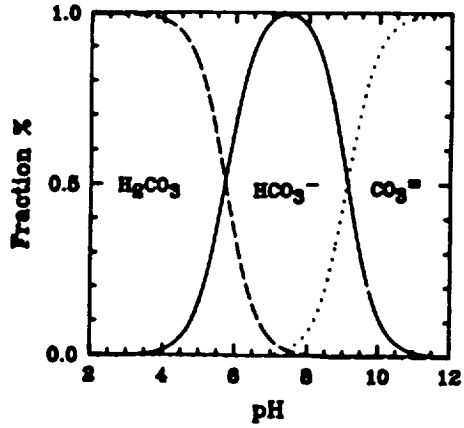

Figure 5. Stability diagram illustrating the distribution of species derived from dissolved CO_2 in seawater (15). (H_2CO_3 is equivalent to CO_2).

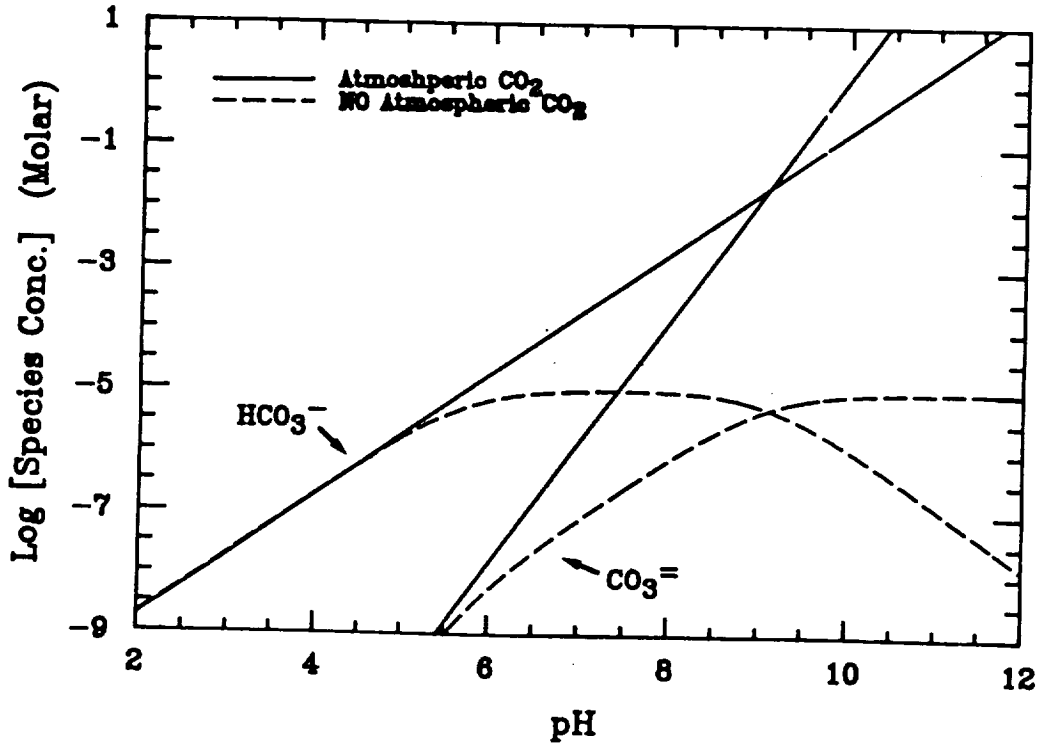

Figure 6. The calculated equilibrium concentrations of the dissociated ions of dissolved CO_2 in seawater, with and without exposure to atmospheric CO_2 (saturated and unsaturated respectively).

INFLUENCE OF DISSOLVED HYDROGEN ON ALUMINUM-LITHIUM ALLOY FRACTURE BEHAVIOR

F.C. Rivet* and R.E. Swanson*

The objective of this work is to study the effects of dissolved hydrogen on the mechanical properties of 2090 and 2219 alloys. Prior to mechanical testing, potentiostatic and potentiodynamic tests were performed using NaCl / HCl solutions varying in pH from 1.5 to 7.5 (3.5% NaCl in deionized water). After analysis of the potentiodynamic curve for each solution, several potentiostatic experiments were conducted for various times (from 10 minutes to several hours) with a cathodic overpotential of 300 mV. These experiments were performed to select charging conditions. The Charpy tests are part of our study designed to investigate the effects of temperature, notch orientation, and notch root radius on fracture behavior. In the present study of notch orientation, it has been shown that the fracture of L-S and T-S orientations proceeds via slipping of layers in the S-T direction. The T-S and L-S orientations fractured with substantially higher propagation energy than the L-T and T-L orientations, due in large part to the extensive delamination propagation of the fracture.

INTRODUCTION

By comparison with traditional aluminum alloys, the aluminum-lithium alloys show many advantages. By adding one weight percent lithium, the density is reduced by three percent and the elastic modulus is increased by six percent. However, the precipitation of the ordered δ' phase (Al_3Li) produces lower ductility and fracture toughness. Mechanical properties of these new alloys have been the subject of numerous studies, but corrosion behavior and, in particular, hydrogen embrittlement require additional study.

Lithium is a very reactive element; its addition is unfavorable in corrosion resistance. The precipitation of the δ phase (AlLi) on the grain boundaries decreases the stress corrosion cracking resistance (1,2). It is also known that lithium increases the sensitivity to localized corrosion and in particular pitting corrosion (3). Furthermore, hydrogen embrittlement tends to be increased by the addition of lithium due to reaction with hydrogen.

* Department of Materials Engineering
Virginia Polytechnic Institute and State University

EXPERIMENTAL PROCEDURE

The 2090 alloy had a pancake-shaped grain structure, with average grain size of about 1.2 mm by .7 mm by .15 mm. Specimens of 2090 have been sectioned and mounted in a red bakelite powder. Holes were drilled to allow for an electrical lead to be attached the 2090 specimen. The samples were polished successively using 320, 400, 600 grit paper and finished using diamond paste down to 1μm. The potentiostatic and potentiodynamic tests were performed on an EG&G Model 342 test system.

Charpy samples have been cut with a size of 55x10x10 mm. Then, for the four orientations L-T, T-L, L-S, and T-S show in Figure 1, a notch of 2 mm depth has been cut with a notch root radius of .25 mm. The samples were heated in an air furnace to various temperatures prior to testing. The impact test system, a GRC Model 730-I, is instrumented with a data acquisition and analysis system running on an IBM-PC. This system provides the capability of separating the total impact energy into initiation and propagation components (4).

HYDROGEN CHARGING STUDIES

In this study, test specimens were cathodically charged using the guidelines proposed by Dull and Raymond (5). Several experiments have been conducted to determine the best conditions to create hydrogen embrittlement without causing macroscopic surface damage. At this time, the tests have been carried out for various values of pH, regulated by the addition of HCl in a solution of dionized water containing 3.5 wt% NaCl. Initially, some potentiostatic and potentiodynamic tests have been conducted on 2090 alloys.

The potentiodynamic tests give us the value of Ecorr for the different solutions used. Then, we have been able to find a relation between the pH and the value of Ecorr, as shown by equation (1) below.

$$Ecorr(mV/SCE) = -540 - 77.7\ pH \qquad (1)$$

This equation can be compared with the one found by Schnuriger et al (6) to determine the pit generation potential (Ep) as a function of chloride ion concentration:

$$Ep(mV/SCE) = -740 - 64 \log [Cl^-] \qquad (2)$$

In tests conducted with pH values near 7 (the solution contained no HCl), two corrosion potentials were detected. A typical curve is shown in Figure 2. This kind of phenomenon has been previously described by Moran et al (7). We hypothesize that this represents a change in the surface layer. This effect will be further investigated.

Several potentiostatic tests have been performed in order to see whether pitting corrosion occurs. Our results show that solutions with a pH under 2.5 are too aggressive for this alloy. On the other hand, with the two

equations described above, we can calculate a potential which will provide hydrogen evolution, yet minimize the risk of pitting.

Microhardness tests have been performed in order to determine the time needed to charge the samples in hydrogen, but no reproducible results had been found. The chloride ions in solution, due to the addition of salt or HCl, seem to generate, even with precaution, some pitting corrosion on the surface of our samples. The chloride ions in solution apparently have a catalytic effect on the surface and increase the rate of pitting corrosion. Consequently, the next solution to be evaluated will be H_2SO_4 acid in water without any chloride ions.

EFFECT OF ORIENTATION ON CHARPY IMPACT ENERGY

In parallel with the electrochemical experiments, some Charpy impact tests have been performed in order to evaluate the effect of notch orientation. Four of the six orientations have been tested, namely, T-S, T-L, L-S, and L-T (Figure 1), for two temperatures: 25°C (70°F) and 200°C (392°F).

The results presented in Figure 3(a) show that the energy for crack initiation is virtually the same for the T-S, T-L, and L-T orientations while the L-S orientation show a greater resistance to crack initiation at 25°C, it has a somewhat lower resistance than the other orientations at 200°C. Figure 3(b) show that the propagation energy of the L-S orientation is much greater than the other orientations, with the T-S orientation having a somewhat greater resistance than T-L or L-T. The total impact energy curves are shown in Figure 3(c), with the same ranking as shown for propagation. The L-S samples did not completely break as shown schematically in Figure 4. The failure mode for the T-S orientation was similar to that of the L-S samples, but total separation occurred. Fracture in both the L-S and T-S orientations proceeded by ductile intergranular separation along the short tranverse plane of the pancake-shaped grains.

Tests have been carried out for the T-L and L-T orientations for additional temperatures, 25°C, 200°C, 300°C, 350°C, 400°C and 500°C. Figure 5 shows a dramatic increase in total impact energy at about 350°C. We are currently conducting tests at low temperatures (from -200°C to 0°C).

SUMMARY

- For these charging solutions, chloride ions produce substantial pitting corrosion in of 2090.

- For each orientation, the Charpy impact initiation energy is nearly the same. But due to the slipping of different layers, the L-S and T-S orientations have much higher propagation energy than the T-L and L-T orientations.

- Because of the pancake-shape grains, the T-S and L-S orientations showed substantial tearing, with corresponding high propagation energy. The T-L and L-T orientations will be used for further impact studies.

ACKNOWLEDGMENT

This work was performed under the sponsorship of the NASA Langley Research center. The authors are also grateful to Dennis Dicus,contract monitor for this study.

REFERENCES

1. T.H. Sanders Jr, P.W. Niskanen, Res. Mechanica Letters, 1 1981, p. 370.

2. P. Niskanen, T.H. Sanders Jr., J.G. Rinker, H. Marek, Corrosion Science, vol 22, 4 1982, p. 283.

3. R.E. Ricker, D.J. Duquette, Proceedings of the 2nd Al-Li Conference, Ed. T.H. Sanders Jr and E.A. Starke Jr (eds.), The Metallurgical Society of AIME, Warrendale, 1983, p. 581.

4. H.J. Saxton, A.T. Jones, A.J. West, and T.C. Mamaros, "Instrumented Impact Testing", T.S. DeSisto (ed.), STP 563, ASTM, Philadelphia, June 1973, pp. 30-49.

5. D.L. Dull and Louis Raymond, "Hydrogen Embrittlement Testing", Louis Raymond (ed.), STP 547, ASTM, Philadelphia, 1972, p. 21

6. S. Schnuriger, G. Mankowski, Y. Roque, G. Chatainier and F. Dabosi, "Statistical Study of the Pitting Corrosion of the 8090 Aluminum-Lithium Alloy", 4th International Aluminum-Lithium Conferences, G. Champier, B. Dubost, D. Miannay, L. Sabetay (eds.), Les Editions de Physique, Sept 1987, p. c3-853.

7. J.P. Moran, E.A. Starke, Jr., G.E. Stoner, G.L. Cahen, "The Influence of the Composition and Microstructure on the Corrosion Behavior of Two AlLiX Alloys", J. Corrosion, National Association of Corrosion Engineers, Vol. 43, No. 6, June 1987, p. 374

8. R.W. Hertzberg, "Deformation and Fracture Mechanics of Engineering Materials", John Wiley & Sons, 1976, p334.

	Li	Ge	Cu	Zr	Mn	Ti	V	Al
2090	2.40	0.27	1.60	0.13	--	--	--	Bal
2219	--	--	6.30	0.18	0.30	0.06	0.10	Bal

Table 1: Composition of each material.

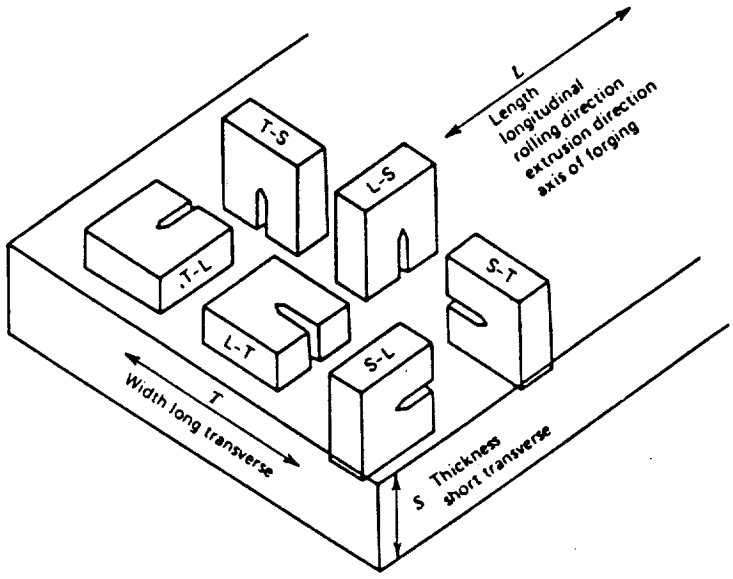

Figure 1: Labelling scheme for specimen orientation (8)

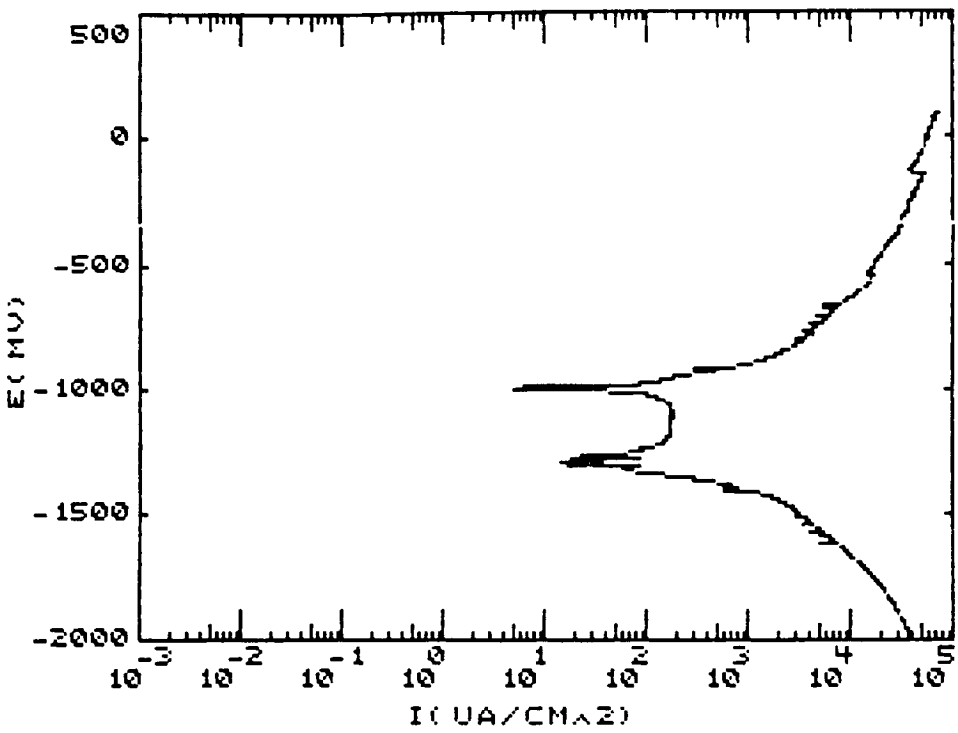

Figure 2: Potentiodynamic curve for a 2090 alloy in a 3.5% NaCl-deionized water solution: Double E_{corr}.

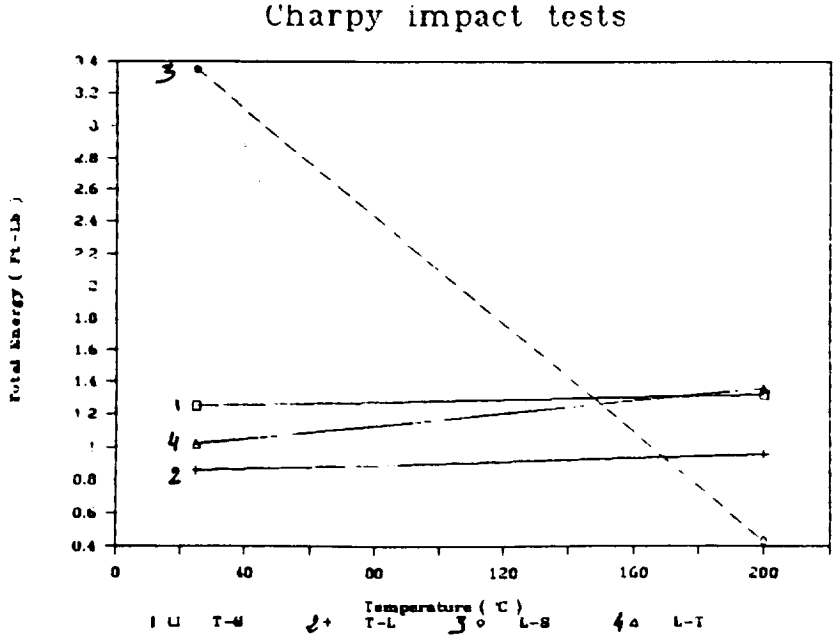

Figure 3(a): Effect of the orientation of the notch on the initiation energy.

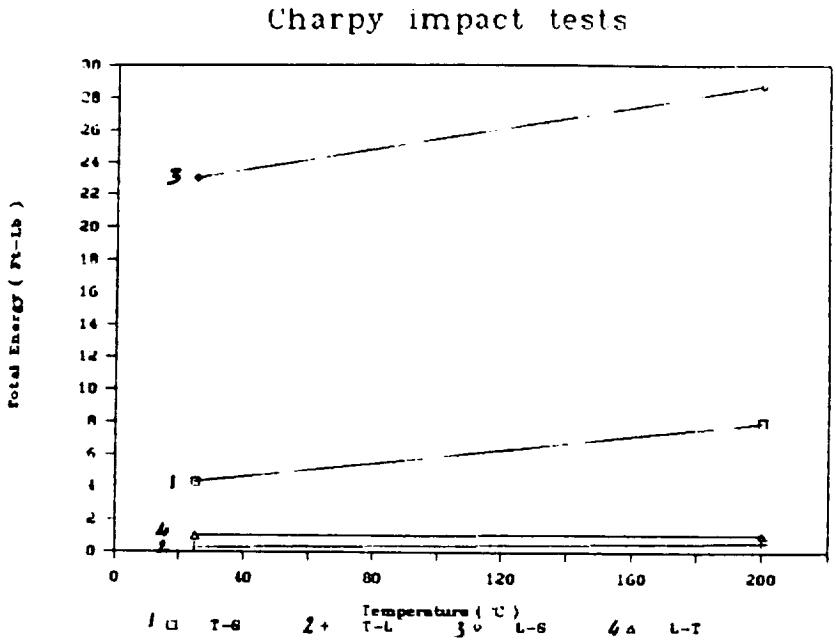

Figure 3(b): Effect of the orientation of the notch on the propagation energy.

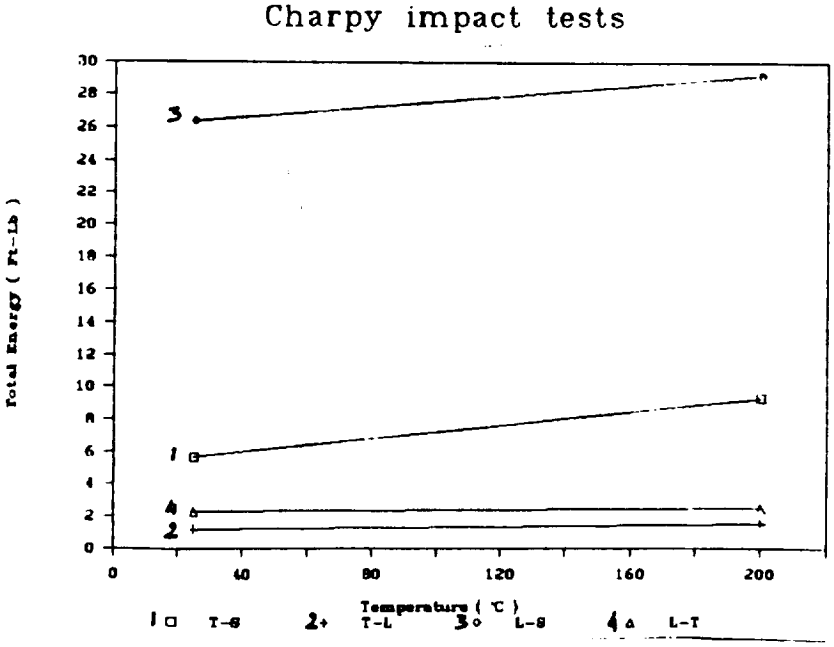

Figure 3(c): Effect of the orientation of the notch on the total energy of the Charpy impact test.

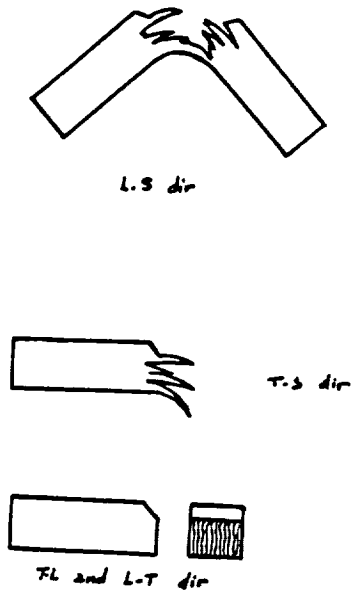

Figure 4: Schematic representation of failure modes for the charpy impact specimens.

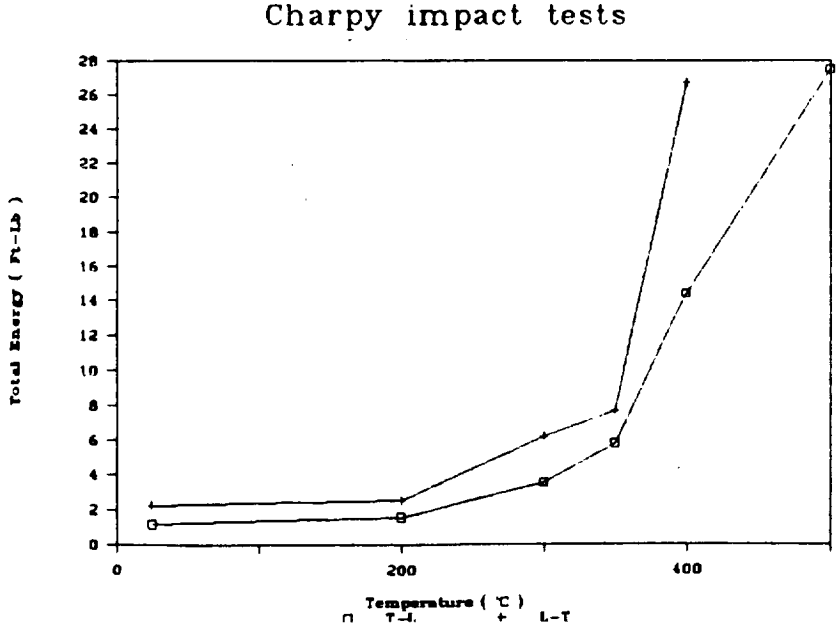

Figure 5: Effect of the temperature on the total energy of the Charpy impact test.

DISTRIBUTION LIST

1 - 3 Mr. D. L. Dicus
Contract Monitor
Metallic Materials Branch, MS 188A
NASA Langley Research Center
Hampton, VA 23665

4 - 5* NASA Scientific and Technical Information Facility
P. O. Box 8757
Baltimore/Washington International Airport
Baltimore, MD 21240

6 Mr. J. F. Royall, Jr.
Grants Officer, M/S 126
NASA Langley Research Center
Hampton, VA 23665

7 Dr. Charles E. Harris
Mechanics of Materials Branch
NASA Langley Research Center
Hampton, VA 23665

8 Mr. W. Barry Lisagor
Metallic Materials Branch
NASA Langley Research Center
Hampton, VA 23665

9 Mr. T. W. Crooker
Code RM
NASA Headquarters
Washington, DC 20546

10 Dr. J. C. Neuman
Mechanics of Materials Branch
NASA Langley Research Center
Hampton, VA 23665

11 Mr. W. Brewer
Metallic Materials Branch, MS 188A
NASA Langley Research Center
Hampton, VA 23665

12 Mr. Dana Ward
Northrop Corporation
1 Northrop Avenue
Mail Zone 3872562
Hawthorne, CA 90250-3277

13 - 14 R. E. Swanson
Department of Materials Engineering
Virginia Polytechnic Institute and State University
Blacksburg, VA 24061

15	E. A. Starke, Jr., UVa.
16 - 17	R. P. Gangloff, MS
18	G. E. Stoner, MS
19	J. A. Wert, MS
20	F. E. Wawner, MS
21	T. H. Courtney, MS
22	W. D. Pilkey, MAE
23	E. A. Thornton, MAE
24	J. K. Haviland, MAE
25	M. A. Townsend, MAE
26	C. T. Herakovich, CE
27	M. J. Pindera, CE
28	L. A. Hoel, CE
29 - 30	E. H. Pancake, Clark Hall
31	SEAS Preaward Administration Files

*One reproducible copy

JO#2634:ph